HAL
open science

Patient-specific biomechanical model of the respiratory system for radiation therapy

Matthieu Giroux

To cite this version:

Matthieu Giroux. Patient-specific biomechanical model of the respiratory system for radiation therapy. Modeling and Simulation. Université de Lyon, 2018. English. NNT : 2018LYSE1205 . tel-01963904v2

HAL Id: tel-01963904

https://hal.science/tel-01963904v2

Submitted on 18 Jan 2021

HAL is a multi-disciplinary open access archive for the deposit and dissemination of scientific research documents, whether they are published or not. The documents may come from teaching and research institutions in France or abroad, or from public or private research centers.

L'archive ouverte pluridisciplinaire **HAL**, est destinée au dépôt et à la diffusion de documents scientifiques de niveau recherche, publiés ou non, émanant des établissements d'enseignement et de recherche français ou étrangers, des laboratoires publics ou privés.

N°d'ordre NNT : 2018LYSE1205

THESE de DOCTORAT DE L'UNIVERSITE DE LYON
opérée au sein de
l'Université Claude Bernard Lyon 1

Ecole Doctorale N° 512
InfoMaths

Spécialité de doctorat :
Informatique

Soutenue publiquement le 17/10/2019, par :
Matthieu Giroux

Patient-specific biomechanical model of the respiratory system for radiation therapy

Devant le jury composé de :

Chèze,Laurence	Professeure	Université Lyon 1	Présidente du jury
Hahmann,Stefanie	Professeure	Université Grenoble	Rapporteure
Daniel,Marc	Professeur	Ecole Polytech Marseille	Rapporteur
Promayon,Emmanuel	Professeur	Université Grenoble Alpes	Examinateur
Shariat, Behzad	Professeur	Université Lyon 1	Directeur de thèse
Ladjal,Hamid	Maître de Conférences	Université Lyon 1	Co-directeur de thèse

UNIVERSITÉ CLAUDE BERNARD LYON 1

Année 2018 *N°*

THÈSE

pour obtenir le grade de

Docteur

Spécialité : **Informatique**

préparée au **Laboratoire d'InfoRmatique en Images et Systèmes d'information**

dans le cadre de l'Ecole Doctorale **Math-Info**

présentée et soutenue publiquement

par

Matthieu Giroux

le

17/10/2018

Titre :

Patient-specific biomechanical model of the respiratory system for radiation therapy

Préparée sous la direction de

Hamid Ladjal et Behzad Shariat

Composition du Jury

M.	Marc Daniel, Professeur Ecole Polytech Marseille	Rapporteur
Mme.	Stefanie Hahmann, Professor, Université Grenoble INP-Ensimag	Rapporteure
Mme.	Laurence CHEZE, Professeur Université Lyon 1	Examinatrice
M.	Emmanuel Promayon, Professeur Université Grenoble Alpes	Examinateur
M.	Behzad Shariat, Professeur Université Lyon 1	Directeur de thèse
M.	Hamid Ladjal, Maître de Conferences Université Lyon 1	Co-directeur de thèse

Patient-specific biomechanical model of the respiratory system for radiation therapy

Abstract: The 4D computational patient specific of the respiratory system could be potentially used in various medical contexts; for diagnosis, treatment planning, laparoscopic, dose computation or the registration between online imaging systems such as positron emission tomography (PET), computed-tomography (CT) as well as high fidelity and precise computer-based training simulators. The main novelty of this PhD project lies in the context of radiation therapy; we have developed a patient-specific biomechanical model of the respiratory system enabling the correlation of the internal organs motion with respiratory surrogate signal(s) during the treatment. This permits to take into account the respiratory motion variabilities. The deformation of the different structures is controlled and driven by simulated rib cage (mimic the external intercostal muscles) and diaphragm actions. For the diaphragm, we have applied the radial direction of muscle forces, and simple homogeneous dirichlet boundary condition is applied to the lower part of the diaphragm, which is attached to the rib cage. For each rib a rigid transformation is calculated automatically by finite helical axis method (rigid translation and rotation) and used to define displacement boundary conditions. The resulting widening of the thoracic cavity forces the lungs to expand due to an applied negative pressure in the pleural cavity. Other novelty of the PhD project, that the amplitude of the lung pressure and diaphragm force are patient-specific, and determined at different respiratory states by an optimization framework based on inverse FE analysis methodology, by minimizing the volume lungs errors, between the respiratory volume (calculated from CT scan images at each state) and the simulated volume (calculated by biomechanical simulation). All other structures are linked to each other, but feature different deformation behavior due to the assigned material properties. Our results are quite realistic compared to the 4D CT scan images and the proposed physically-based FE model is able to predict correctly the respiratory motion.

Keywords: Biomechanics, Respiratory motion, Finite element method, Medical imaging

Acknowledgement

This research is supported by French Ministry of Education and Research, by the LABEX PRIMES (ANR-11-LABX-0063), within the program "Investissements d'Avenir" (ANR-11-IDEX-0007) operated by the French National Research Agency (ANR).

Contents

1 Framework of the PhD project **5**

1.1 Introduction . . . 5

1.2 Respiratory-induced organ motion . . . 7

1.2.1 Methods to manage breathing motion . . . 7

1.2.2 Beam gating technique . . . 9

1.2.3 Beam tracking system . . . 10

1.3 Medical context: radiation therapy treatment . . . 10

1.4 Objective of the PhD and document organization . . . 12

2 Biomechanical Modeling of Respiratory Organ Motion **15**

2.1 Anatomy and physiology of the respiratory system . . . 15

2.1.1 Lungs . . . 16

2.1.2 Diaphragm . . . 16

2.1.3 Thoracic cage . . . 18

2.1.4 The mediastinum . . . 18

2.1.5 Physiology of the Respiratory System . . . 19

2.1.6 Inhalation and Exhalation . . . 19

2.1.7 Physiological description of compliance . . . 20

2.2 Biophysical modeling of breathing mechanics . . . 22

2.2.1 Motion of a single organ: the lungs . . . 23

2.2.2 Motion of the respiratory system including the different organs . . . 26

2.3 Conclusion . . . 28

3 Anatomical and biomechanical patient specific model of the respiratory system **33**

3.1 Introduction . . . 34

3.2 Patient-specific anatomical model of respiratory system . . . 34

3.2.1 3D segmentation and surface extraction . . . 35

3.2.2 Surface mesh treatment . . . 37

3.3 Patient-specific respiratory mechanics . . . 40

3.3.1 Input data and appropriate prediction of the mechanic behavior . . . 41

3.3.2 Formulations of FEM . . . 44

3.3.3 Geometrical Non-linear hyper elastic behavior: Saint-Venant Kirchhoff 46

3.3.4 Thoracic cage and rib kinematics . . . 47

3.3.5 The boundary conditions (BC) 48
3.3.6 Automatic tuning and optimization 50
3.3.7 Dynamic Model 51
3.3.8 Density mapping 51
3.4 Conclusion of this chapter 52

4 Simulations and evaluation 53
4.1 Introduction 54
4.2 Evaluation metrics 54
4.2.1 Computation of landmark and surface errors 54
4.2.2 Lung tumor motion 54
4.3 Simulations and evaluation 56
4.3.1 Contact stabilization 56
4.3.2 Mesh quality and mesh convergence study 57
4.3.3 Qualitative and quantitative comparison 58
4.3.4 Anatomical landmarks evaluation at end of inhalation (EI) and the end of exhalation (EE) 60
4.3.5 Anatomical landmarks evaluation at intermediate states between EI and EE 62
4.3.6 Mechanical parameters uncertainty assessment 65
4.3.7 Behavior uncertainty 70
4.3.8 Discussion and conclusion 71

5 General conclusions and future perspectives 75

6 Résumé en français 79
6.1 Introduction 79
6.2 Contributions 80
6.3 Conclusion 81

A Hyperelastic models 83

B Principle of Mechanical Resolution by the Finite Element Method 87
B.1 Variational approach 87
B.2 Discretization in elements. 88
B.3 Numerical integration and Matrix system 89

C Geometrical tools for breathing modelisation 93
C.1 Principle of Non-Uniformal Rational B-Splines 93
C.2 Principle of a-shape 94

Bibliography 105

Publications related to this work

Peer-reviewed journal articles

Matthieu Giroux, Hamid Ladjal, Philippe Giraud, Michael Beuve Shariat Behzad (2017). "Patient-Specific Biomechanical Modeling of the Lung Tumor for Radiation Therapy". Computer Methods in Biomechanics and Biomedical Engineering, vol. 20, sup1, pp. 95-96. doi: 10.1080/10255842.2017.1382878. HAL : hal-01628725.

Conference contributions

Matthieu Giroux, Hamid Ladjal, Michael Beuve Behzad Shariat (2017). "Biomechanical Patient-Specific Model of the Respiratory System Based on 4D CT Scans and Controlled by Personalized Physiological". Medical Image Computing and Computer Assisted Intervention - MICCAI 2017 - 20th International Conference, 13 septembre 2017, Quebec (Canada), pp. 216-223. HAL : hal-01589991.

Hamid Ladjal, Nadir Skendraoui, **Matthieu Giroux**, Yazid Touileb, Joseph Azencot, Michael Beuve, Philippe Giraud and Behzad Shariat (2015). "Physiological and Biomechanical Model of Patient Specific Lung Motion Based on 4D CT Images". The 8th Biomedical Engineering International Conference (IEEE BMEiCON2015), 27 november 2015, Thaïlande. HAL : hal-01214310.

Workshops

Matthieu Giroux, Hamid Ladjal, Michael Beuve Behzad Shariat (2017). "Modélisation biomécanique patient spécifique du système respiratoire: application radio/hadrontherapie". 42ème Congrès de la Société de Biomécanique, 2 et 3 novembre 2017, Rennes, France (présentation Orale).

List of Acronyms

IMRT Intensity Modulated Radiotherapy

HT Hadron Therapy

SOBP Spread Out Bragg Peak

RBE Relative Biological Effectiveness

DNA Deoxyribose Nucleic Acid

ICRU International Commission on Radiation Units and Measurements

GTV Gross Tumour Volume

CTV Clinical Target Volume

ITV Internal Target Volume

PTV Planning Target Volume

OAR Organs At Risk

CT Computed Tomography

DIR Deformable Image Registration

PDE Partial Differential Equations

FEM Finite Element Method

EE End Exhale

EI End Inhale

PET Positron Emission Tomography

CAD Computed Aided Design

HIT Heidelberg Ion beam Therapy center

Chapter 1

Framework of the PhD project

The first chapter presents the context of the PhD thesis which is treating moving tumours with particle beam therapy. We start with a brief introduce the notion of Hadron Therapy (HT) as an emerging alternative improved solution to conventional radiotherapy. Then we briefly describe the basic physical principles behind HT. Next we provide a comprehensive review of the current research status in hadron therapy with a focus on moving tumours. Overcoming the challenge of tumour motion requires a knowledge about the internal motion of the patient. Therefore we briefly describe the existing motion estimation techniques and ends with a detailed presentation of the objectives of this thesis.

Contents

1.1 Introduction **5**

1.2 Respiratory-induced organ motion **7**

1.2.1 Methods to manage breathing motion 7

1.2.2 Beam gating technique 9

1.2.3 Beam tracking system 10

1.3 Medical context: radiation therapy treatment **10**

1.4 Objective of the PhD and document organization **12**

1.1 Introduction

Lung cancer is an enormous healthcare challenge. In Europe 350 thousands people die every year of lung cancer, the leading cause of all cancer deaths. It has the highest economic costs (EUR 18.8 billion) of all cancer types, representing 15% of all cancer health care costs. While historically a disease affecting mostly men, lung cancer rates are rising in women in recent decades, predicted to overtake breast cancer as the leading death cause in women this year. Besides surgery and chemotherapy, sterilizing tumours with ionising radiation (radiotherapy or hadrontherapy) is an important treatment modality for lung cancer, with 75% of patients benefiting from radiotherapy at some point in their life. To meet the lung cancer challenge, modern medicine is moving towards personalised care. Radiation

cancer therapy is ideally suited for personalization because it can be combined in various ways with other treatment modalities (surgery, chemotherapy, targeted agents) and can be modulated in space (3D radiation dose delivery) and in time (dose is delivered in fractions over multiple days/weeks). Radiation cancer therapy aims at delivering a lethal dose of ionizing radiation to tumour tissues while sparing the surrounding tissues from the adverse effects of radiation. Techniques such as Intensity Modulated Radiation Therapy (IMRT) or Hadron Therapy (HT) as proton therapy, can allow the reduction of safety-margins and the escalation of the therapeutic dose in the tumour volume.

Radiation therapy is the medical use of ionizing radiation to treat cancer. In conventional radiation therapy, beams of X rays (high energy photons) are produced by accelerated electrons and then delivered to the patient to destroy tumour cells. Using crossing beams from many angles, radiation oncologists irradiate the tumour target while trying to spare the surrounding normal tissues. Inevitably some radiation dose is always deposited in the healthy tissues.
When the irradiating beams are made of charged particles (protons and other ions, such as carbon), radiation therapy is called hadrontherapy. The strength of hadrontherapy lies in the unique physical and radiobiological properties of these particles; they can penetrate the tissues with little diffusion and deposit the maximum energy just before stopping. This allows a precise definition of the specific region to be irradiated. The peaked shape of the hadron energy deposition is called Bragg peak and has become the symbol of hadrontherapy. With the use of hadrons the tumour can be irradiated while the damage to healthy tissues is less than with X-rays (Figure 1.1).

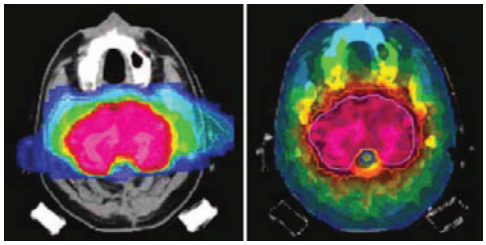

Figure 1.1 – Comparison of dose distribution in the case of a large tumour located in the base of the skull.(Left) HT using Carbon ions (two fields). (Right) IMRT (nine fields). In the case of HT it can be noticed a substantial reduction in the deposited dose in the normal tissue as compared to IMRT. Taken from [Durante 2010].

Tumour motion, especially due to respiration, during irradiation reduces target coverage and increases dose to healthy tissues. This motion modifies the internal organs shape, position and densities. However, beside the target ballistics information, hadrontherapy requires an accurate knowledge about the density and the chemical composition of all the traversed organs by the beam, since it determines the position of maximum deposited energy carried by the ions, usually referred to as the Bragg peak (see Figure 1.2).

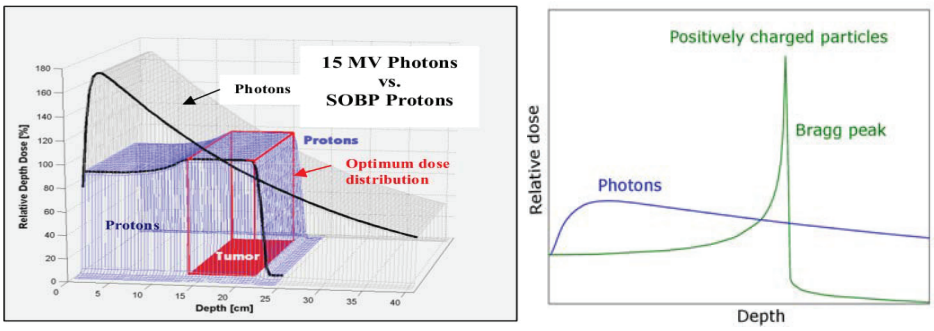

Figure 1.2 – Right : the schematic comparison between the dose profiles of photons and of charged particles used in HT. Left: a high dose of radiation is distributed to the tumour volume while not exceeding the tolerable dose of nearby critical healthy tissues. In contrast, with photons a lower dose is delivered to the tumour and a significant dose to the normal tissues distal from the tumour (figure taken from [Smith 2009]).

1.2 Respiratory-induced organ motion

Two types of motion variations can be distinguished, inter-fraction or intra-fraction:

— Inter-fraction motions consist in all the varying shapes in the patient anatomy from one treatment session to another, such as tumour swelling or shrinkage [Mori 2009], position changes dues to bladder or intestinal gas [Fokdal 2004] or anatomy variations due to patient weight loss.

— Intra-fraction motions represents all the motion occurring during the delivery: e:g:, breathing, heart beats, hiccup, cough.

In this manuscript we will focus on breathing-induced intra-fractional motion.
Respiration is the most important source of intra-fraction motion in the patient's body. The pancreas, the liver, the duodenum, the kidneys and obviously the lungs suffer from deformations induced by breathing. As a consequence, tumours situated in such moving organs continuously change position (and sometimes shape) during treatment [Seppenwoolde 2002]. For example, Lung tumour displacement can range up to more than 2 cm, while lung volume varies by about 25% during respiration [Langen 2001]. A schematic representation of the breathing curve and lung inflation is depicted in Figure 1.3. A detailed description on intra-fractional lung tumour motion in the lungs was published elsewhere [Shirato 2004].

1.2.1 Methods to manage breathing motion

In the following section, we are going to briefly describe the various intra-fraction motion mitigation techniques used in radiation therapy.

1.2.1.1 Organ motion reduction

One solution is to reduce the organ motion of the patient using for example abdominal compression [Negoro 2001] or partial/complete stop of the patient respiration [Hof 2003]. However, these techniques would substantially increase the patient setup time as well as

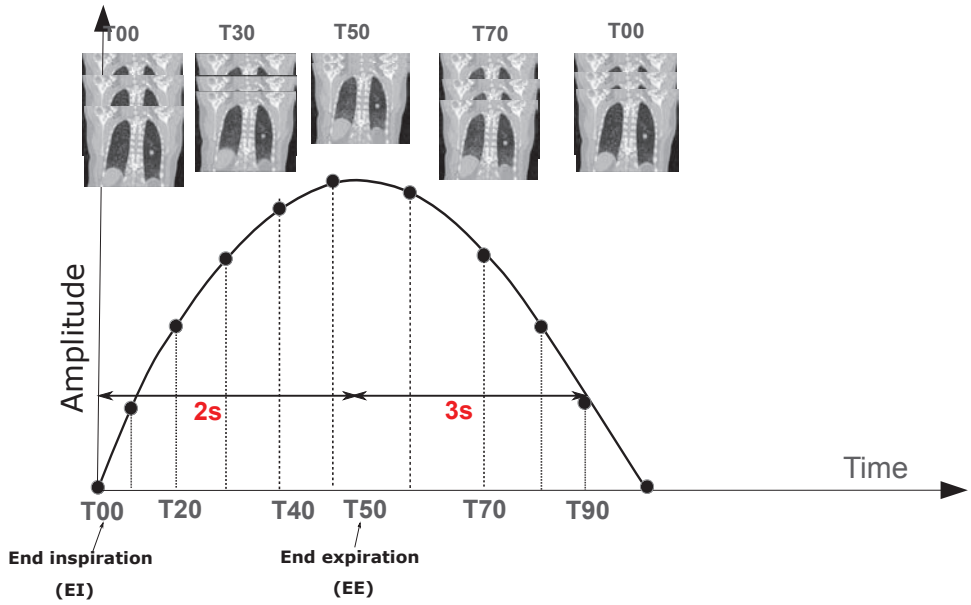

Figure 1.3 – Lung deformations during the full breathing cycle and intermediate states (10 states). Image slices of a patient case are taken from the DIR-lab data base [Castillo 2009]. The curve is only for illustration purposes .

the associated clinical workload.

1.2.1.2 Treatment margins optimization

According to the International Commission on Radiation Units and Measurements (ICRU), in this section we introduce the common definition of treatment margins used in conventional radiation therapy. In order to include the tumour motion inside the beam field, we increase the different treatment margins [Jones 1994]:

— The Gross Tumour Volume (GTV) consists in the visible/palpable tumour volume.

— The Clinical Target Volume (CTV) adds extra margins to the GTV in order to include non-visible latent tumour spread.

— The Internal Target Volume (ITV) includes extra margins aimed to compensate for variations in size, shape and position of the CTV during irradiation.

— The Planning Target Volume (PTV) consists in the volume that takes into consideration the effect of all the possible geometrical variations ensuring that the prescribed dose is actually absorbed in the CTV for a specific beam arrangement.

— The Organs At Risk (OAR) represent normal tissues in the vicinity of the tumour usually with a high radiosensitivity. The delivery of the beam needs to be done in such a way that the OAR do not receive more dose than they can tolerate.

Figure 1.4 shows how the different volumes are related to each other from a geometrical point of view for lung cancer. In the case of moving tumours, the PTV is increased so that the tumour lies inside the treatment field at all times. This technique is usually used in IMRT and recently in passive HT [Nihei 2006]. Nevertheless, the downside of this approach

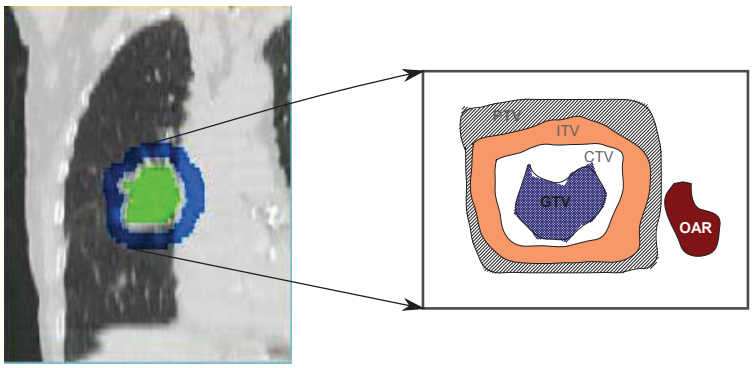

Figure 1.4 – Schematic representation of the volumes of interest defined by the ICRU [Jones 1994]. An example of the different treatment margins on lung cancer.

is that increasing the target volume implies more dose delivered to the surrounding tissues and possibly to the OAR.

1.2.2 Beam gating technique

Fig.1.5 illustrates the principal of bean gating technique, where the irradiation occurs only during specific portions of the breathing cycle and synchronized to the breathing motion of the patient in phases with little motion [Minohara 2000], [Lu 2007]. The major disadvantage of this technique has the treatment time is prolonged due to the frequent interruptions of the beam delivery. Moreover, this technique cannot take into consideration the variations of the patient's breathing pattern because the beam gating is based on previously acquired images.

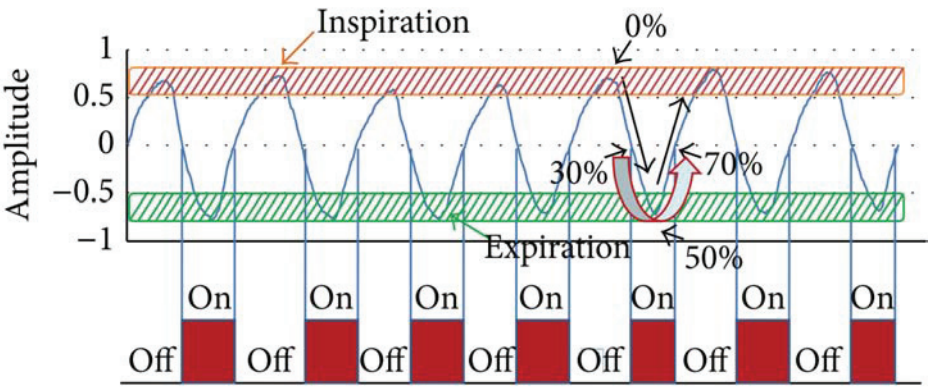

Figure 1.5 – An example of the respiratory gating radiation therapy during the specific period of respiration. Taken from [Jung Ae Lee 2014]

1.2.3 Beam tracking system

Fig.1.6 shows an example of a beam tracking system used in the clinical environment is the robotic Cyberknife Synchrony system (Accuray Inc., Sunnyvale, Ca., USA) applied to x-ray radiosurgery [Kilby 2010]. The system has the capacity to acquire two orthogonal 2D radiographies during treatment which are used to reposition the beam. Three fiducial markers can be implanted in the tumour and visualized with the x-ray imaging system and therefore the position of the tumour is estimated at any time during the treatment. Nevertheless, this is a highly invasive procedure and it cannot predict the deformations of the tumour shape. Moreover, the density changes along the beam path cannot be properly determined which is essential in the case of HT.
Other example of a beam tracking system with carbon ions has been implemented at GSI (Centre for Heavy Ion Research). The beam is moved laterally with the two scanner magnets, while the range of the beam is adjusted by fast energy modulation[Bert 2010]. Unfortunately, the system is not ready for clinical use as it requires accurate real-time internal motion monitoring in order to ensure the correct motion compensation. A more detailed review concerning motion mitigation techniques for particle therapy can be found elsewhere [Bert 2011].

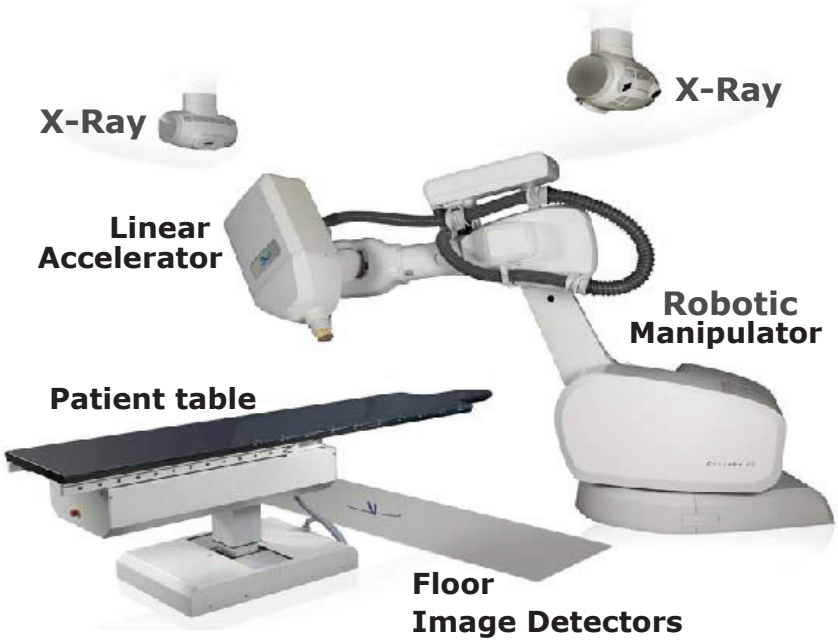

Figure 1.6 – An example of the robotic Cyberknife Synchrony system (Accuray Inc., Sunnyvale, Ca., USA) applied to x-ray radiosurgery.

1.3 Medical context: radiation therapy treatment

The Fig.1.7 shows the description of the different steps and workflow of radiation ther-

apy with summary of each phases.

The first step is the patient immobilization aimed to minimize patient motion during treat-

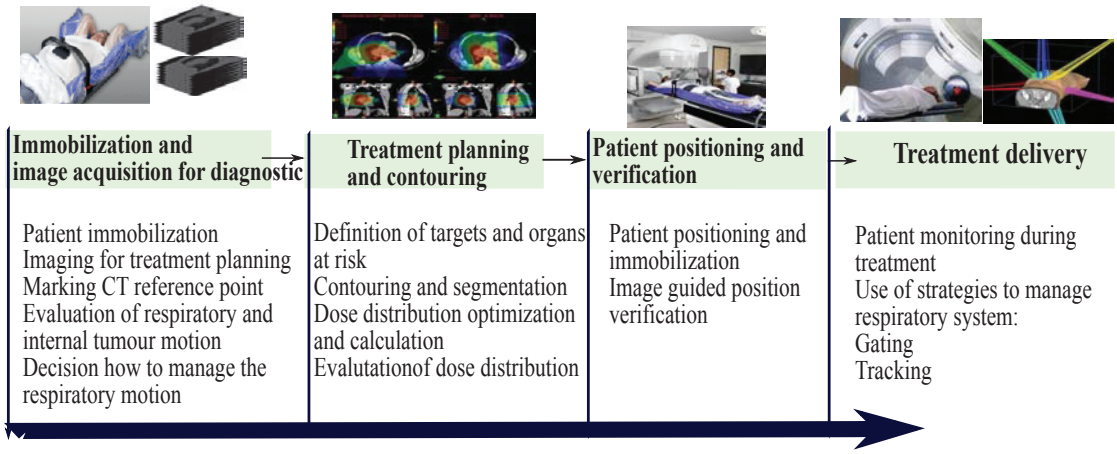

Figure 1.7 – Description of the different steps and workflow of radiation therapy with summary of each phases.

ment. Then, the next step is the acquisition of a CT images of the patient in the treatment position. The CT images are used to create a virtual three-dimensional 3D model of all organs on which radiation therapy planning will be based and simulated. At this level of the workflow, internal tumour motion caused by breathing should be evaluated to define the margin of treatment field. To ensure sufficient dose coverage throughout the treatment course, internal margin (IM) and setup margin (SM) are added to the clinical target volume (CTV) to make up the planning target volume (PTV). If target motion amplitude is large, the inclusion of the entire region in the treatment volume might result in exceedingly high rates of toxicity [Ota S 2015]. Therefore, the respiratory motion should be managed. The different techniques to manage respiratory motion include abdominal compression, synchronization of radiation delivery with a particular stage of the respiratory cycle (gating), and moving the radiation beam so as to follow the tumor motion trajectory in real time (tracking) when possible. The next step, concerning the treatment planning and dose calculation. In this step, multiple radiation fields and a highly conformal dose distribution around the target volume are calculated and optimized based on different algorithms including the respiratory motion models as image registration. However, these methods cannot fully consider the density variations of the tissues in the fact that respiratory motion is not reproducible.

In the next step, patient positioning and verification based on 3D coordinates of the target to position patients for radiation therapy delivery. This is achieved with the use of image-guided radiation therapy techniques. Finally, the delivery treatment can be performed with linear accelerators, with tools that allow monitoring of target motion as image-guided radiation therapy in order to image the tumor before and during treatment. By comparing these images to the reference images taken during simulation, the patient's position and/or

the radiation beams may be adjusted to more precisely target the radiation dose to the tumor. After the treatment, we have a treatment verification step, to monitor treatment progress and weekly review session.

Unfortunately, breathing is an active and complex process where the respiratory motion is non-reproducible [Shirato 2006]. As shown by many studies, the breathing periodicity, amplitude and base line of patients can vary during a single imaging or treatment session. Lung tumours can even present hysteresis in their trajectories, making them more difficult to locate with precision.

The current solutions are invasive and would greatly increase the radiation dose to the patient due to imaging and generally, it is very difficult or impossible to accurately identify the tumour location during the treatment. All these techniques require a treatment plan based on a motion model associated to the breathing induced organ motion that ideally would estimate the position of the tumour and surrounding organs at any time during treatment and this uncertainty on the position makes necessary the development of a strategy for the prediction of tumour motion during radiation treatment.

An alternative way is to use a correspondence model to find the relationship between the internal organs motion and the external respiratory surrogate signals, such as spirometry or the displacement of the skin surface, which can be easily measured during treatment [Ehrhardt 2013].

1.4 Objective of the PhD and document organization

In my PhD project, we have proposed and developed a novel approach to monitor the lung motion due to diaphragm motion and thoracic movement (rib kinematics) during radiation treatment based on continuous mechanics laws. This model can help and calculate the dose distribution on lung tumour including biomechanical tumour motion. The Fig. 1.8 illustrates the concept based on biomechanical patient specific model of the respiratory system. During the expiration, the diaphragm contracts and moves lower, the chest cavity enlarges, reducing the pressure within the pleura region. To equalize the pressure, air enters the lungs. When the diaphragm relaxes and moves back up; the elasticity of the lungs and chest wall pushes air out of the lungs.

An important novel aspect of the proposed concept is that we are able to correlate the diaphragm motion to the lung volume variation measured directly by an external sensor (spirometer), and the rib displacement by the the measurement of the 3D displacement of the thorax surface. This model is able to take into account the variability and non reproducibility the respiratory system during treatment, and find the relationship between a respiratory surrogate signal(s) and the motion of the internal anatomy. The developed model allows to:

- take into account the non-reproducible aspects of the motion and the different types od breathing (chest breathing, abdominal breathing or combined breathing),
- establish a bio-mechanical model from patients geometrical and physical data,
- be able to monitor the internal motion by external sensors during the treatment.

For the diaphragm, we have applied the radial direction of muscle forces, and simple

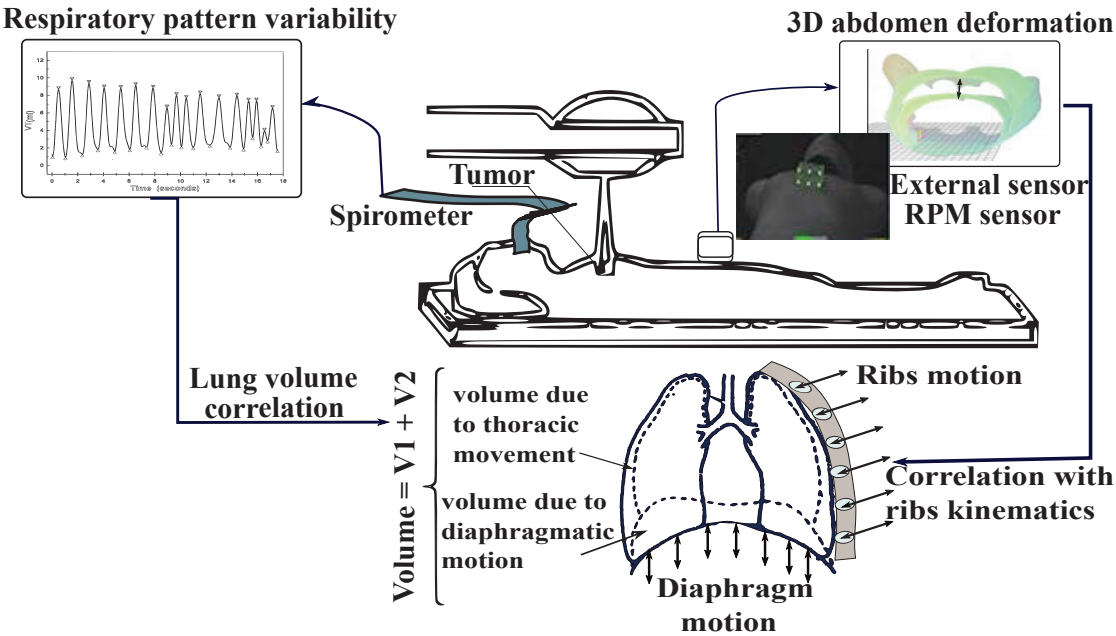

Figure 1.8 – Global methodology to monitor the lung motion by the diaphragm muscles and rib kinematics, correlated to external sensors during treatment: between the spirometer and/or the capture of thoracic motion .

homogeneous dirichlet boundary condition is applied to the lower part of the diaphragm, which is attached to the rib cage. For each rib a rigid transformation is calculated automatically by finite helical axis method (rigid translation and rotation) and used to define displacement boundary conditions. The resulting widening of the thoracic cavity forces the lungs to expand due to an applied negative pressure in the pleural cavity. Other novelty of the PhD project, that the amplitude of the lung pressure and diaphragm force are patient-specific, and determined at different respiratory states by an optimization framework based on inverse FE analysis methodology, by minimizing the volume lungs errors, between the respiratory volume (calculated from CT scan images at each state) and the simulated volume (calculated by biomechanical simulation). All other structures are linked to each other, but feature different deformation behavior due to the assigned material properties.
This document is organized as follows: In chapter 2, we present a related research of the biomechanical respiratory system models. Next, in the chapter 3 we describe how to build anatomical and biomechanical patient specific model of the respiratory system from 4D scan images and controlled by personalized physiological compliance. First, we propose and improve the geometrical modeling procedure for accurate reconstruction of respiratory system. This procedure consists of medical image segmentation, geometrical reconstruction of all relevant tissue of the respiratory system, generation of geometric approximations (boundary surfaces and volumetric meshes) of three-dimensional anatomy suited for finite element analysis. Then, we illustrate our approach to predict the internal movement from two external parameters; the volume of air exchanged and the thoracic movement (rib kinematics). This approach is based on biomechanical patient-specific model of the respi-

ratory system, constrained by real boundary conditions, coupled with an automatic tuning algorithm to compute lung pressures and diaphragm forces during a whole respiratory cycle. Chapter 4 presents our finite element simulations and results based on patient specific biomechanical model of the respiratory system. The qualitative and qualitative evaluations have been done by comparing the finite element simulation with the experimental data (4D CT scan images) on anatomical landmarks, at end inspiration (EI), end expiration (EE) states, and at each intermediate respiratory state. Also, the tumour trajectory evaluation and the sensitivity analysis results as well as experimental validation are included in this chapter. Finally we lay down the general conclusion and discuss possible future directions in Chapter 5.

Chapter 2

Biomechanical Modeling of Respiratory Organ Motion

In this section, we introduce the most important mechanical organs of the respiratory system starting with anatomy and physiology of the breathing. In the following section we present a non-exhaustive literature review of existing research on biomechanical models of the respiratory system. This is followed by a discussion and a comparison study between the existing models and our proposed approach.

Contents

2.1 Anatomy and physiology of the respiratory system 15
2.1.1 Lungs 16
2.1.2 Diaphragm 16
2.1.3 Thoracic cage 18
2.1.4 The mediastinum 18
2.1.5 Physiology of the Respiratory System 19
2.1.6 Inhalation and Exhalation 19
2.1.7 Physiological description of compliance 20
2.2 Biophysical modeling of breathing mechanics 22
2.2.1 Motion of a single organ: the lungs 23
2.2.2 Motion of the respiratory system including the different organs . . . 26
2.3 Conclusion 28

2.1 Anatomy and physiology of the respiratory system

Breathing is an active and complex process where the mechanics of the respiratory motion is controlled by two muscle groups: the diaphragm and the intercostal muscles. The lung is a mechanically passive organ and is linked to the diaphragm and to the ribs through the pleura (Fig.2.3). The lungs inflates mainly due to thoracic pressure variations

and forces exerted by the diaphragm to its bottom surface. The pleura consists of two sheets (visceral and parietal). The visceral pleura is attached to the lungs and the parietal pleura is attached to the diaphragm and to the chest wall. Between the two sheets, an incompressible fluid allows lungs to slide while they follow diaphragm and ribs motion. The trachea descends from the mouth and branches into the two main bronchi to supply air to either half of the lung. The pulmonary artery, coming from the heart, supplies blood for gas exchange.

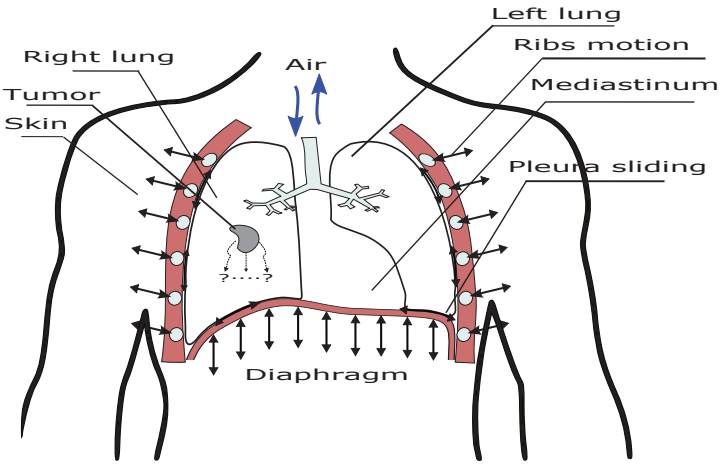

Figure 2.1 – Respiratory mechanics: the role of the diaphragm and thorax in breathing.

2.1.1 Lungs

The lung is a passive organ, is divided into two halves, the right and left lungs, situated in thorax on either side of the heart. Each half of the lung is composed of smaller units called lobes. The right lung has three lobes called upper, middle and lower lobes. The left lung only has two lobes, the upper and lower. Surrounding the lung is an airtight membrane called the pleural cavity. The pleural cavity is surrounded by the the chest wall on the sides, and the diaphragm on the bottom. This space contains pleural fluid which facilitates near frictionless sliding at this boundary.

2.1.2 Diaphragm

The diaphragm is a dome-shaped musculofibrous membrane concave toward the lungs (Fig.2.3) which separates the thorax from the abdominal cavity. It is composed of a peripheral part (muscular fibre) and a central part (tendon). The tendon is the upper part of the diaphragm, in contact with the lungs and is closer to the front than to the back of the thorax, so that the posterior muscular fibres are longer. The peripheral part, which consists of muscles, is linked to the lower thoracic cavity perimeter and has three major insertions: lumbar, sternum and ribs.
Lungs are linked to the diaphragm and to the ribs through the pleura. The diaphragm moves down during the inhalation, creating negative pressure around the thoracic cavity

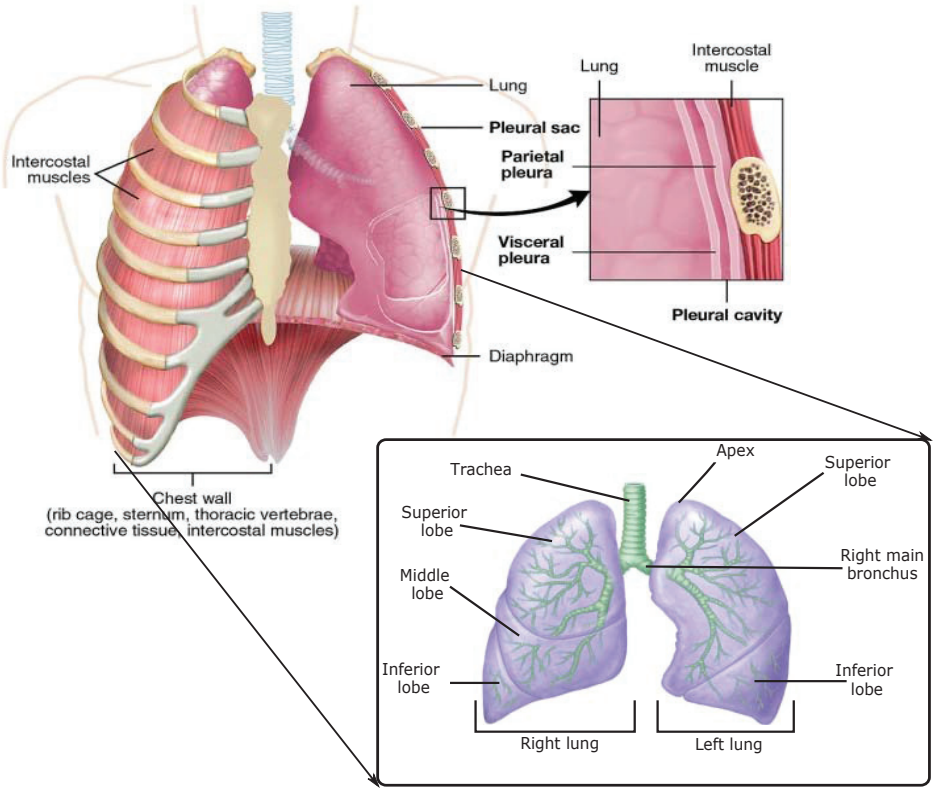

Figure 2.2 – Anatomy of the Lungs divided into two halves, the right and left lungs. Each half of the lung is composed of lobes. Surrounding the lung is an airtight membrane called the pleural cavity. The pleural cavity is surrounded by the the chest wall on the sides, and the diaphragm on the bottom.

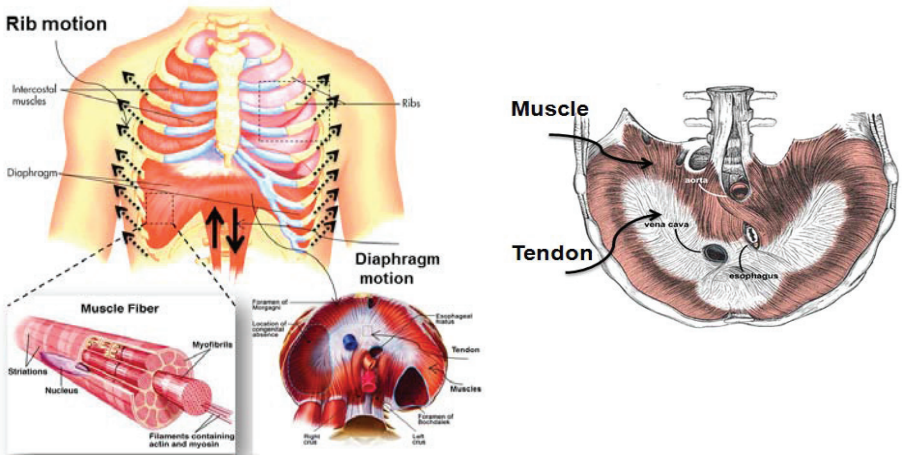

Figure 2.3 – Anatomy of human diaphragm. It is composed of a peripheral part (muscular fibre) and a central part (tendon).

and increasing pressure on abdominal organs. As it moves up during exhalation, the negative pressure in the pleural region decreases, resulting in lungs deflation(Fig. 2.3).

2.1.3 Thoracic cage

The thorax is delimited by the bones of the spine and rib cage and their associated muscles (intercostal muscles). Together the bones and muscles are called the thoracic cage. The ribs and spine (the chest wall) form the sides and top of the cage. A dome-shaped sheet of skeletal muscle, the diaphragm , forms the floor. Between each rib lie several layers of intercostal muscles. When we breathe, the intercostal muscles are responsible for expanding and shrinking the rib cage.
The thoracic cage (rib cage) is the skeleton formed by the 12 pairs of ribs and associated costal cartilages, the sternum and the thoracic vertebrae. The ribs are anchored posteriorly to the 12 thoracic vertebrae (R1-R12). Ribs (R1-R7) are classified as true ribs.
The costal cartilage from each of these ribs attaches directly to the sternum. Ribs (R8-R12) are called false ribs. The costal cartilages from these ribs do not attach directly to the sternum. For ribs (R8-R10), the costal cartilages are attached to the cartilage of the next higher rib. The last two false ribs (R11-R12) are also called floating ribs. These are short ribs that do not attach to the sternum at all.

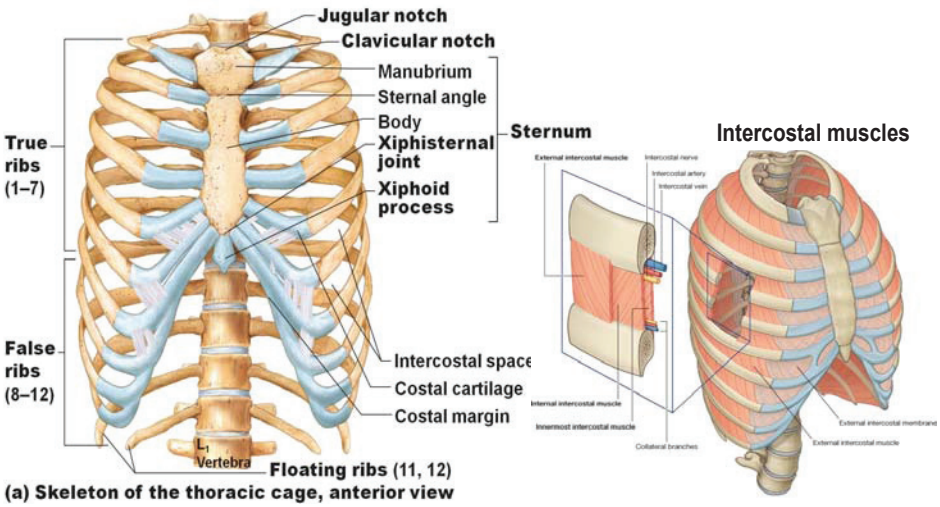

Figure 2.4 – Anterior view of the thoracic cage and intercostal muscles (figure taken from http://anatomysciences.com).

2.1.4 The mediastinum

The mediastinum is an area found in the midline of the thorax that is surrounded by the left and right pleural sacs. It extends from the sternum in front to the vertebral column behind, and contains all the thoracic viscera excepting the lungs. It is divided into two parts: the superior and inferior mediastinum. The inferior mediastinum is further divided into the anterior, middle and posterior mediastinum (Fig. 2.5). Every part of the

mediastinum contains many vital organs, vascular and neural structures that are closely related one to another.

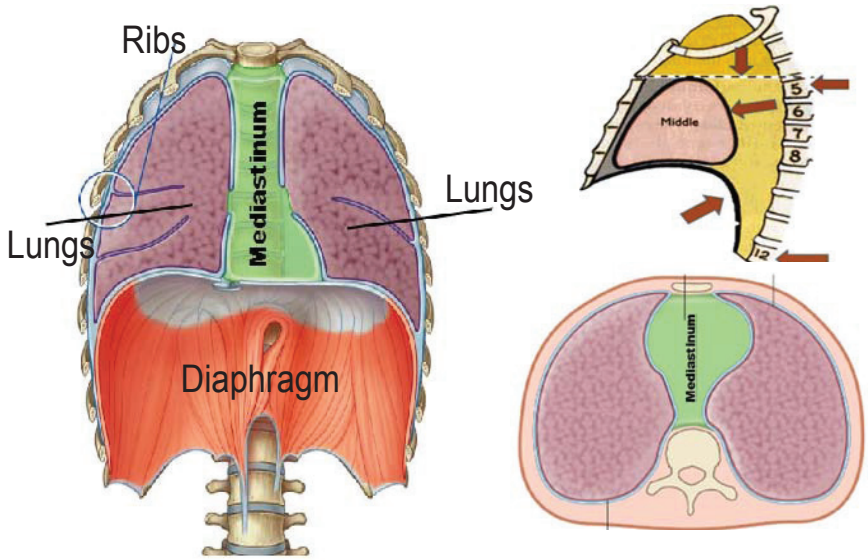

Figure 2.5 – Anatomy the mediastinum area found in the midline of the thorax that is surrounded by the left and right pleural sacs. It is divided into two parts: the superior and inferior mediastinum.

2.1.5 Physiology of the Respiratory System

Negative pressure breathing (natural breathing) initiates when the diaphragm and chest wall move away from the lung, which enlarges the pleural cavity creating a negative pressure on the lung surface. The negative pressure expands lung volume, dropping the internal pressure, allowing air to passively enter the lung.

2.1.6 Inhalation and Exhalation

The mechanics of human breathing involves two steps that alternate with each other: inhalation (inspiration) and exhalation (expiration) (see Fig.2.6). During the process of inhalation, the lung volume expands as a result of the contraction of the diaphragm and intercostal muscles (the muscles that are connected to the rib cage). When the lung volume decreases, the air pressure inside it increases. Thus, air moves out from high pressure in the lungs to low pressure area outside. The process of exhalation, usually a passive process. This process occurs due to an elastic recoil of the lung tissue which causes a decrease in volume, resulting in increased pressure in comparison to the atmosphere; thus, air rushes out of the airway. In fact, the diaphragm and the intercostal muscles relax and involve a smaller thoracic volume and a positive pressure relative to the atmospheric pressure inside the thorax, which causes the expulsion of air outside.

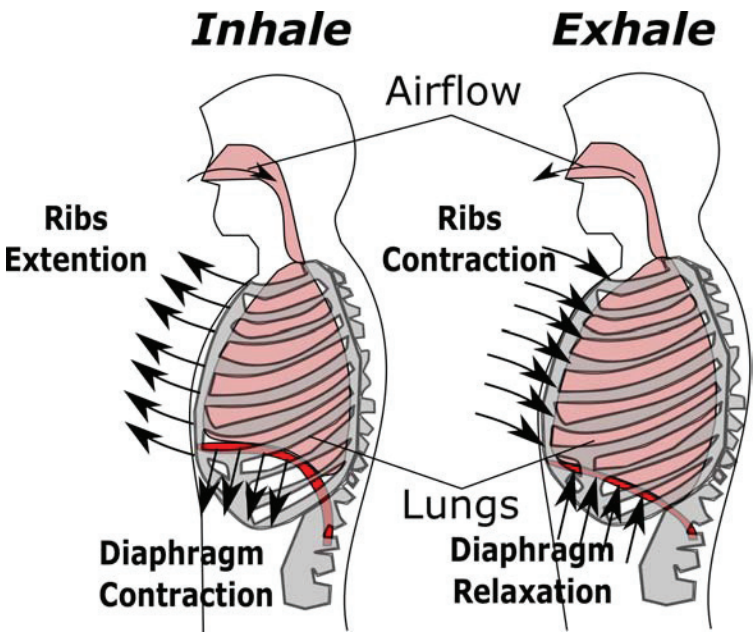

Figure 2.6 – Inhalation and Exhalation: During the process of inhalation, the lung volume expands as a result of the contraction of the diaphragm and intercostal muscles. The exhalation the diaphragm and the intercostal muscles relax and involve a smaller thoracic volume and a positive pressure relative to the atmospheric pressure inside the thorax.

2.1.7 Physiological description of compliance

Lung compliance is the relationship between how much pressure is required to produce a degree of volume change of the lungs (Fig.2.7). It is affected by the elastic properties of the lung. Compliance is a thorough Exploration Functional Exploration (EFR) review. The pulmonary compliance therefore reflects the lung's ability to develop in response to an increase in pressure. It is usually expressed in $ml/cmH2O$. The ratio between the volume variation $\triangle V$ and the pressure $\triangle P$ represents the compliance:

$$C = \frac{\triangle V}{\triangle P}$$

Pressure volume curves of the lung describe lung compliance at different lung volumes and demonstrate hysteresis. The Fig.2.7 shows a theoretical pressure-volume curve (compliance) of the lung. Lung compliance can be classified into two types: static compliance and dynamic compliance.

— Dynamic compliance presents a different path depending on inhalation and exhalation. It corresponds to a measurement taken under conditions of forced or rapid breathing. It is calculated by $C_{dyn} = \frac{Vt}{P_{peek} - PEEP}$ where Vt is the inspired or expired volume, P_{peek} the maximum pressure during the cycle and $PEEP$ residual pressure maintained in the airway during exhalation (Fig.2.8).

— Static compliance is represented by a line whose coefficient of direction is a parameter that we will use in modeling to characterize the elasticity of the lung. It corresponds

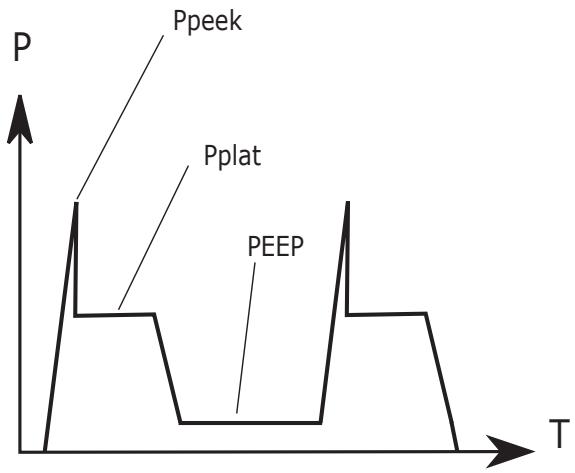

Figure 2.7 – Pulmonary pressure volume curves obtained during inflation and deflation with air: Theoretical curve representing the pressure volume during the full cycle breathing.

to a calm and normal breathing. It is calculated by$C_{stat} = \frac{Vt}{P_{Plat}-PEEP}$ where $P_{Plat}$is the pressure measured during the passive phase of the expiratory cycle.

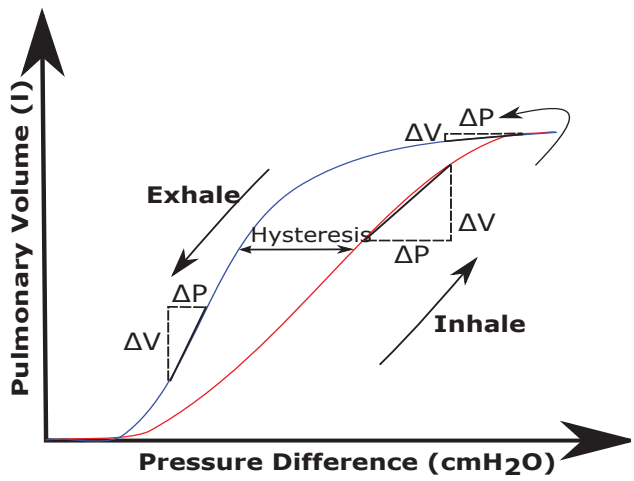

Figure 2.8 – Theoretical curve representing a dynamic compliance calculated by $C_{dyn} = \frac{Vt}{P_{peek}-PEEP}$ where Vt is the inspired or expired volume, P_{peek} the maximum pressure during the cycle and $PEEP$ residual pressure maintained in the airway during exhalation

On the other hand static compliance makes it possible to characterize the elasticity of the lung of a patient, and is considered constant and homogeneous throughout the lung. The lung static compliance can be written as:

$$K = \frac{E}{3(1-2\nu)} = -V_0 \frac{dP_{elastic}}{dV} = -\frac{V_0}{C} \tag{2.2}$$

where K the bulk modulus, is a numerical constant that describes the elastic properties of a solid when it is under pressure on all surfaces.

with E: Young's modulus (or modulus of Elasticity), represents a mechanical property that measures the stiffness of a solid material. It defines the relationship between stress (force per unit area) and strain (proportional deformation) in a material in the linear elasticity regime of a uniaxial deformation.
ν: Poisson ratio is the measurement of the simultaneous change in elongation and in cross-sectional area within the elastic range during a tensile or compressive test. V_0 represents the initial lung volume.
In addition, the Young's modulus (E) and Poisson ratio (ν) are linked to Lame's constants, where μ:Shearing coefficient and λ: Compression coefficient.

$$\mu = \frac{E}{2(1+\nu)} \qquad \lambda = \nu \frac{E}{(1-2\nu)(1+\nu)} \tag{2.3}$$

Under the assumption that elastic pressure is null at equilibrium, after calculations, we can write:

$$P_{elastic_i} = -K \frac{V_i - V_{0_i}}{V_{0_i}} = -\frac{E}{3(1-2\nu)} \frac{V_i - V_{0_i}}{V_{0_i}} \tag{2.4}$$

where $P_{elastic_i}$ presents the elastic pressure at each intermediate respiratory state. V_{0_i} is the initial lung volume at each intermediate respiratory state and the V_i represents the lung volume.
In the next section, we discuss the different motion models for respiratory system in order to predict the position and trajectory of the lung tumor. Therefore, this section is organized as follows: First, we describe models that focus on motion of a single organ (the lungs). Then, we present the extensions of the single organ models to provide motion estimation for several anatomical structures of the respiratory system. Next, we illustrate a comparison studies of biomechanical modeling approaches and our proposed model. We close with conclusions on potential benefits of the proposed approach in this PhD.

2.2 Biophysical modeling of breathing mechanics

Methods usually used to estimate respiratory motion are based on deformable image registration (DIR) techniques. The motion fields are directly calculated and extracted from 4D image sequences (CT or IRM). Often, these methods (rigid or deformable) are accomplished by minimizing/maximizing similarity measures between the 2D frames of the image sequences. A detailed overview of DIR-based methods may be found in [Ehrhardt 2013]. Currently, image-based methods do not explicitly take the information related to the breathing physiology (anatomical boundary conditions, sliding behavior between different organs, compliance...) and physical properties (density and masses, mechanical properties, dynamic....) of organ tissues into account, Unfortunately, these methods assume a reproducible motion of the respiratory system and cannot fully take into account the variability of the respiratory motion.
Indeed, breathing is an active and complex process where the respiratory motion is non-reproducible and this should be taken into account during treatment. This non-reproducibility of the lung motion is explained by the anatomy of the respiratory system. Hence, the respiratory is controlled by two muscle groups: the diaphragm and the intercostal muscles

attached to the ribs.
In this context, biophysical models attempt to overcome these limitations due to variations and non reproducibility of the respiratory motion[Shirato 2006] taking into account the different anatomical and physiological aspects of breathing dynamics of the patients, and generate the patient-specific prediction of respiratory motion.
First, the biophysical models able to simulate the respiratory motion can be classified into two categories: (1) models proposed by the computer graphics community for real time applications [Baudet 2003, Promayon 2008, Villard 2009, Vidal 2012]. The main drawback of these models is the lack of precision due to the difficulty of the integration of the biomechanical parameters into them. The second category of models are often directly associated with Finite Element Methods (FEM) because FEM are frequently applied to solve the problem formulation derived during the modeling process (usually partial differential equations, PDEs) based on continuum media mechanics.

2.2.1 Motion of a single organ: the lungs

Various physical and geometrical models have been proposed, focuses primarily on the lung modeling as a central organ for respiration. Lung inflation is due to the breathing muscles (diaphragm, outer intercostal muscles) contract and the thoracic cavity expands. As a consequence, the intrapleural pressure takes larger negative values. First, the most studies on modeling lung behavior considered lung tissue to be homogeneous and isotropic, where the bronchial tree and pulmonary vessels (Inner lung structures) are ignored [Al-Mayah 2009, Werner 2009, Villard 2005, Werner 2009]. Also, the simulations are quasi-static and usually the inertia effects are neglected.
In [Al-Mayah 2009], the authors have investigated the effect of the sliding of the lungs inside chest cavities on the accuracy of modeling lung's motion for seven patients. A 4D CT scans images were used to determine the optimal material parameters and coefficient of friction between the lung and the pleural surface. The optimization was based on minimizing the residual error of the predicted superior-inferior (SI), in the left-right (LR) and anterior-posterior (AP) of bronchial bifurcations identified on the images and including the contact model with a frictionless surface. Hyperelastic material properties are used for the lungs where the stress-strain plot is based on the experimental investigation on human lung tissues conducted by [Zeng 1987]. The model includes the body, lungs, and tumor behaviors (Fig.2.9).
Other methods based on contact-impact analysis have been applied to simulate the interaction between the lung and the surrounding tissues [Ilegbusi 2014]. These methods incorporates a pre-computation of surface displacements, i.e. lung boundary displacements are determined prior to the actual biomechanical modeling. Generally, the authors applied as displacement or Dirichlet boundary conditions for the lungs surfaces. The Figure 2.10 illustrates two boundary condition concepts commonly applied for biomechanical modeling of lung ventilation [Ilegbusi 2014]. The first approach is to pre-compute lung surface displacements (orthogonal projection) prior to the biomechanical modeling. Then, the displacements are specified as Dirichlet boundary condition [Didier 2007, Eom 2009, Nakao 2007, Werner 2008, Werner 2009]. In the second approach, to simulate the effect

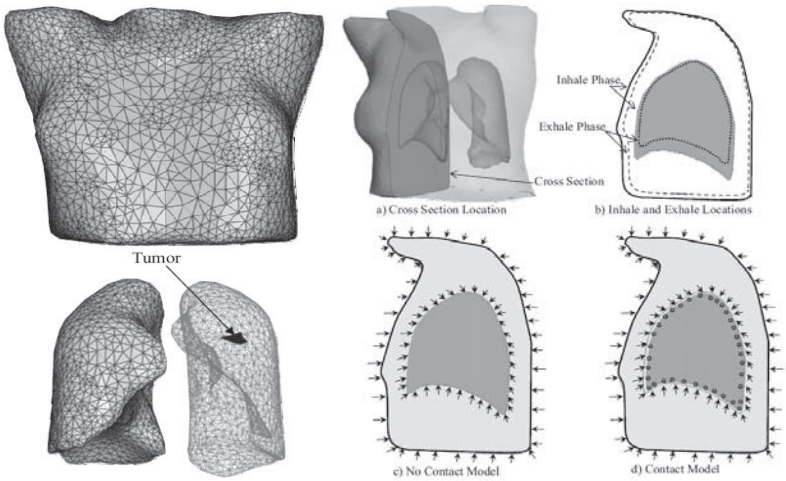

Figure 2.9 – Model components including body, lungs, and tumor. In the model without the contact surface; these displacements are applied to the lung's nodes directly since they are attached to those of the chest cavities. However, in the contact model; the boundary conditions are applied to the chest cavity nodes, not to the lungs, allowing sliding of lungs inside chest cavities. (figure taken from [Al-Mayah 2009]).

of the intrapleural pressure, the forces are applied to the lung boundary along the surface normal and tangential forces to simulate the sliding motion of the pleura along a limiting final geometry (final breathing state)[Ehrhardt 2013]. Various studies simulate the lung expansion during the inhalation by a uniform negative pressure and reaches the target surface (rigid) at the final state of breathing (e.g. end inspiration (EI)) [Villard 2005, Villard 2004, Villard 2005, Werner 2008, Werner 2009]. The contact between the rigid final geometry and the expanded lungs is simulated and modeled as frictionless [Ehrhardt 2013]. The authors [Werner 2009] have proposed similar approach based on finite element model, where tumor and lung tissue were assumed to be isotropic, homogeneous, and linearly elastic. In their study, They reported that lung tumor size and location influenced the simulation results, and that accuracy decreased in the region surrounding the tumor applied on 12 lung cancer patients (Fig.2.11).

In this paper [Tehrani 2015], the authors present a physics-based modeling method of respiratory motion over a complete normal breathing cycle, based on 4DCT data of four patients. To avoid multiple geometric smoothing procedures, an intermediate non-uniform rational B-spline NURBS surface representation was used. A nonlinear hyperelastic material model is used together with generic pressure-volume P-V curves and pleural sliding. The finite element model has been validated using 48 landmarks from the CT data without any tuning methods of finite element modeling parameters.

[Eom 2009, Eom 2010] have proposed finite element model of the lung based on the mechanical behavior described by [Zeng 1987] including the pleural sliding. The model includes a thoracic cavity, lung tumor and lungs (Fig.2.12). The lung tissue assumed homogenous isotropic hyper-elastic model. A frictionless contact condition assumed between the lung

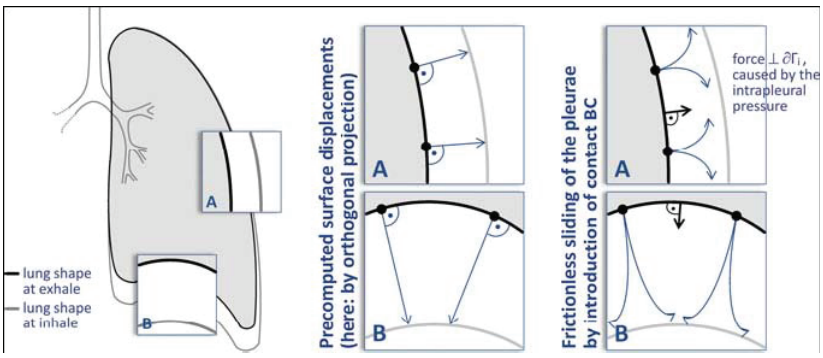

Figure 2.10 – Illustration of two boundary condition (BC) concepts commonly applied for biomechanical modeling of lung ventilation. The first approach is to pre-compute lung surface displacements prior to the actual biomechanical modeling process. In the second approach, the forces are applied to the lung boundary are along the surface normal and also the motion of the lung surface points are allowed to slide along a limiting geometry (final breathing phase). (figure taken from [Ehrhardt 2013]).

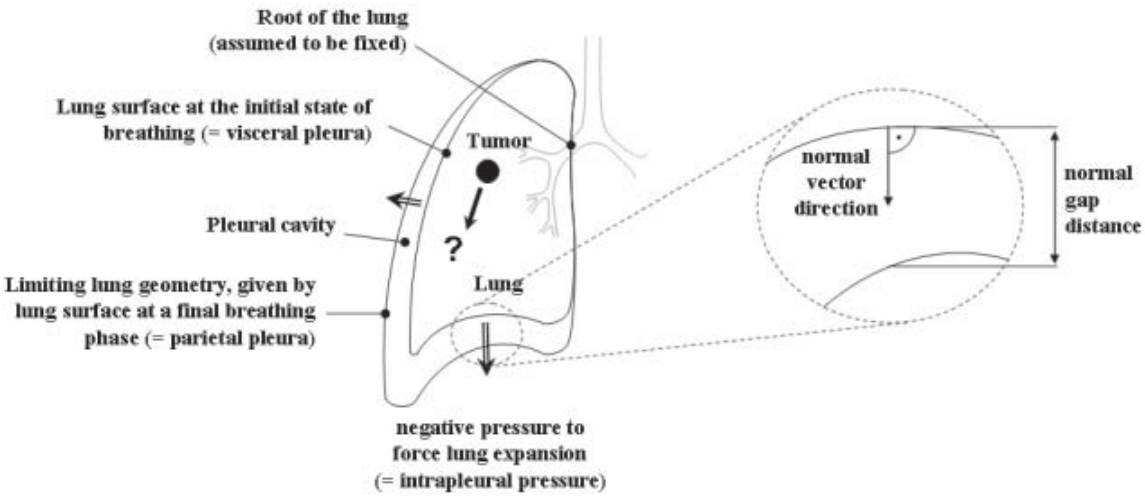

Figure 2.11 – Illustration of the anatomical boundary conditions (figure taken from [Werner 2009]).

and chest wall. Pressure is uniformly applied to the surface of the lungs. Extracted pressure amplitudes for different breathing phases from the measured curves, PV representing the relationship between lung volume and transpulmonary pressure (= difference between alveolar and intrapleural pressure). The displacement results from the finite elements analysis were compared using landmarks from the CT scan images and only in the superior-inferior direction. The authors reported the average error over multiple breathing phases less than 3 mm.

Unfortunately, most of the time, the authors have used a single organ (lung) with non-realistic boundary conditions. Moreover, these simulations are static and do not take into

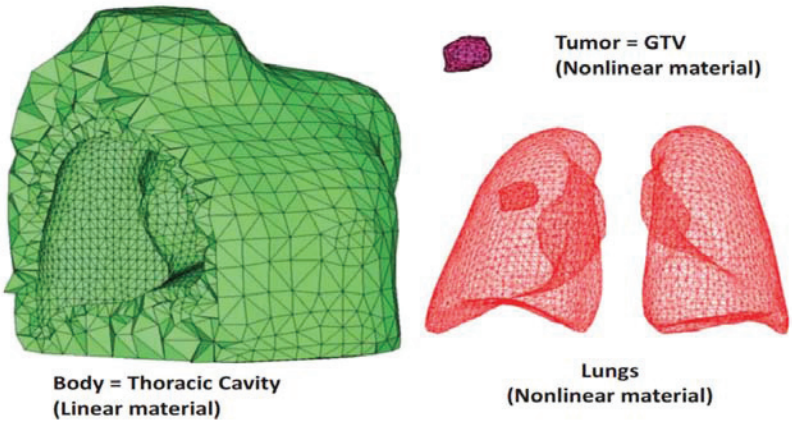

Figure 2.12 – Finite element model including a thoracic cavity, lung tumor and lungs (figure taken from [Eom 2010]).

account the dynamic variabilities of the respiratory system and none of these methods consider the real patient-specific physiological respiratory motion.

2.2.2 Motion of the respiratory system including the different organs

Lung motion is due to forces induced by the respiratory muscles of the diaphragm and rib cages. Some studies have been done to model the performance of the respiratory muscles (diaphragm and rib cages).
In an extension of the work [Villard 2005], the authors [Didier 2007] have used the same finite element model and investigated the kinematic effects of the ribs on the motion during a breathing cycle by using a finite helical axis (FHA) method (Fig.3.13). They computed the lung deformation induced by the motion of the ribcage and diaphragm.
Authors [Ladjal 2013b, Ladjal 2015] have proposed an extension of this work by including

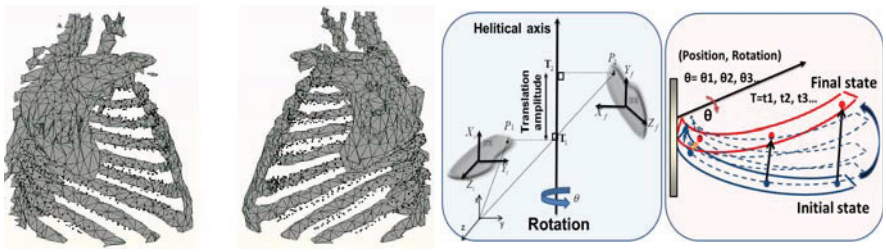

Figure 2.13 – Rib kinematics based on the Finite Helical Axis Method (FHAM). Left figure: two thorax sagittal views grey mesh: thorax segmented on the CT scans at an intermediate state of breathing black dots: computed rib cage position by inverse kinematics. Right figure: Finite helical axis method principle (figure taken from [Ladjal 2015]).

the physiological behavior of the diaphragm. The authors present an accurate patient-specific Finite Element (FE) model of the respiratory system including the diaphragm behavior and the complete thorax with musculoskeletal structure (Fig. 2.14), coupled with an inverse finite element method to determining automatically the appropriate tangential force of specific human diaphragm. The deformations of the human diaphragm and thorax are measured using a patient's CT scan images and compared to the personalized finite element model's predicted results. In their study, They reported that the linear elastic model can accurately predict diaphragm deformations.
In order to predict the type of the (geometrical or material) nonlinearities of the diaphragm, a quantitative comparison of the clinical data was applied on twelve patients [Ladjal 2015]. The authors have proposed two nonlinear hyperelastic models: the Saint-Venant Kirchhoff (SVK) and Mooney-Rivlin models. They reported that the nonlinear hyperelastic model Mooney-Rivlin of the diaphragm give as good results as the linear elastic model with large displacement (Saint-Venant Kirchhoff).
The authors in [Zhang 2016] have proposed a bio-mechanical model of the respiratory sys-

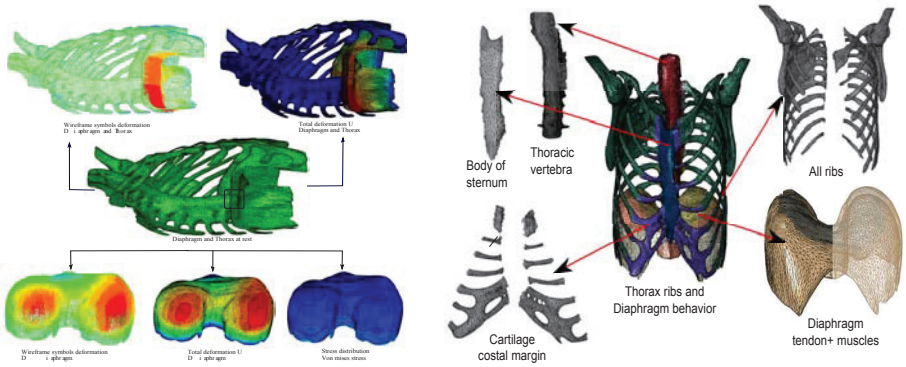

Figure 2.14 – Right: Different parts of the human diaphragm and thorax including: tendon and muscles tissues, ribs, Thoracic vertebra, costal cartilage margin, body of sternum. Left: Finite element simulation of the human respiratory system: stress distribution and the total deformation of the diaphragm including the thorax behavior (figure taken from [Ladjal 2015]).

tem (without the lung behavior) including the rib cage, intercostal muscles and diaphragm to monitor in the future the motion od the lungs (Fig. 2.15). To reproduce the muscle contractions, the authors have introduced the Hilltype transversely isotropic hyperelastic continuum skeletal muscle model and a static analysis has been performed. Unfortunately, the model is not patient specific and the experimental data for the active force/length relationship of the intercostal muscles and diaphragm are measured on an adult baboon.
Recently, the authors in [Fuerst 2015] have proposed patient specific biomechanical model of the lung motion from the end exhalation (EE) to the end inspiration (EI) based on 4D CT images, where the motion is not constrained by any fixed boundary condition. The authors have respectively applied different negative pressures on the pre-defined surface zones of thorax and diaphragm contacting with lungs, respectively, 4 and 16 pressure zones on the sub-diaphragm and thoracic cavity (Fig. 2.16). Then, the pressure force is transferred to the

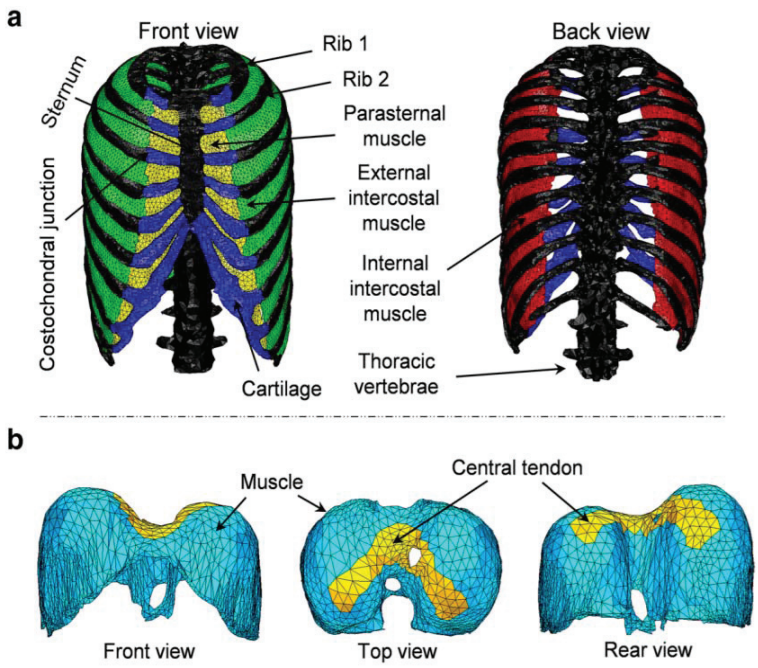

Figure 2.15 – Finite element model of the thorax: Respiratory muscles, rib cage and vertebrae and diaphragm (figure taken from [Zhang 2016]).

lung surface through a thorax/diaphragm/lung interaction model. The pressure values were estimated through an optimization procedure compared to CT images at end-inspiration (EI). The authors have reported that the sliding between the lung and the surfaces of thorax cavity and diaphragm was simulated as a frictionless contact problem. Unfortunately, none of these models and methods take into account the real physiological respiratory motion and its control or monitoring by the external parameters could be impossible.

2.3 Conclusion

Table.2.1 summarizes the comparison between the most biomechanical models of the respiratory system that have been used in the literature,that includes the material properties, the boundary conditions, the mechanical behavior (the elastic, hyperelastic models...), physiological parameters, the contact surface condition and different organs investigated in each model. This table illustrates the large variety values of the Young's modulus can be found in the literature. The lung tissue Young's modulus is reported at 0.1kPa to 10kPa in different studies [Al-Mayah 2011, Werner 2009, Nakao 2007, Villard 2005]. The material property parameters are almost impossible to measure in vivo and so few studies have been done on the mechanical properties of lung tissues [Al-Mayah 2011] . Most of the studies have been done in vitro, where the tissues are not in the conditions of respiration including oxygenation of cells and blood circulation. Moreover, tissue properties are also affected by various factors such as age, lung parenchyma distortion, or tissue location. In our work, we choose the mechanical properties of the lung tissues issued from [Al-Mayah 2011] and in the

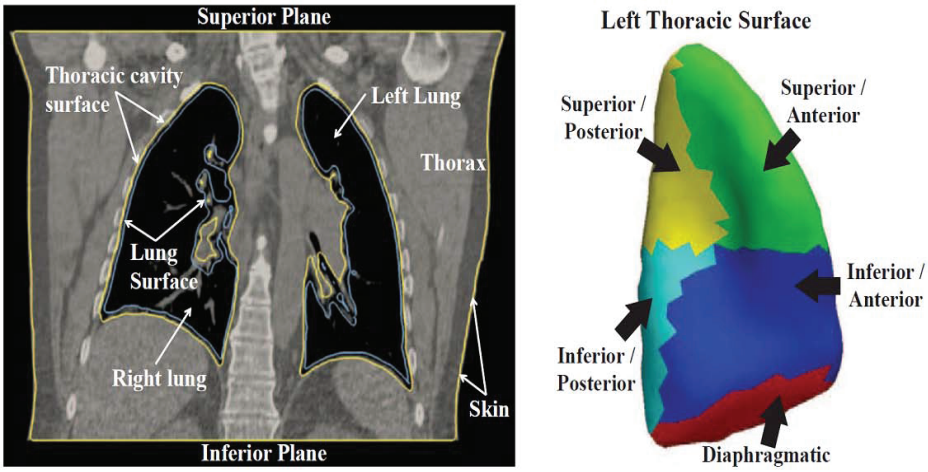

Figure 2.16 – Left: CT image showing the respiratory system of a patient. Right: patient specific biomechanical model of the lung motion used 4 and 16 pressure zones on the sub-diaphragm and thoracic cavity (figure taken from [Fuerst 2015]).

chapter 4, we will evaluated and compared the Young's modulus values often used in the literature and applied to simulate lung deformation to investigate the impact of mechanical properties uncertainties on the lung tumor motion prediction.

In this thesis, we present our developed patient-specific biomechanical model of the respiratory system for a whole respiratory cycle, based on 4D CT scans and personalized physiological compliance (pressure-volume curves) and constrained by real boundary conditions from the anatomy [Giroux 2017a, Giroux 2017b]. Our model includes the appropriate mechanical behavior and physiological parameters for each organ (lungs, diaphragm, the complete thorax with musculoskeletal structure, mediastinum, pleura and soft tissues. The mechanical role of the pleura described in part 2.1, allows a sliding between the different organs with very little friction. It is considered that the friction is negligible and we will model the role of the pleura by a frictionless sliding contact.

The amplitude of the lung pressure and diaphragm forces are specific, and differs from one patient to another and depends on geometrical and physiological characteristics of the patient. To determine these parameters at different respiratory states and for each patient, an inverse finite element (FE) analysis has been implemented to match the experimental data issued directly from 4D CT images, to the FE simulation results, by minimizing the lungs volume variations. The proposed approach (our model) can be monitored and correlated with two external parameters, the volume of air exchanged and the thoracic movement (rib kinematics).

This chapter has detailed and discussed the most commonly used biomechanical models of the respiratory system from the literature, and considered some of the issues relevant mechanical behaviors and physiological parameters for patient specific. The following chapter illustrates how to build the anatomical and biomechanical patient specific model of the respiratory system from 4D CT scan images and controlled by personalized physiological compliance. Then we present a new method for prediction the mechanical behavior of the

Reference	Data	Cycle	E (kPa)	ν	Material Properties	Boundary Conditions	Organs Modelized	Pressure Forces
Al-Mayah et al. 2008-2009-2011	CT4D	Exhale	3.74	0.35–0.499	Experimental data Zeng et al	Sliding without friction	Lungs	Surface displacement
Brock et al. 2005-2010	MRI	Exhale	5.0	0.45	SVK	Displacement surface	Lungs	Surface displacement
Didier et al 2007	CT4D	Inhale	0.823	0.25–0.35	SVK	Sliding without friction	Lungs Ribs Diaphragm	Uniform Kinematic Tangential Forces
Fuerst et al 2014 -2016	DIRLAB CT4D	Exhale	0.9-7.8	0.4-0.43	Experimental data Zeng et al	Sliding without friction	Lungs Ribs Diaphragm	Minimization of surface force
Werner et al 2009-2010	CT4D	Inhale	0.1–10	0.2–0.45	SVK	Sliding without friction	Lungs	Uniform
Eom et al 2009-2010	CT4D	Full	0.823	0.2-0.45	Experimental data Zeng et al	Sliding without friction	Lungs Thoracic cavity	Uniform P-V Generic
Our Model	DIRLAB CT4D	Full	0.823	0.33	SVK	Sliding without friction	Lungs Mediastinum Ribs Diaphragm	Uniform P-V specific Kinematic Forces Tangential Forces

Table 2.1 – List of most studies of biomechanical models for respiratory system that have been used in the literature.

diaphragm and lungs and controlled by personalized physiological compliance calculated from 4D CT images.

Chapter 3

Anatomical and biomechanical patient specific model of the respiratory system

This chapter focuses on biomechanical patient specific model of the respiratory system based on 4D CT scans and controlled by personalized physiological compliance. First, we propose and improve the geometrical modeling procedure for accurate reconstruction of respiratory system. This procedure consists of medical image segmentation, geometrical reconstruction of all relevant tissue of the respiratory system, generation of geometric approximations (boundary surfaces and volumetric meshes) of three-dimensional anatomy suited for finite element analysis and biomechanical simulation. We illustrate in this chapter, a new approach to predict the internal movements from two external parameters; the volume of air exchanged and the thoracic movement (rib kinematics). This approach is based on biomechanical patient-specific model of the respiratory system, constrained by real boundary conditions, coupled with an automatic tuning algorithm to compute lung pressures and diaphragm forces during a whole respiratory cycle. The geometrical (anatomy, boundary conditions and interactions...) and physiological (amplitude of the lung pressure, diaphragm force, ribs displacement ..) parameters are patient specific and determined at different respiratory states.

Contents

3.1 Introduction **34**

3.2 Patient-specific anatomical model of respiratory system **34**

3.2.1 3D segmentation and surface extraction 35

3.2.2 Surface mesh treatment 37

3.3 Patient-specific respiratory mechanics **40**

3.3.1 Input data and appropriate prediction of the mechanic behavior . . 41

3.3.2 Formulations of FEM 44
3.3.3 Geometrical Non-linear hyper elastic behavior: Saint-Venant Kirchhoff 46
3.3.4 Thoracic cage and rib kinematics 47
3.3.5 The boundary conditions (BC) 48
3.3.6 Automatic tuning and optimization 50
3.3.7 Dynamic Model 51
3.3.8 Density mapping 51
3.4 Conclusion of this chapter 52

3.1 Introduction

This chapter is structured as follows: first, we briefly describe a global methodology pipeline to build patient-specific biomechanical model of the respiratory system from medical images. Then, we present a new method for prediction the mechanical behavior of the diaphragm and lungs from 4D CT images, and some formulations of finite element method. Next, we describe our main contribution to the field, which consists in 4D dynamic and realistic biomechanical patient-specific model of the respiratory system, constrained by real boundary conditions, coupled with an automatic tuning algorithm to compute personalized lung pressures and diaphragm forces during a whole respiratory cycle and at any intermediate breathing states.

3.2 Patient-specific anatomical model of respiratory system

One of the major difficulties of the finite element method applied to computational biomechanics is the complexity associated with the building of patient-specific geometrical models. In this order, it is necessary to obtain a three-dimensional quality geometrical representation of anatomical shapes and generate good finite element meshes by good quality surfaces. Fig.3.1 presents a global methodology pipeline to generate patient-specific biomechanical model of the respiratory system from medical images. Firstly, we proceed by segmenting medical images. This step must be carefully performed, as segmentation errors can lead to a wrong estimation of the anatomy of the patient organs and therefore to a poor estimation of the electron density along the beam path which can lead to inaccurate dose calculations. Using marching cubes, we have extracted triangular surface meshes corresponding to each organ. These surfaces meshes are simplified and smoothed and then converted into tetrahedral meshes suited for finite element analysis. Due to the excessive number of nodes and large number of bad quality elements, which are common features in mesh based models, a CAD-based approach was developed. The volumetric meshes obtained from our developed pipeline were inserted into finite element ABAQUS solver in order to perform finite element analysis. In summary, the following steps are applied:

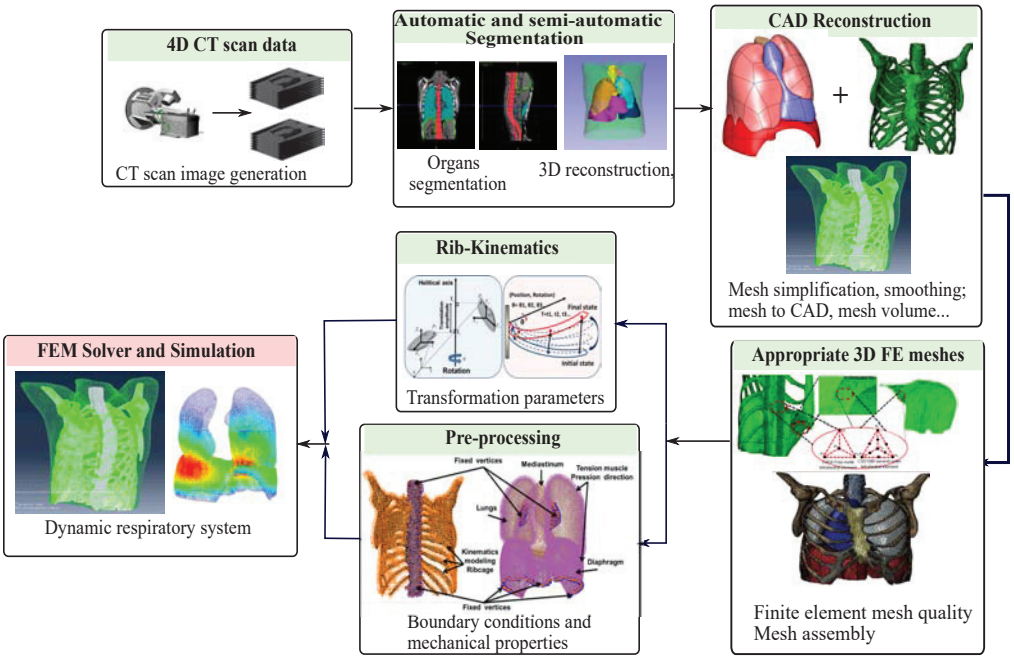

Figure 3.1 – Schematic of a global pipeline to generate patient-specific anatomical 3D models of the respiratory system from medical images (CT scan data) to finite element simulation including: the organs segmentation, 3D CAD reconstruction and 3D mesh generation, boundary conditions and appropriate behavior for different parts of the respiratory system.

1. 3D automatic, semi-automatic or manual segmentation of the thoracic organs from CT scan images and surface extraction
2. Surface mesh processing (decimation, smoothing...) and 3D NURBS model reconstruction in order to generate the appropriate mesh elements for finite element simulation.
3. Applying boundary conditions between thoracic organs (diaphragm and thorax) based on anatomical and physiological properties,
4. Finite element analysis of the respiratory system based on appropriate behavior laws for each organ (linear elastic, nonlinear hyperplastic, homogenous or heterogenous...).

3.2.1 3D segmentation and surface extraction

Various approaches for multi-organ segmentation have been developed based on CT images, which include gray-level thresholding, region growing or edge tracking. Five selected patients, from DIR-Lab Dataset [Castillo 2009] are selected, where the entire thorax was visible and with small and large breathing amplitudes (Table. 3.1).

In our thesis, the different organs are segmented semi-automatically using gray-level thresholds algorithms available within free software ITK-SNAP library [1]. It provides a dynamic interface for navigation and segmentation of 3D medical imaging data.

1. ITK-SNAP is a software application used to segment structures in 3D medical images

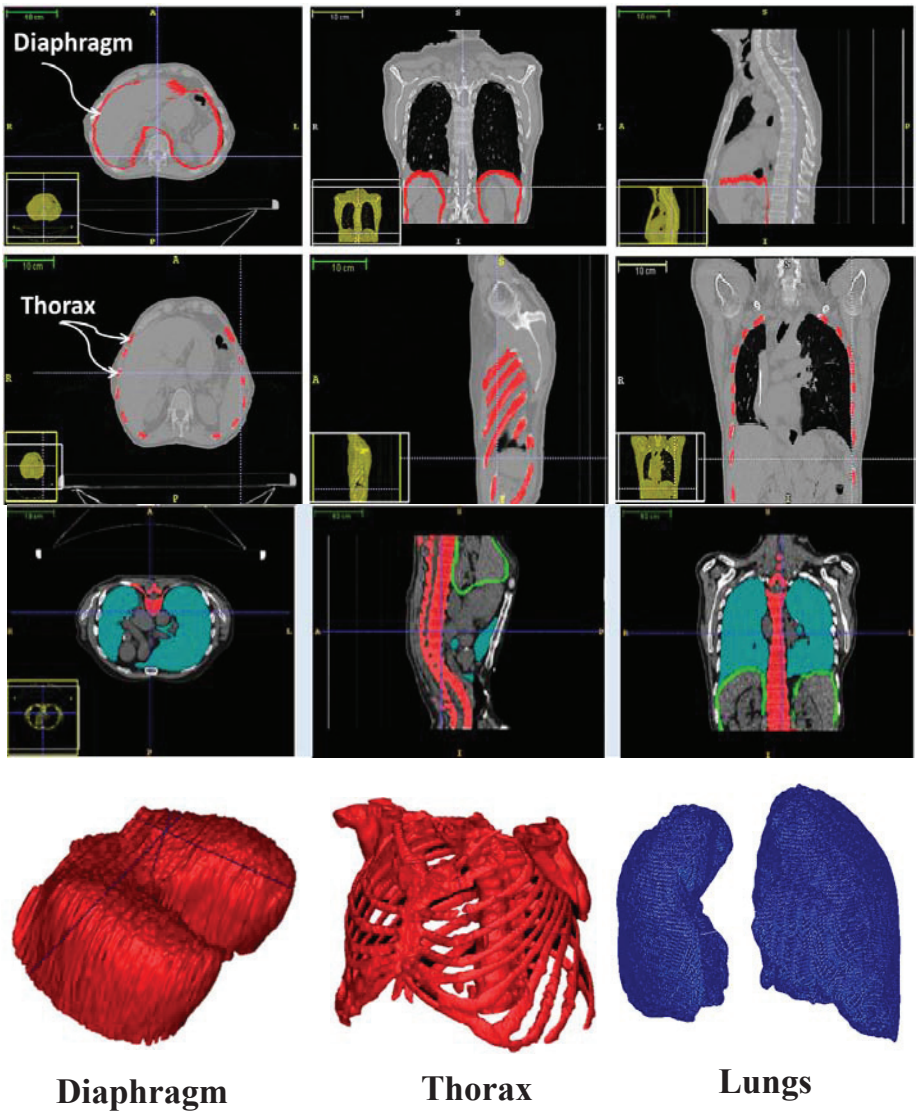

Figure 3.2 – 3D segmentation of the internal organs of the respiratory system: all ribs and diaphragm and 3D geometrical models issued directly from segmentation: human Ribcage and diaphragm.

The human diaphragm is a thin tissue, with thickness between $2mm$ and $5mm$. The automatic segmentation of the diaphragm is difficult and challenging due to the similar appearance of organs surrounding the diaphragm. Some authors attempts to propose a semi-automatic and automatic segmentation of the diaphragm dome and top surface [Li 2006, Yalamanchili 2010]. However, theses algorithms are not robust and not suitable for biomechanical modeling, because the quality and results need more time treatment and reconstruction. In this order, and for more precision, the diaphragm is segmented manually. The diaphragm muscles and tendon cannot be identified separately on CT images. According to [Cluzel 2000], the mean central tendon surface area is 143 cm^2, this area does

Patient	image dimension	Size of Voxels (mm)	volume between EE and EI (%)	Amplitude Diaphragm (mm)
1	256x256x94	0.97x0.97x2.5	12.8	10.1
4	256x256x99	1.13x1.13x2.5	14.6	20.2
6	512x512x128	0.97x0.97x2.5	25.4	24.1
9	512x512x128	0.97x0.97x2.5	13.4	12.5
10	512x512x120	0.97x0.97x2.5	16.7	22.3

Table 3.1 – Five selected patients from DIR-Lab Dataset [Castillo 2009], with small and large breathing amplitudes.

not vary to a large extent from one person to another.
For the thorax and all skeletal structure (the sternum, ribs and vertebrae), we have used a full automatic segmentation algorithm of the thorax and applied a threshold value to the images [Ladjal 2013b],[Ladjal 2015]. The intensity and volume thresholds were determined empirically from experimenting and adapted for different patients.
For the lungs and the external skin are segmented automatically using graylevel threshold algorithms available within ITK-SNAP library. However, the automatic segmentation of lung tumors remains quite challenging as they are directly in contact with healthy tissues and the different methods (automatic or manual) suffer from a lack of reproducibility. Thus, the correct segmentation can only be achieved by medical experts.
To extract the mediastinum structure, we have used the different segmentation masks of the lungs, thorax, the inner thoracic region and the diaphragm.
Finally, a 3D surface meshes for each organ are created automatically using a simple iterative algorithm (marching cubes algorithm) for creating a triangle mesh from an implicit function. The marching cubes algorithm is probably the most popular approach for extracting isosurfaces from a volumetric dataset. The basic idea to represent a volume, the space is divided into elementary cubes. Then we set a density threshold and we will go through the cube space. For each cube, we count the number of vertices above the threshold. Then, according to this number, a table makes it possible to register all the possible topologies of triangles displayed inside the cube. Each configuration corresponds to a set of facets drawn inside the volume. These triangles thus allow the representation of the surface of the volume to be determined Fig.3.5. Finally, theses meshes are saved and exported as *.stl* files.

3.2.2 Surface mesh treatment

These surface meshes (.stl files) were imported into MeshLab. MeshLab is an open source system for processing and editing 3D triangular meshes and offers a range of sophisticated mesh processing tools with a graphical user interface. Generally, the Marching Cubes algorithm produced very detailed surface meshes with a high number of small and irregular sized elements. Then, these surface meshes are simplified and smoothed based on Laplacian smoothing filter to rectify the step-like artifacts produced by the reconstruction algorithm and improving the surface mesh appearance. Fig.3.2. However, simplifications usually

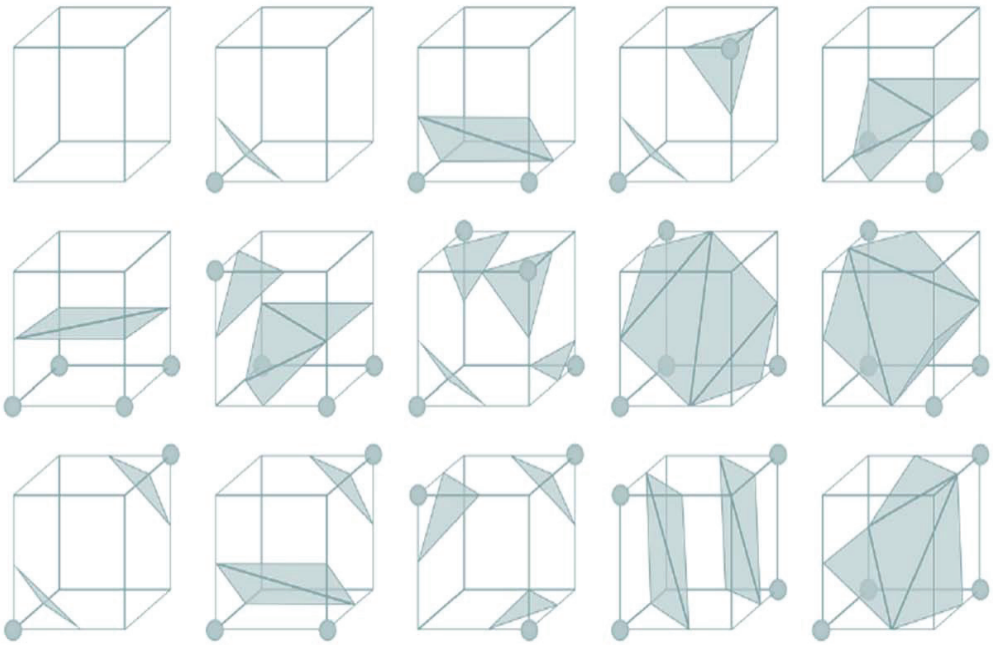

Figure 3.3 – Type of surface combinations for the marching cube algorithm.

involve elimination of less important details that unnecessarily increase the mesh complexity.

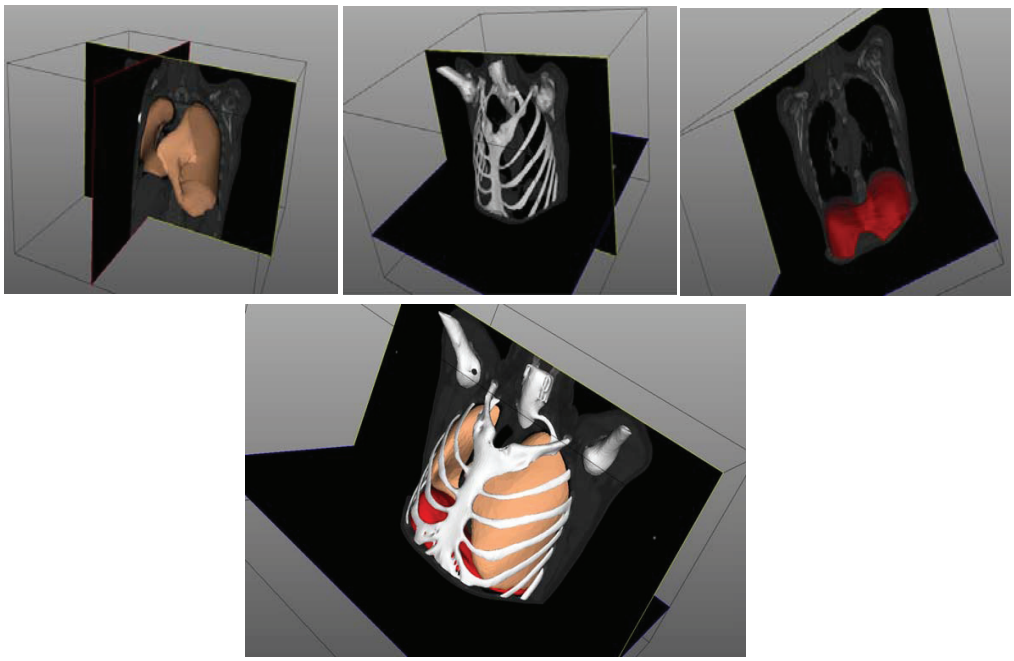

Figure 3.4 – Respiratory solid model superimposed onto CT scan volume images.

3.2.2.1 CAD surface construction

The proposed method takes advantage of the CAD description, which usually comes in the form of Non-Uniform Rational B-Splines (NURBS) patches. The NURBS is a geometric language which has been commonly used in computer graphics and Computer Aided Design, due to its great flexibility and precision for handling modeled shapes. Using CAD software, NURBS curves can be defined that follow the anatomical details of the structure. This transformation from surface elements to a NURBS-based representation allows for greater control of the shape and quality of the resulting finite element mesh. The construction of tetrahedral meshes from triangular surface meshes gives, in most cases, undesirable results, and may have intersections and penetrations between the meshes (Fig. 3.5) . Moreover, this poses a real problem in order to correctly model the contacts and the slides between the meshes. To overcome these difficulties, we can generate for each organ, by interpolation of the adjusted iso-surface mesh, a discrete set of surface patches that form a solid model based on non-uniform rational basis-splines (NURBS) surfaces (Fig. 3.6) . For more information about non-uniform rational basis-splines (NURBS) surfaces, please see the Appendix C. Finally, the export model is saved in STEP (STP) format or IGES (IGS) format. The choice of format depends on the compatibility with the pre-processing software of the finite element analysis (FEA) program (Abaqus software).

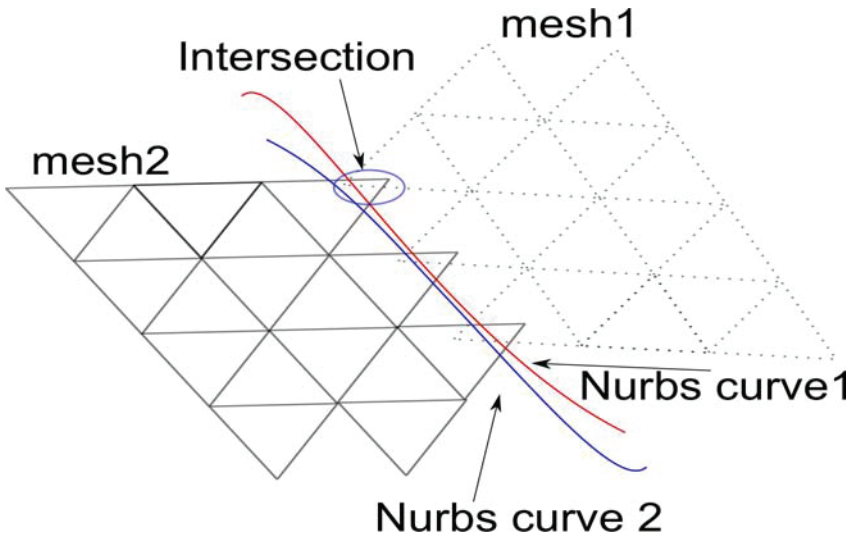

Figure 3.5 – An example for 2D triangle meshes intersection and approximated by NURBS curves.

3.2.2.2 Generation of the finite element mesh

After 3D solid reconstruction, the organs solid models are superimposed over original CT scan volume images with respecting the size and organ contacts Fig. 3.4. Then, the different structures are meshed with tetrahedral elements. The mesh affects the accuracy, convergence and speed of the computational process. A more precise and efficient finite element mesh results in a more accurate and faster solution. The generation of poor meshes

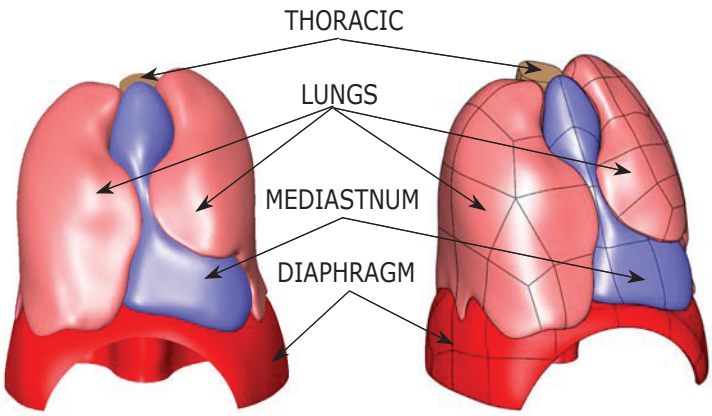

Figure 3.6 – Geometrical patient specific of the respiratory system with NURBS (Non-Uniform Rational Basis Splines) including: diaphragm, thorax, mediastinum and lungs

would lead to the formation of incorrect results. In this context, we have chosen and compared two types of tetrahedral elements (Fig.3.7):

— The first-order tetrahedra (C3D4), are usually used when stiff, and extremely fine meshes are required to obtain more accurate results than the coarser mesh.

— The second-order, the modified 10 node elements (C3D10) take advantage of automatic triangular and tetrahedral mesh generators and are robust for large deformation problems and contacts, but they necessitate more computing time.

The quality of the mesh plays a significant role in the accuracy and stability of the numerical computation. In our study, the mesh quality is performed using Abaqus packages. By default, poor quality elements are those elements with one (or more) of some criteria, for example:

— Ratio of maximum side length to minimum side length is larger than 10

— Minimum interior angle is smaller than 20 degrees

— Maximum interior angle is larger than 120 degrees

— Jacobian should be greater than 0.6

3.3 Patient-specific respiratory mechanics

Most biological soft tissues exhibit both linear elastic and hyper-elastic nonlinear mechanical response, under physiologic forces[Ladjal 2013a, Ladjal 2013b, Ladjal 2015]. Generally, the linear elasticity is used for the modeling of deformable materials, mainly because the equations remain quite simple and the computation time can be optimized. For the hyper-elastic nonlinear behavior, the Mooney-Rivlin (MR) and Saint-Venand Kirchoof (SVK) are commonly used to model soft tissues.

In the present section the mechanical behavior analysis and the choice of an appropriate linear or nonlinear model for the diaphragm and lungs models will be investigated. For this analysis, the statistical studies on the different strain deformation are performed on different patients to identify and to predict the type of the nonlinearities (large stress or

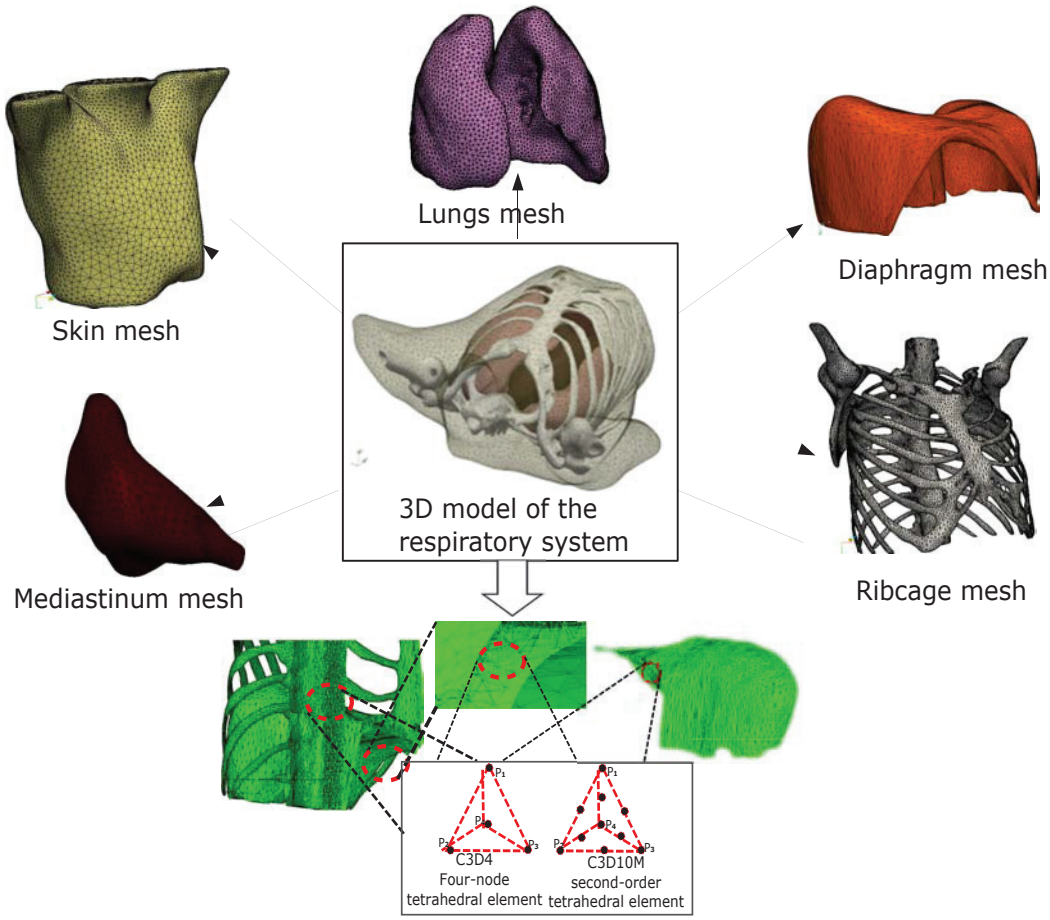

Figure 3.7 – Different parts and 3D tetrahedral meshes of the human respiratory system using two types of tetrahedral elements: The first-order tetrahedra (C3D4) and the modified 10 node elements (C3D10).

large strain) of the human diaphragm and lungs.

3.3.1 Input data and appropriate prediction of the mechanic behavior

In this section, we try to predict the mechanical behavior of the lungs and the diaphragm tissues, in order to identify the type of nonlinearity (geometrical or material nonlinearity). There are basically two types of non-linearities: material nonlinearity and geometric nonlinearity, but sometimes contacts are also refereed to as being nonlinear. For this reason, we assuming if the rate of global deformations between the initial state and the final state is less than 10%, then we can assume and simplify the mechanical behavior by a simple hyperplastic model (only geometric nonlinearity). We will evaluate this hypothesis by comparing the predicted behavior with other more complex models including the material nonlinearity and geometric nonlinearity (as mooney rivlin model). For more information concerning the hyperplastic models one can refer to Appendix A.

Table 3.2 – Experimental data analysis: Quantification of the deformation of the human diaphragm based on 4CT scan data for twelve patients, $\varepsilon_1 = \frac{l-l_0}{l_0}$, $\varepsilon_2 = ln\left(\frac{l}{l_0}\right)$, $\varepsilon_3 = \frac{1}{2}\left(\frac{l^2-l_0^2}{l_0^2}\right)$

Patients	ε_1	ε_2	ε_3
P1	6,31%	2,83%	6,11%
P2	5,49%	2,45%	5,34%
p3	3,97%	1,76%	3,89%
P4	8,07%	3,65%	7,74%
P5	7,56%	3,41%	7,27%
P6	3,98%	1,70%	4,06%
P7	6,26%	2,81%	6,06%
P8	9,23%	4,20%	8,80%
P9	6,59%	2,96%	6,38%
P10	5,41%	2,41%	5,26%
P11	5,64%	3,13%	5,13%
P12	7,04%	3,30%	5,43%
(Mean $\pm SD$)%	6,30 $\pm 1,17$	2,89 $\pm 0,56$	5,96 $\pm 1,10$

3.3.1.1 A geometrical approach to estimate (predict) the diaphragm behavior

In order to predict the appropriate behavior of the diaphragm, we have used twelve 4D CT scan data sets covering the whole thorax of patients. Each 4D CT consisting several sets of 3D CT scans at different respiratory states (full exhalation, intermediate stage and full inhalation). The CT images voxel size is $1.17 \times 1.17 \times 3$ mm^3 with $512 \times 512 \times 130$ voxels respectively in the left-right (X), dorsoventral (Y) and craniocaudal (Z) directions. The physical behavior of soft tissue may be considered as linear elastic if its strain and stress remain small (less than 10% of the mesh size). Based on the 4D CT scan images, we have compared the geometry of the diaphragm at the end of inspiration(EI) and at the end of expiration (EF). To estimate the deformation, we have calculated the uniaxial strain deformation measured by: $\varepsilon_1 = \frac{l-l_0}{l_0}$. The large strain can be measured by the logarithmic strain also called natural strain $\varepsilon_2 = ln\left(\frac{l}{l_0}\right)$. Also, the Green-Lagrange strain is defined as: $\varepsilon_3 = \frac{1}{2}\left(\frac{l^2-l_0^2}{l_0^2}\right)$, where l_0 is the original length of the undeformed mesh and l is the length of the deformed mesh in the different directions (see Fig.3.8). All calculations have been tested on 12 patients (Table 3.2). The Fig.3.9 shows the average value of errors ε_i and their standard deviation (SD), computed from the patients 4D CT scan data. We have obtained an average mean for all ε_i are less than 10%: $\varepsilon_1 = 6,30 \pm 1,17$, $\varepsilon_2 = 2,89 \pm 0,56$ and $\varepsilon_3 = 5,96 \pm 1,10$.

3.3.1.2 Lungs behavior

Various studies on modeling lung behavior (macroscopic) approximate lung tissue to be homogeneous, linear or hyper-elastic hyper-elastic and isotropic [Villard 2005, Al-Mayah 2008,

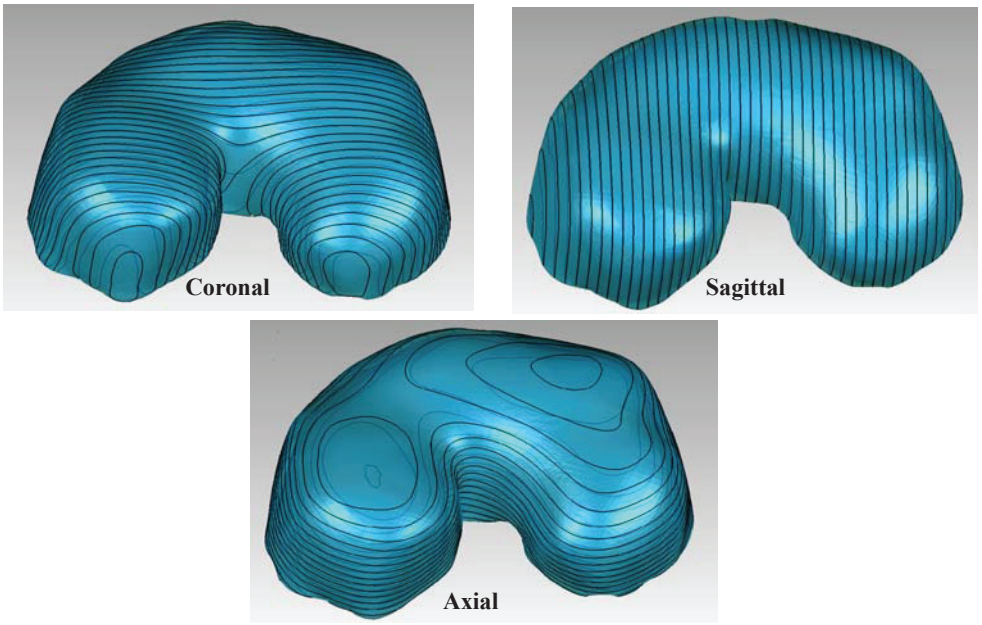

Figure 3.8 – Contour diaphragm.

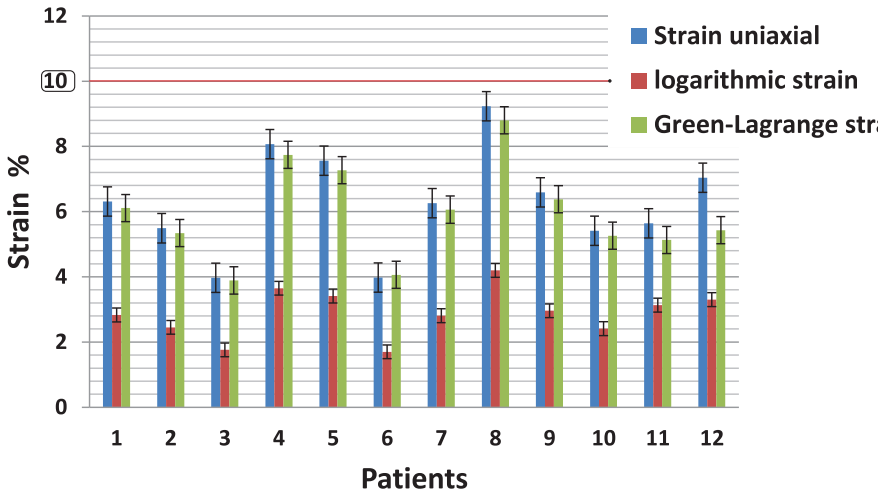

Figure 3.9 – Strain estimation: the uniaxial strain deformation ε_1, the logarithmic strain ε_2 and the Green-Lagrange strain ε_3 .

Al-Mayah , Fuerst 2015, Giroux 2017a, Giroux 2017b]. Based on five 4D CT images selected patients, with small and large breathing amplitudes. To estimate the deformation of the lungs for each patient, we have compared the geometry of the lungs at the end of inspiration(EI) and at the end of expiration (EF) in three directions (see Fig. 3.10). We have applied the same strategy as the diaphragm by calculating the three strains: uniaxial strain deformation ε_1, the large strain ε_2 and the Green-Lagrange strain ε_3 for right and

left lungs (see Fig.3.8). We suppose that the lung mechanical behavior may be considered as linear elastic if its strain and stress remain small (less than 10% of the mesh size). The

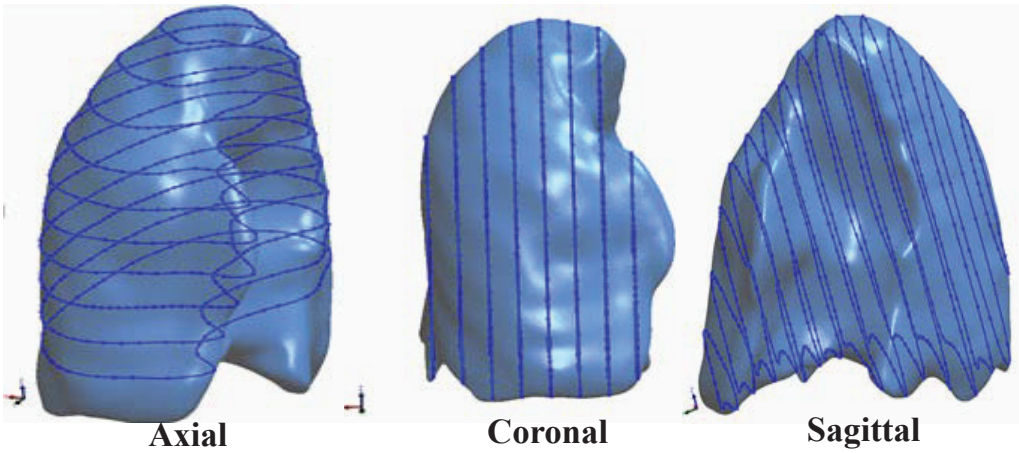

Figure 3.10 – Contour lungs.

figure (Fig.3.11) shows the average value of errors ε_i and their standard deviation (SD). We have obtained an average mean error for all lungs ε_i are less than 10%.

Finally, these results confirm that the approach of small deformations (with the large displacement) may be globally maintained in the modeling of the diaphragm and lungs (typically ε_i less than 10% of the mesh size). In the following study and based on our prediction, the lungs and diaphragm tissues are assumed to be a hyper-elastic St Venant-Kirchhoff material (small deformations and large displacement).

3.3.2 Formulations of FEM

Finite Element Method (FEM) can provide a great insight into the mechanical behavior of the organs, since they are based on the biomechanical material properties, complex geometry of organs and anatomical boundary conditions.
Using classical notations, for an isotropic elastic or hyperelastic material the elastic energy, noted W, can be written as:

$$W(\mathbf{E}) = \frac{\lambda}{2}\left(tr\mathbf{E}\right)^2 + \mu\, tr\left(\mathbf{E}^2\right) \tag{3.1}$$

where $\mathbf{E}$ is the Green-Lagrange strain tensor, λ and μ are the Lame's coefficients.
The Green-Lagrange strain tensor can be written as:

$$\begin{aligned} \mathbf{E} &= \frac{1}{2}(\mathbf{F}^T\,.\,\mathbf{F} - \mathbf{I}) \\ &= \tfrac{1}{2}\left(\mathbf{grad}\,\underline{U} + \mathbf{grad}^T\,\underline{U} + \mathbf{grad}^T\,\underline{U}\,.\,\mathbf{grad}\,\underline{U}\right) \end{aligned} \tag{3.2}$$

$\left[\mathbf{I}\right]$ is the identity matrix
A displacement $\underline{U}$ based finite element solution is obtained with the use of the principal of virtual works. For small deformations, the Green-Lagrange strain tensor is linearized into

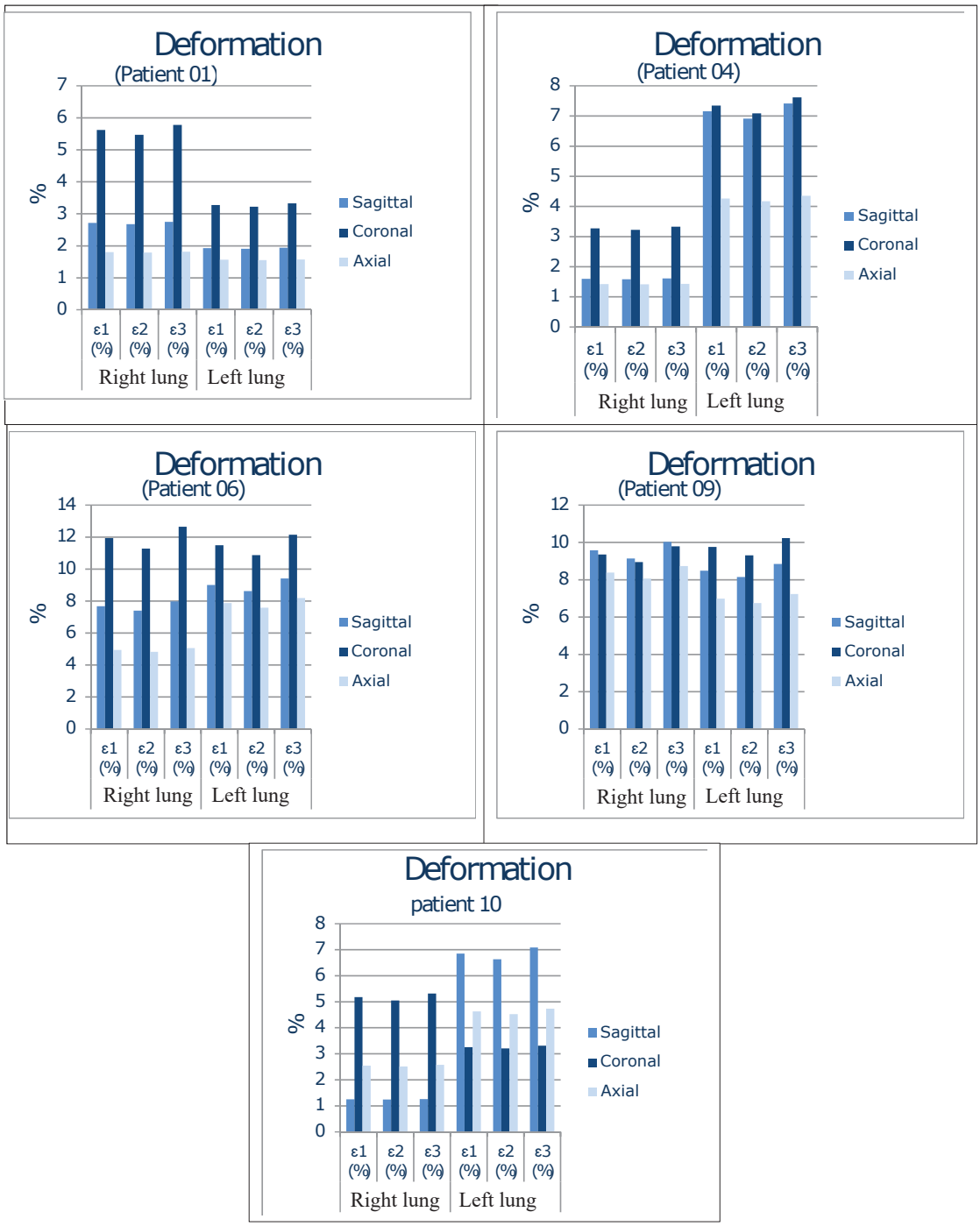

Figure 3.11 – Contour lungs.

the infinitesimal strain tensor $\left\{\boldsymbol{\varepsilon}\right\}$:

$$\left\{\boldsymbol{\varepsilon}\right\} = \tfrac{1}{2}(\mathbf{grad}\,\underline{U} + \mathbf{grad}^T\,\underline{U}) \tag{3.3}$$

The relation between the stress tensor and the strain tensor (Hooke's law), for isotropic material and for linear deformation, can be written:

$$\left\{\boldsymbol{\varepsilon}\right\} = \frac{1+\nu}{E}\sigma - \frac{\nu}{E}tr(\sigma)Id \tag{3.4}$$

E: Young's modulus and ν: Poisson's coefficient, other expression can be written, introduce Lame's constants, where μ:Shearing coefficient and λ: Compression coefficient.

$$\mu = \frac{E}{2(1+\nu)} \qquad \lambda = \nu\frac{E}{(1-2\nu)(1+\nu)} \tag{3.5}$$

In our work, the respiratory system are the volume object, these structures are meshed with three dimensional (3D) tetrahedral element. The relation between the Cauchy stress tensor and the linearized strain tensor is written with Lame's coefficient in condensed vector notation as :

$$\left\{\boldsymbol{\sigma}\right\} = \lambda\left(tr\left\{\boldsymbol{\varepsilon}\right\}\right)\left[\mathbf{I}\right] + 2\,\mu\left\{\boldsymbol{\varepsilon}\right\} \tag{3.6}$$

where $\left[\mathbf{I}\right]$ is the identity matrix.
This relation can be written in matrix form. We can write the following relationship between stress and strain as follows:

$$\left\{\boldsymbol{\sigma}\right\} = \left[\mathbb{C}\right]\left\{\boldsymbol{\varepsilon}\right\} \tag{3.7}$$

with

$$\left[\mathbb{C}\right] = \begin{bmatrix} \lambda+2\,\mu & \lambda & \lambda & 0 & 0 & 0 \\ \lambda & \lambda+2\,\mu & \lambda & 0 & 0 & 0 \\ \lambda & \lambda & \lambda+2\,\mu & 0 & 0 & 0 \\ 0 & 0 & 0 & 2\,\mu & 0 & 0 \\ 0 & 0 & 0 & 0 & 2\,\mu & 0 \\ 0 & 0 & 0 & 0 & 0 & 2\,\mu \end{bmatrix} \tag{3.8}$$

The principle of virtual work applied to a single tetrahadron T^{τ} leads to the elementary stiffness matrix $\left[\mathbf{K}^{\tau}\right]$ such that the elementary nodal force vector acting on a tetrahedron is:

$$\left\{\boldsymbol{f^{\tau}}\right\} = \left[\mathbf{K}^{\tau}\right]\left\{\boldsymbol{u^{\tau}}\right\} \tag{3.9}$$

For more information concerning the principle of mechanical resolution by the Finite Element Method (FEM) one can refer to Appendix B.

3.3.3 Geometrical Non-linear hyper elastic behavior: Saint-Venant Kirchhoff

The Saint-Venant Kirchhoff law extends the Hooke's law for large displacement. The relation between the second Piola-Kirchhoff stress tensor, the Green-Lagrange strain tensor and the rate effect leads to:

$$\mathbf{S} = \lambda\,(tr\,\mathbf{E})\,\mathbf{I} + 2\,\mu\,\mathbf{E} \tag{3.10}$$

where $\left[\mathbf{I}\right]$ is the identity matrix, $(\mathbf{E})istheGreen - Lagrangestraintensor$,$\lambda$ and μ are the Lame's coefficients. for more information concerning the hyperelastic models, we can see the Appendix A.

3.3.4 Thoracic cage and rib kinematics

In our thesis, we have considered the thoracic cage including all skeletal structure: all ribs and associated costal cartilages, the sternum and the thoracic vertebrae (Fig. 3.12). The

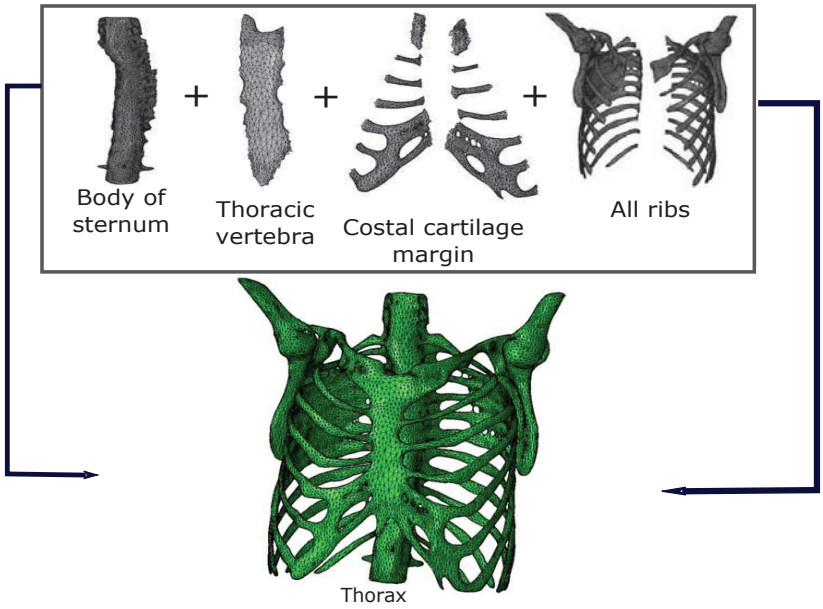

Figure 3.12 – Different parts and 3D tetrahedral meshes of the thorax including:ribs, thoracic vertebra, costal cartilage margin, body of sternum.

ribs are considered as articulated rigid bodies. The motion of a rigid body between position 1 and position 2 can be characterized by an Euclidean transformation. Several authors have investigated the ribs kinematics. In [Wilson 2001], human ribs displacement has been studied and the transformation parameters have been defined using planes attached to the ribs. In our previous works [Didier 2007, Ladjal 2013b, Ladjal 2015], we have presented a methodology to study ribs kinematics, using the finite helical axis method. The ribs can be considered as rigid bodies in comparison to other surrounding anatomical elements, each rib transformation parameter is calculated automatically using rigid registration techniques, computed between the initial and final states (Fig. 3.13). Then, We used a linear interpolation of the transformation to predict the rib motion at any intermediate breathing states.

FHAM is used to represent three dimensional motion of the ribs described by a rotation (θ) about an axis and a translation (T) along an axis. The Fig. 3.13 shows the principle of the Finite Helical Axis Method (FHAM), where $P_1(X_i, Y_i, Z_i)$ is a coordinate system linked to a solid at an initial state and $P_2(X_f, Y_f, Z_f)$ is the same coordinate system after transformation.

$$\overrightarrow{P_1P_2} = 2\,\overrightarrow{k}\,\frac{tan\theta}{2} \times (\frac{\overrightarrow{T_1P_1} + \overrightarrow{T_2P_2}}{2}) + \overrightarrow{T_1T_2} \tag{3.11}$$

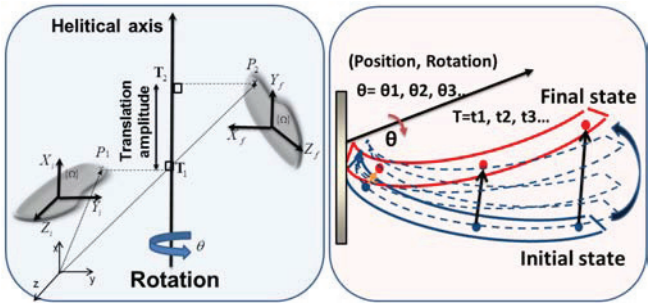

Figure 3.13 – Finite Helical Axis Method (FHAM) represent 3D motion of the ribs described by a rotation (θ) about an axis and a translation (T) along an axis : (Left) shows the principle of the Finite Helical Axis Method (FHAM) and (Right) shows the automatic rib positions computed by interpolation at any intermediate state (figure taken from [Ladjal 2015]).

Rib positions can then be computed by interpolation at any intermediate state.

$$\Big[\mathbf{P}\Big]_{ij} = \begin{bmatrix} \alpha + kx^2\beta & kxky\alpha + kz\gamma & ky\gamma + kxkz\beta \\ kz\gamma + kxky\beta & \alpha + ky^2\beta & -kx\gamma + kykz\beta \\ -ky\gamma + kxkz\beta & kx\gamma + kykz\beta & \alpha + kz^2\beta \end{bmatrix} \tag{3.12}$$

with $\alpha = cos(\theta)$, $\beta = 1 - cos(\theta)$, $\gamma = sin(\theta)$, kx,ky,kz: axis direction.

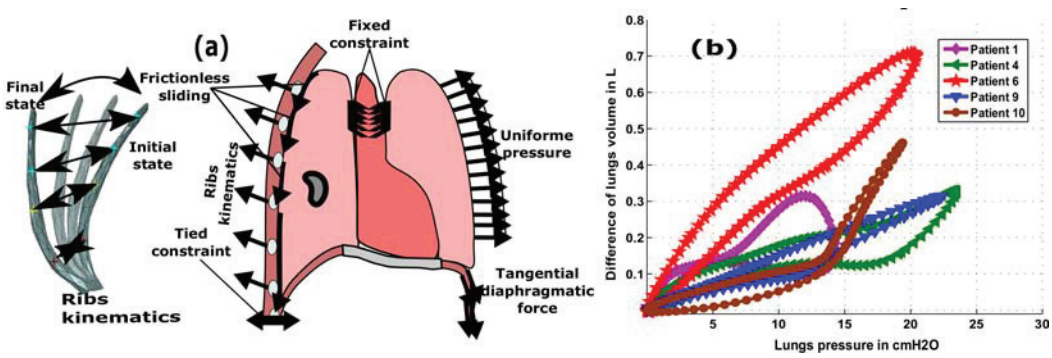

Figure 3.14 – The boundary conditions (BC) of our patient specific biomechanical model including rib kinematics (a), and the personalized Compliance (b).

3.3.5 The boundary conditions (BC)

The boundary conditions (BC) are inferred from the anatomy and identified by medical experts (Fig.3.14(a)). For the diaphragm, we have applied the radial direction of muscle forces, which corresponds anatomically to the direction of muscle fibers. The force is applied on the muscular part of the diaphragm and simple homogeneous dirichlet boundary condition is applied to the lower part of the diaphragm which is assumed to be fixed($\underline{U}$ =0), and the Lagrange multiplier's method is used for the contact model. In order to simulate

the sliding of the lungs, a surface-to-surface contact model is applied to the lung-chest cavity. The frictionless contact surfaces are used to simulate the pleural fluid behavior. All parameter values are illustrated in the chapter 4 (next chapter).
To simulate the rib cage kinematics, and automatic rigid registration algorithm has been developed from the patient's 4D CT: for each rib, an Euclidean transformation has been computed between the end inspiration (EI) and end expiration (EE) states. Then we have calculated the transformation parameters for each intermediate respiratory state. These parameters has been applied as displacement boundary conditions during the whole respiratory cycle. The different simulations and validation will presented next chapter applied on 4D CT scan images.
The originality of our work compared to the existing works is:

— The amplitude of the lung pressure and diaphragm force are patient-specific, determined at different respiratory states by an optimization framework based on inverse FE analysis methodology, using lung volume variation.
— The organs' masses have been computed from the voxelized CT attenuation values. Based on the principal of mass conservation
— the developed biomechanical respiratory model is monitored directly by simulated actions of the breathing muscles: the diaphragm and the intercostal muscles (the rib cage).

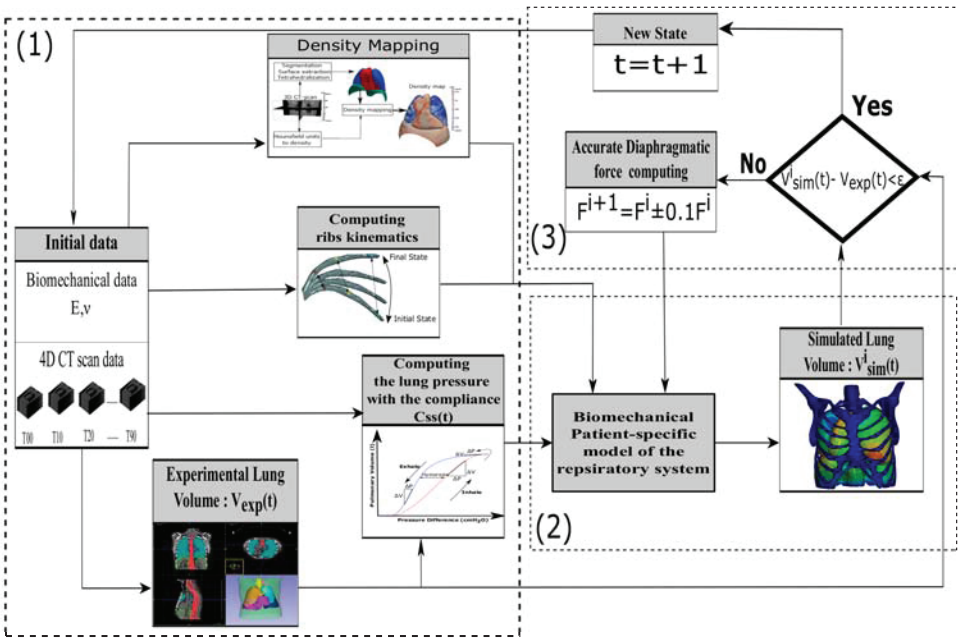

Figure 3.15 – Global computational framework patient-specific model of the respiratory system. The personalized diaphragm forces and the lungs pressure during the whole respiratory cycle and for each intermediate respiratory state are calculated automatically based on inverse finite element optimization.

3.3.6 Automatic tuning and optimization

Physiological parameters of the respiratory system are patient-specific and vary from one patient to other. Most values of these parameters were chosen heuristically due to the lack of experimental data. The schematic of the computational framework developed for this study is illustrated in Figure (Fig 3.15). This framework is designed to find and calculate automatically the personalized diaphragm forces and the lungs pressure during the whole respiratory cycle and for each intermediate respiratory state based on inverse finite element optimization. The optimization loops were achieved with a program coded in Python coupled within finite element Abaqus solver. Our proposed computational framework is illustrated in Fig 3.15. Besides data acquisition (4D scan images), there are three successive steps involved in this framework. The first step is the estimation of the initial parameters: the initial compliance, the initial segmented geometry, the organs mass computed from the voxelized CT images and the rib kinematics calculated by FHAM. In the second step, the biomechanical simulation (simulation loop) based on finite element analysis of the respiratory system is generated using the current parameters. In the third step, the optimization loop, in which the diaphragm forces and lung pressures are adapted and corrected until the volume lungs errors distance between the simulated lung volume (V_{sim}) mesh and the segmented lung volume (V_{seg}) mesh extracted from the CT scan images of the same respiration step is minimized. Thus, we have adopted the following computational procedure:

1. Initially, we have segmented the respiratory system at end inspiration (EI, the reference state). Also, we have segmented lungs at all states (10 states for a full cycle). Then, the model is controlled by a personalized pressure-volume curves (semi-static compliance), can be calculated as $C_{ss} = \frac{3(1-2\nu)}{E\,V_{t-1}}$. The semi-static compliance (C_{ss}) or a specific compliance (calculated previously in Chapter 2), based on the tissue properties; Young Modulus E and ν Poisson coefficient [Villard 2005, Al-Mayah 2008, Giroux 2017a] and the lung volume V_t at each step t (respiratory phases) calculated from 4D CT scan images (Fig 3.14(b)). For each respiratory volume V_t (from CT scan images), the internal lung pressure is computed. The algorithm starts with an initial estimate of the compliance, the initial geometry, the organs mass computed from the voxelized CT attenuation values [Manescu 2013] and the rib kinematics calculated by FHAM.
2. The simulation loop calculates the deformations of the respiratory system using a finite element method. The FE results were processed by the optimization program and compared to the CT images at different respiratory states. For each respiration phase, the optimization algorithm starts with two initial parameters (lung pressure, diaphragm force) and updates them iteratively until the lung volumes issued from the simulation matches real volumes provided by CT images and the maximum of the displacement of the node in contact between lung and diaphragm don't change between two different pressure. For the first iteration (i = 1), a weak diaphragmatic force is imposed for the first stage of breathing (t = 0). In the case of a respiratory step during the cycle, the imposed diaphragmatic force is equal to the previous one such that $F_0(t) = F_i(t-1)$. Then by minimizing the volume lungs errors, between the

V_t and the simulated volume (V_s), the appropriate diaphragm forces are computed. The iteration is terminated when the optimized parameters were found using the tolerance of 5% (This value has been chosen in comparison with an epsilon at 2% where the computational time was increased dramatically and an epsilon at 10% the displacement errors are larger then an epsilon at 2%. The squared error between the simulated and experimental data was used as an objective function to be minimized. If the objective function has not converged, the estimates of the parameters are updated, and the new parameters are fed back into the simulation loop.

3. Finally, the respiratory model is monitored directly by simulated actions of the breathing muscles: the diaphragm and the intercostal muscles behavior (the rib cage displacement).

3.3.7 Dynamic Model

The deformation of the organs is given by the displacement of the nodes according to the action of external and internal forces. The applied forces change in time and we have used a dynamic simulation using FEM. The equation of motion of a vertex v of the organs mesh can be written:

$$M^v \left\{ \ddot{\mathbf{u}}_v \right\} + \gamma^v \left\{ \dot{\mathbf{u}}_v \right\} + \sum_{\tau \in \mathcal{V}_v} \left(F_v^{int} \right) = F_{ext}^v \tag{3.13}$$

Where M^v, γ^v are respectively the mass and damping coefficients of each vertex. The $\mathcal{V}_v$ is the neighborhood of vertex v (i.e. the tetrahedra containing node v). The F_v^{int} are the internal forces calculated by FE method and the F_{ext}^v are the tangential imposed forces calculated as stated above. To solve the dynamic system, the implicit finite scheme has been chosen for more stability.

3.3.8 Density mapping

In our simulation, the density and mass of each tissue are patient-specific, calculated and determined directly from CT scan images, based on density mapping algorithm defined and developed in our previous work [Manescu 2013]. First, organs tetrahedral meshes are generated from segmented CT scanner images. Next, the Hounsfield values issued from CT scanner images are converted into density values that are mapped to these mesh nodes, respecting the principles of mass conservation(Fig. 3.16). The figure 3.16 shows a 2D example of calculating the mass of a mesh element as the sum of the masses of the overlapping volumes. Example of applying equation in a 2D space: $m(T_k) = m(I_k^1) + m(I_k^2) + m(I_k^4) + m(I_k^5) + m(I_k^6) + m(I_k^8) + m(I_k^9)$.

$$m(T_k) = \frac{vol(T_k)}{4} \cdot \sum_{l=1}^{4} \rho_l^k \tag{3.14}$$

where $\rho_l^k = \rho_k(S_l^k)$, $l = 1, ..., 4$ represent the mass density at the nodes of the tetrahedral element T_k.

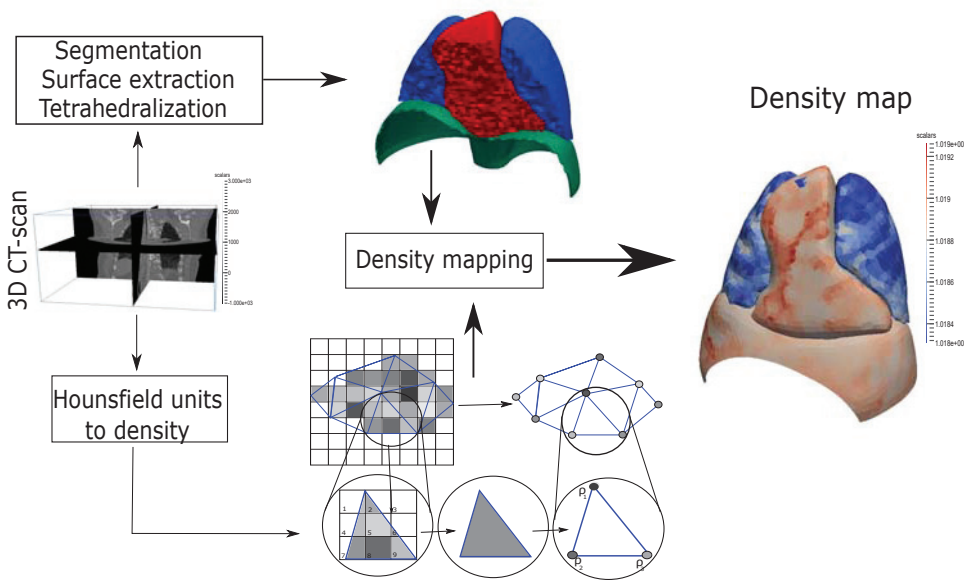

Figure 3.16 – Tetrahedral density map generation.The mass of a tetrahedral element equals the sum of the masses of volumes of intersection between the tetrahedron and the grid of voxels.

In order to calculate the mass of each tetrahedron, the tetrahedral mesh is intersected with the voxel grid. The mass of a tetrahedral element can be expressed as the sum of the volumes of intersection between the tetrahedron and the grid of voxels. For more information related to density mapping algorithm, one may refer to [Manescu 2013].

3.4 Conclusion of this chapter

In this chapter, we have presented an approach to internal movement monitoring with two external parameter, the volume of air exchanged and the thoracic movement (rib kinematics). Firstly, we have developed a geometric modeling pipeline to build 3D model of the respiratory system based on CAD approach, issued directly from medical image data, and adapted for biomechanical simulation. Then, we have investigated the impact of the non-linearity type (geometrical or material) to find the appropriate mechanical behavior of the organs (diaphragm and lungs), calculated directly from experimental data. Finally, we have presented and developed a biomechanical model of the respiratory system coupled with an inverse finite element analysis to determine the appropriate lung pressures and diaphragm forces for each patient, during a whole respiratory cycle and at different respiratory states. The following chapter presents a comparative study between our finite element simulation and experimental data (4D CT scan images).

Chapter 4

Simulations and evaluation

In this chapter, we present our simulations and results based on patient specific biomechanical model of the respiratory system. The qualitative and qualitative evaluations have been done by comparing the finite element simulation with the experimental data (4D CT scan images) on anatomical landmarks, at end inspiration (EI), end expiration (EE) states, and at each intermediate respiratory state. First, we present some metrics that are used to quantify and evaluate the accuracy of our model. Then mesh quality and mesh convergence study are presented. Then, to measure the precision of our biomechanical simulation, we have compared the anatomical landmarks position of the motion at the end of inhalation (EI) and the end of exhalation (EE) obtained from CT scan images and our finite element simulations. We present also and evaluate the impact of the rib kinematics on the accuracy of our model. Finally, we have investigated the impact of the nonlinearity and the impact different elasticity parameters (Young's modulus and Poisson's ratio) on the accuracy of our model.

Contents

4.1 Introduction **54**

4.2 Evaluation metrics **54**

4.2.1 Computation of landmark and surface errors 54

4.2.2 Lung tumor motion 54

4.3 Simulations and evaluation **56**

4.3.1 Contact stabilization 56

4.3.2 Mesh quality and mesh convergence study 57

4.3.3 Qualitative and quantitative comparison 58

4.3.4 Anatomical landmarks evaluation at end of inhalation (EI) and the end of exhalation (EE) 60

4.3.5 Anatomical landmarks evaluation at intermediate states between EI and EE 62

4.3.6 Mechanical parameters uncertainty assessment 65

4.3.7 Behavior uncertainty 70

4.3.8 Discussion and conclusion 71

4.1 Introduction

We have evaluated the model accuracy on five selected patients, from DIR-Lab Dataset [Castillo 2009], where the entire thorax was visible and with small and large breathing amplitudes. We have by compared the finite element simulation results on 300 landmarks, at end inspiration (EI), end expiration (EE) states, and 75 landmarks at each intermediate respiratory state. We have also evaluated the tumor motion and trajectory identified in 4D CT scan images on two selected patients (6 and 10) from the same Dataset DIR-Lab [Castillo 2009], where the tumor location is visible (see figure Fig.4.1). These trajectory are compared and evaluated with the trajectory obtained by FE simulation, during one complete breathing cycle [Giroux 2017a].

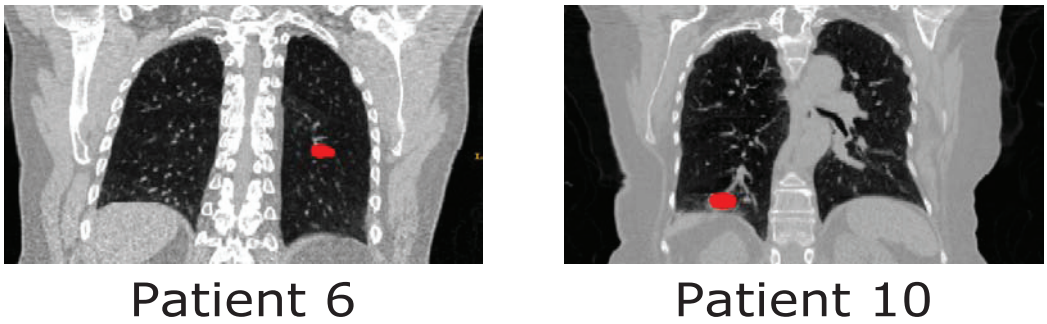

Figure 4.1 – Two selected patients (6 and 10) from DIR-Lab Dataset [Castillo 2009], where the tumor location is visible

4.2 Evaluation metrics

4.2.1 Computation of landmark and surface errors

In order to quantify the accuracy of the reconstructed organs, the surface error is the average distance between two triangle meshes. We have used the Hausdorff distance between is the average distance between two triangle meshes (X and Y), defined as:

$$d(X,Y) = max\left\{\sup_{y\in Y}\inf_{x\in X}\delta(x,y), \sup_{x\in X}\inf_{y\in Y}\delta(x,y),\right\}$$

The landmark error is the Euclidean distance between the landmark's simulated position (FEM) and the position at the target phase (medical images).

4.2.2 Lung tumor motion

To evaluate lung tumor motion, the lung tumor trajectories identified in 4D CT scan images were used as reference and compared with the target trajectories estimated from

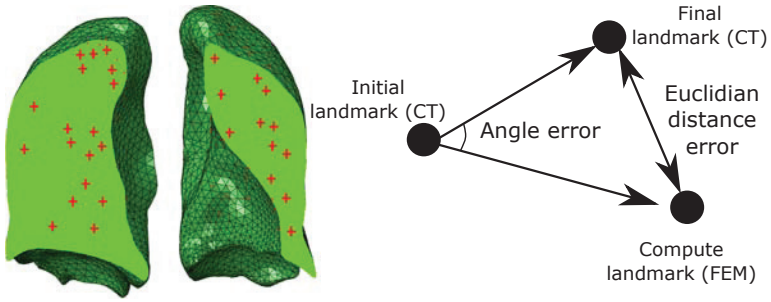

Figure 4.2 – Euclidean distance between the landmark's simulated position (FEM) and the position at the target phase (medical images)

finite element simulation without and within the optimization algorithm during the whole cycle of breathing (10 phases between the EI and EE). To track the lung tumor movement in 4D CT images, we have used the affine registration applied to the segmented lung tumor volume at different respiratory states (Fig.4.3). Then, the accuracy of the proposed tumor tracking method is evaluated by comparing and calculating the average Euclidean distance between the 3D mesh surface of the segmented tumor and predicted FE lung tumor.

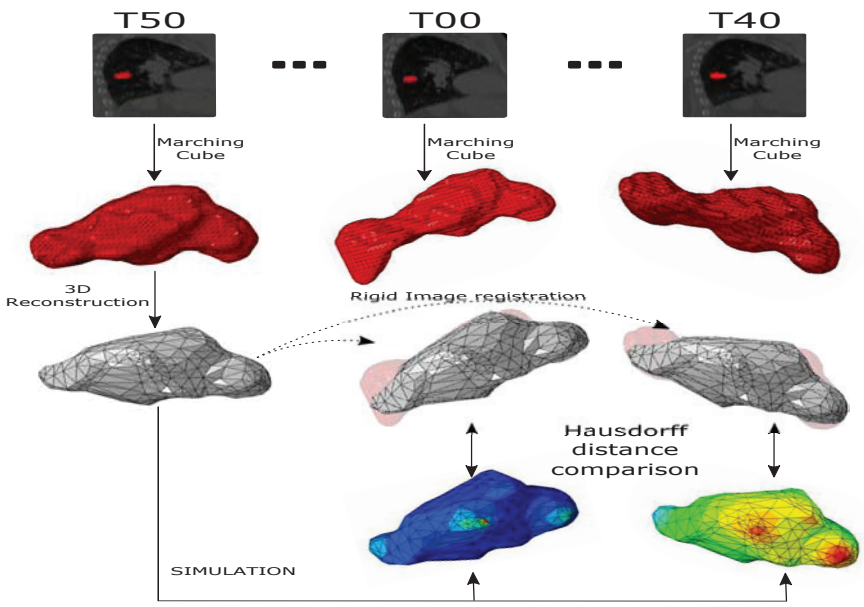

Figure 4.3 – Evaluate lung tumor motion: affine registration applied to the segmented lung tumor volume at different respiratory states

4.3 Simulations and evaluation

4.3.1 Contact stabilization

Firstly, it is important to verify that the presence of contact stabilization does not significantly alter our simulations. We have compared the energy dissipation due to stabilization (ALLSD) with the internal energy of the structure (ALLIE). Ideally the amount of stabilization energy should be a small fraction of the internal energy. The energies involved in the process have been plotted with respect to time. Fig. 4.4 shows the variation of the stabilization and internal energies. We can see, that the dissipated stabilization energy is indeed small.

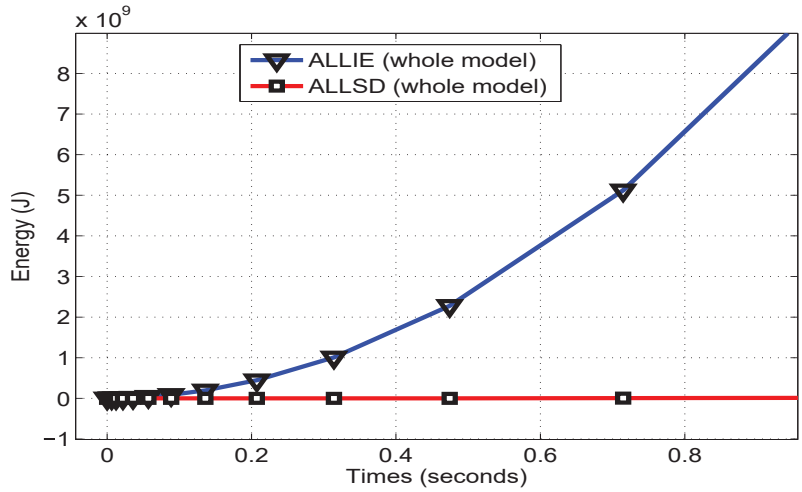

Figure 4.4 – Stabilization and internal energies: comparison between the energy dissipation due to stabilization (ALLSD) against the internal energy of the structure (ALLIE)

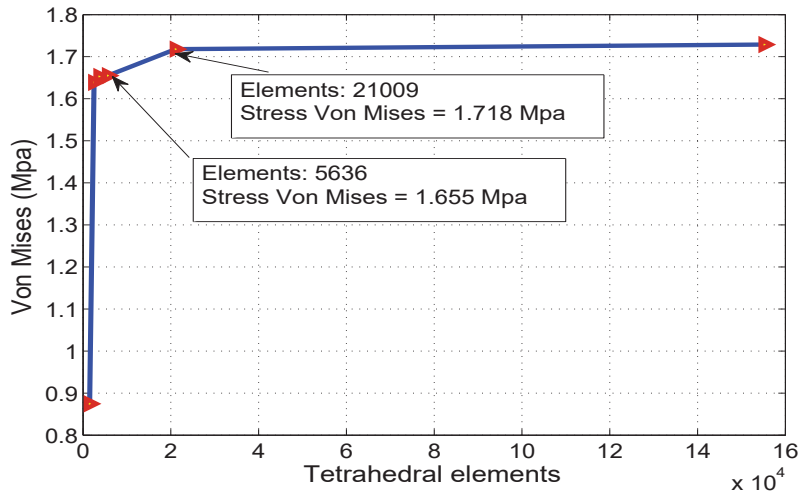

Figure 4.5 – Mesh convergence study: Stress Von Mises computed for different resolution of meshing.

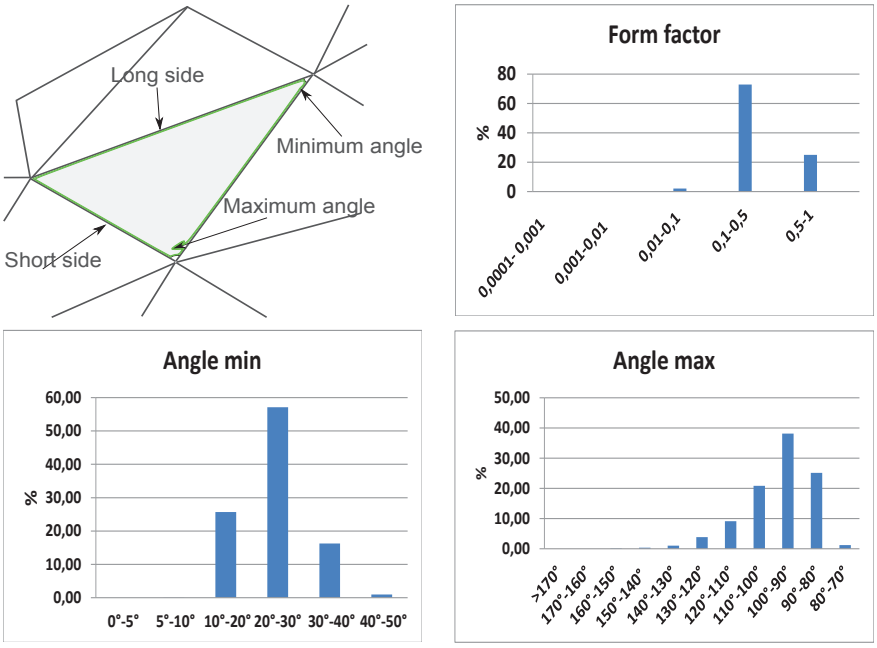

Figure 4.6 – Some criteria of mesh quality of tetrahedral elements of the human diaphragm without thorax. The triangular mesh element showing the longest side, shortest side, maximum interior angle and the minimum interior angle.

4.3.2 Mesh quality and mesh convergence study

As described in the previous chapter, a mesh convergence study has been done to choose the optimum mesh number from the computational accuracy. The patient (P1) have been selected for the investigation. Stress Von Mises have computed for different resolution of meshing. In order to get better result in different analysis with ABAQUS software, mesh convergence study was done for the patient 1.

Fig.4.5 shows by increasing the number of tetrahedral, the Stress Von mises goes up sharply and then approximately remains steady. As it is shown in the Fig. 4.5, the mesh with 21000 linear tetrahedral elements is a proper point. However, to the need for accuracy, there is also a need for practical considerations when implementing a real time biomechanical model into a radiotherapy application. Requires a compromise between the realism of biomechanical models used the accuracy and computational speed. The computation time increases from 39 seconds to 176 seconds and the small stress Von Mises difference (from 1.655 MPa to 1.71 MPa). In this order, we have selected the mesh with small number elements 5636 for mesh quality study.

In our study, the mesh quality is performed using Abaqus packages. The FE model consisting of only human lung included as example 5636 linear tetrahedral elements, out of $97,83\%$ of the elements with shape factor $(\frac{EV}{OEV})$ [1] between 0.1 and 1, $82,95\%$ elements

1. EV: element volume and OEV: Optimal element volume is the volume of an equilateral tetrahedron with the same circumradius as the element. (The circumradius is the radius of the sphere passing through

with minimum angle$\geq$ 20, 99,5% elements with maximum angle $\leq$ 140, 95,9% elements with minimum length edge $\geq 3mm$, 99,1% elements with maximum length edge $\leq 15mm$, thus meeting the desired element quality (Fig.4.6).

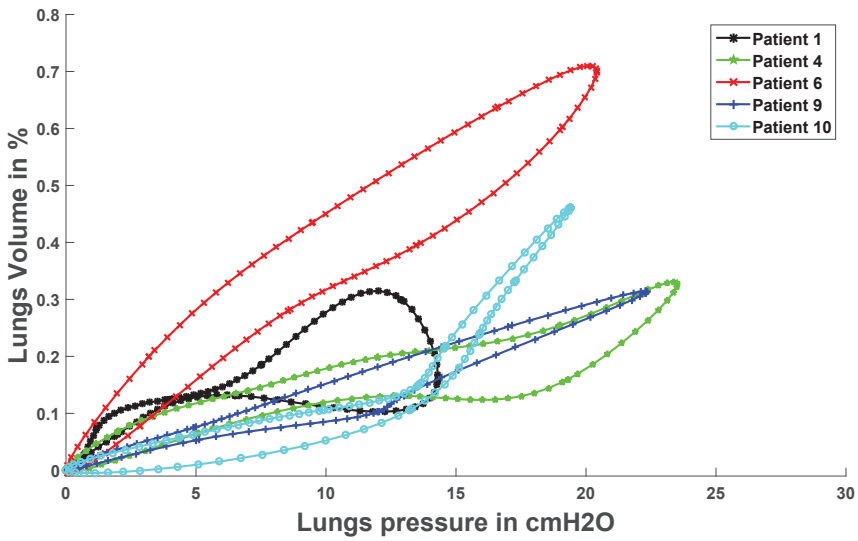

Figure 4.7 – Different specific compliances for each patient, calculated and identified at each state directly from 4D CT scan images

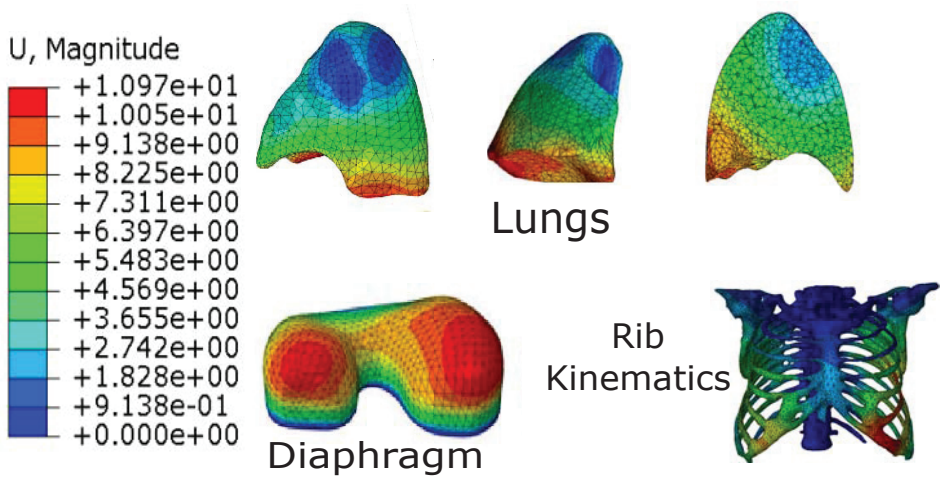

Figure 4.8 – Qualitative analysis of finite element simulation for respiratory system

4.3.3 Qualitative and quantitative comparison

In order to demonstrate the validity of our patient specific biomechanical model, a quantitative and qualitative analysis of simulations were conducted. We have compared

the four vertices of the tetrahedron.)

Table 4.1 – Mechanical properties of breathing system: LE Linear Elastic, HVSK Hyperelastic Saint Venant Kirchhoff, E Youngs modulus andν Poisson coefficient (from [Al-Mayah 2011, Villard 2005], ρ volumetric density (calculated from CT images) .

Tissues	Mechanical behavior	E (MPa)	ν	ρ (t/mm^3)
Lungs	HSVK	$3.74\,10^{-3}$	0.3	$3\,10^{-10}$
Lung tumor	LE	49	0.4	1.510^{-9}
Mediastinum	LE	$5.87\,10^{-3}$	0.4	$1\,10^{-10}$
Diaphragm muscle	HSVK	5.32	0.33	$1\,10^{-9}$
Diaphragm tendon	LE	33	0.33	$1\,10^{-9}$
Ribs	LE	5000	0.4	$1.5\,10^{-9}$
Cartilage	LE	49	0.3	$1\,10^{-9}$
Body of sternum	LE	11500	0.3	$1.5\,10^{-9}$
Thoracic vertebra	LE	9860	0.4	$1.5\,10^{-9}$
Flesh	LE	5.32	0.4	$1\,10^{-6}$

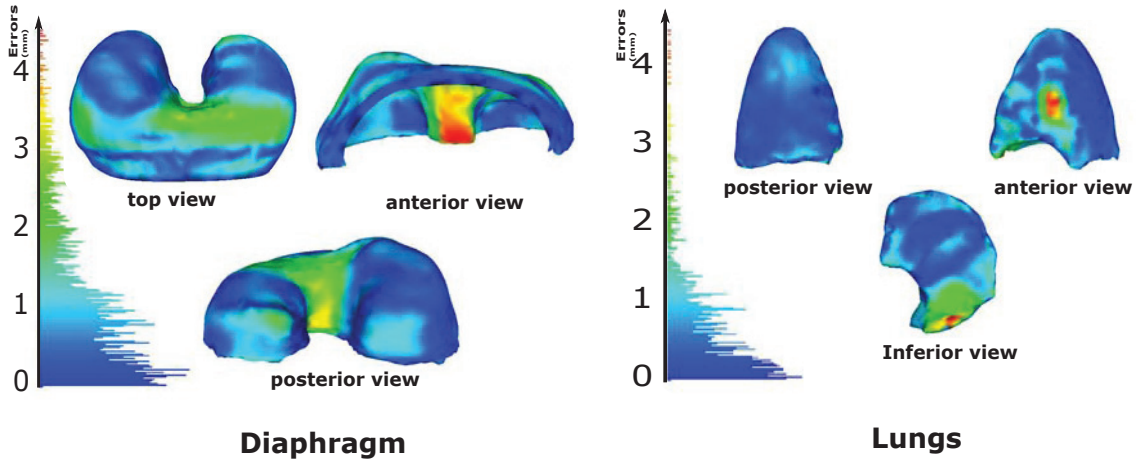

Figure 4.9 – Distance error measurement on the diaphragm and lungs between FEM simulated end inspiration EI and segmented EI extracted from CT images.

the results of a simulated motion with the experimental data provided directly from the 4DCT scan images. In our simulation, the physiological compliance (pressure-volume curve) is patient specific. The Fig .4.7 illustrates the different specific compliances for each patient, calculated and identified at each state directly from 4D CT scan images. Then, these compliances are used as input in our biomechanical patient specific model to simulate the full cycle. In our FE simulation, we define the simulation time for the inspiration phase is 2 seconds and for the expiration phase is 3 seconds. The mechanical properties and behaviors of the different organs used in our simulations are settled in the Table. 4.1.
The Fig.4.8 shows the total deformation and the maximum displacement components of

the lungs and diaphragm during breathing. We can observe the maximum displacement of the diaphragm on the right-posterior (RP) and left-posterior (LP) sides. It is also possible to notice a slightly larger (RP) side motion than (LP) side motion, in concordance with the physiological anatomy. For the lungs deformation, the results resemble the real 4DCT lung deformation with the maximum displacement occurring in the posterior region along the superior-inferior (SI) direction.

surface errors End Inspiration EI	Diaphragm Mean ± SD	lungs Mean ± SD
Patient 1	1.8± 1.5	2.0± 1.5
Patient 4	2,0 ± 1,6	2,2 ± 1,7
Patient 6	1,9 ± 1,6	2.1 ± 1,5
Patient 9	2,1 ± 1,5	2,3 ± 1,6
Patient 10	2,2 ± 1,1	2,5 ± 1,8

Table 4.2 – Average surface errors (mm) for the diaphragm and lungs surfaces at end inspiration EI between FEM simulation surface and segmented surfaces extracted from CT images for four patients from DirLab database [Castillo 2009]

Table.4.2 and Fig.4.2 show the 3D Hausdorff distance surface errors between the simulated finite element surface (diaphragm and lungs) and the segmented surface at end inspiration (EI). The average surface errors are less than 2 mm. The finite element simulation applied on 5 patients shows that the developed model is in a good agreement with the experimental data (medical images). However, errors depend mainly on the quality of the 3D segmentation.

4.3.4 Anatomical landmarks evaluation at end of inhalation (EI) and the end of exhalation (EE)

Then, to measure the precision of our biomechanical simulation, we did a comparison study between the anatomical landmarks of the respiratory system at the end of inhalation (EI) and at the end of exhalation (EE) obtained from CT scan images and our finite element simulations. For each patient, 300 corresponding landmarks at the EI and the EE states are available with manual delineations.
Table.4.3.4 shows the comparative study between our FE simulation results and the anatomical landmarks displacement vectors for five patients. The average for anatomical landmark lung error(mm) at end inspiration (EI) and end expiration (EE) states for four patients are less than $2.5 \pm 1.5mm$ at EI (T00) and at EE (T50) states was obtained. In addition to the need for accuracy, we also evaluated the percentile errors distribution and calculated on the 300 corresponding landmarks for the same lung cancer patients (five patients) along the AP (Anterior/Posterior), RL (Right/Left), and SI (Superior/Inferior) directions. Fig.4.10 and Fig.4.11 summarize the error distribution for 300 anatomical landmarks, the mean error ±

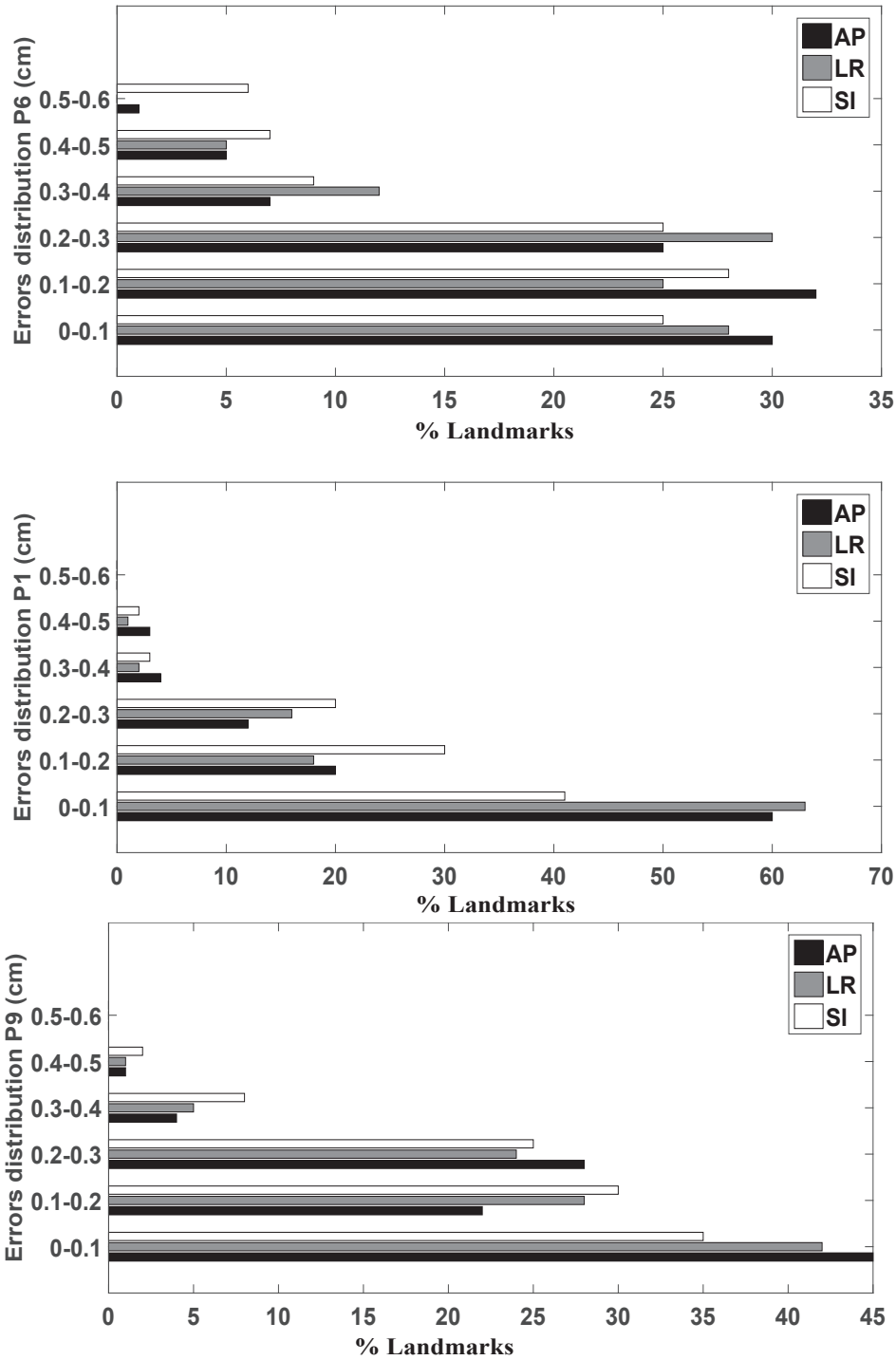

Figure 4.10 – The percentile errors distribution for patient from DIRlab dataset in the AP, RL, and SI directions at EE and EI phases.

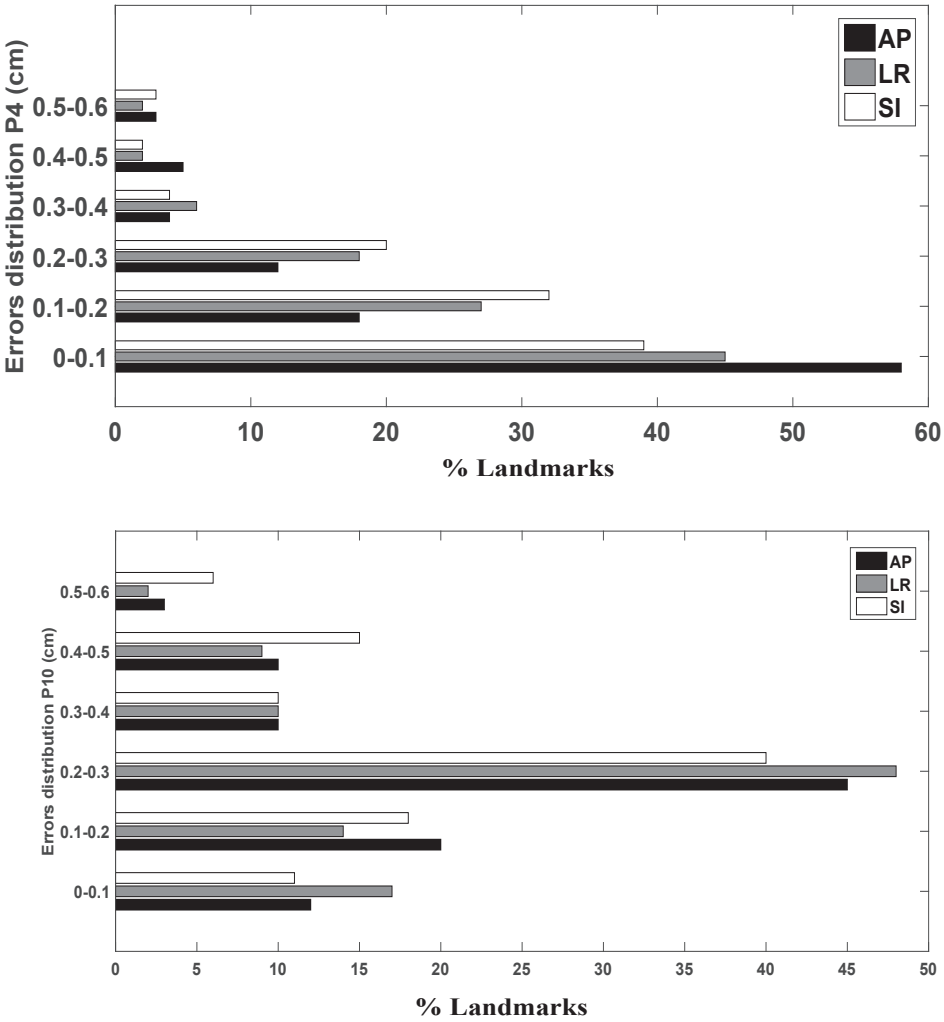

Figure 4.11 – The percentile errors distribution for patient from DIRlab dataset in the AP, RL, and SI directions at EE and EI phases.

the standard deviation in the LR, AP and SI directions at EE and EI phases. More than 95 percentile shows a mean error value less than $3mm$ difference.

4.3.5 Anatomical landmarks evaluation at intermediate states between EI and EE

The performance of the proposed biomechanical model has been evaluated by comparing the simulation results with ground truth (CT images) on 75 landmarks available only between one trajectory from EI to EE at intermediate states (5 states).
The Table.4.3.5.1 shows the comparative study between our FE simulation results and the ground-truth displacement vectors for five patients. In our simulation, we have obtained an average mean error for all ground-truth landmarks: 1.8 ± 1.3, 2.0 ± 1.2, 2.0 ± 1.3,

Mean error ± SD en mm	End Inspiration EI :$T00$	End Expiration EE : $T50$
Patient 1	2,0 ± 1,3	1.5 ± 0.9
Patient 4	2,2 ± 1,5	1.8 ± 1.0
Patient 6	2,0 ± 1,5	2,0 ± 1,2
Patient 9	2,2 ± 1,3	1.9 ± 1,1
Patient 10	2,4 ± 1,6	2.1 ± 1,2

Table 4.3 – Average anatomical landmark lung error(mm) at end inspiration (EI) and end expiration (EE) states for four patients from DirLab database [Castillo 2009]

Patient	Mean ± SD (mm)					Mean
	T10	T20	T30	T40	T50	All states
Patient 1	2,1 ± 1,5	2,2 ± 1,2	2,1 ± 1,6	1,6 ± 1,4	1,1 ± 0,8	1,8± 1,3
Patient 4	2,3 ± 1,2	2,5 ± 1,3	2,1 ± 1,2	1,8 ± 1,2	1,5 ± 1,2	2.0±1.2
Patient 6	2.4 ± 1.5	2.3 ± 1.2	2,0 ± 1.6	1.9 ± 1.6	1.4 ± 1,1	2.0±1.3
Patient 9	2,3 ± 1,4	2,2 ± 1,1	2,1 ± 1,3	1,8 ± 1,4	1,3 ± 0,9	1.9± 1.2
Patient 10	2,1 ± 1,5	2,2 ± 1,2	2,1 ± 1,6	1.6 ± 1,5	1.1 ± 0.8	1.8±1.3

Table 4.4 – Average landmark lung error (mm) during respiration at different respiratory states: the first state T00, the end inspiration (T50), the end expiration (T10)

1.9 ± 1.2 and 1.8 ± 1.3 (mm) respectively for P1, P4, P6, P9 and P10 respectively. These results show that the developed biomechanical model coupled with the personalized lung-pressure/diaphragm-force optimization algorithm of the respiratory system is in a good agreement with the experimental data, and produces more accurate predictions with lower errors than other works ([Fuerst 2015] ,[Li 2015]) applied to the same data sets and despite using less parameters.

4.3.5.1 Tumor tracking and impact of the rib kinematics on lung tumor motion

In order to evaluate the impact of the rib kinematics on lung tumor motion, we have compared the 3D lung tumor trajectories identified and estimated from CT scan images with the trajectories estimated by finite element simulation. However, the tumor trajectory has been evaluated on a full breathing cycle (10 phases between the EI and EE). Firstly, to overcome the segmentation difficulties of lung tumor and geometric uncertainties, the affine registration (rigid translation and rotation) method is applied to the lung tumor mesh (with good quality surface reconstruction) at different respiratory states. Then, the accuracy is evaluated on two patients (patient 6 with the tumor location in the left lung, and patient 10 with tumor in the right lung in contact with the diaphragm), by comparing and calculating the average Hausdorff distance between the 3D mesh surface of the segmented tumor and predicted FE lung tumor, including or not the rib kinematics. The Fig. 4.12, Fig.4.13 and Fig.4.14 demonstrate that our patient specific biomechanical model for lung tumor position

estimation is very accurate (less than 3 mm).

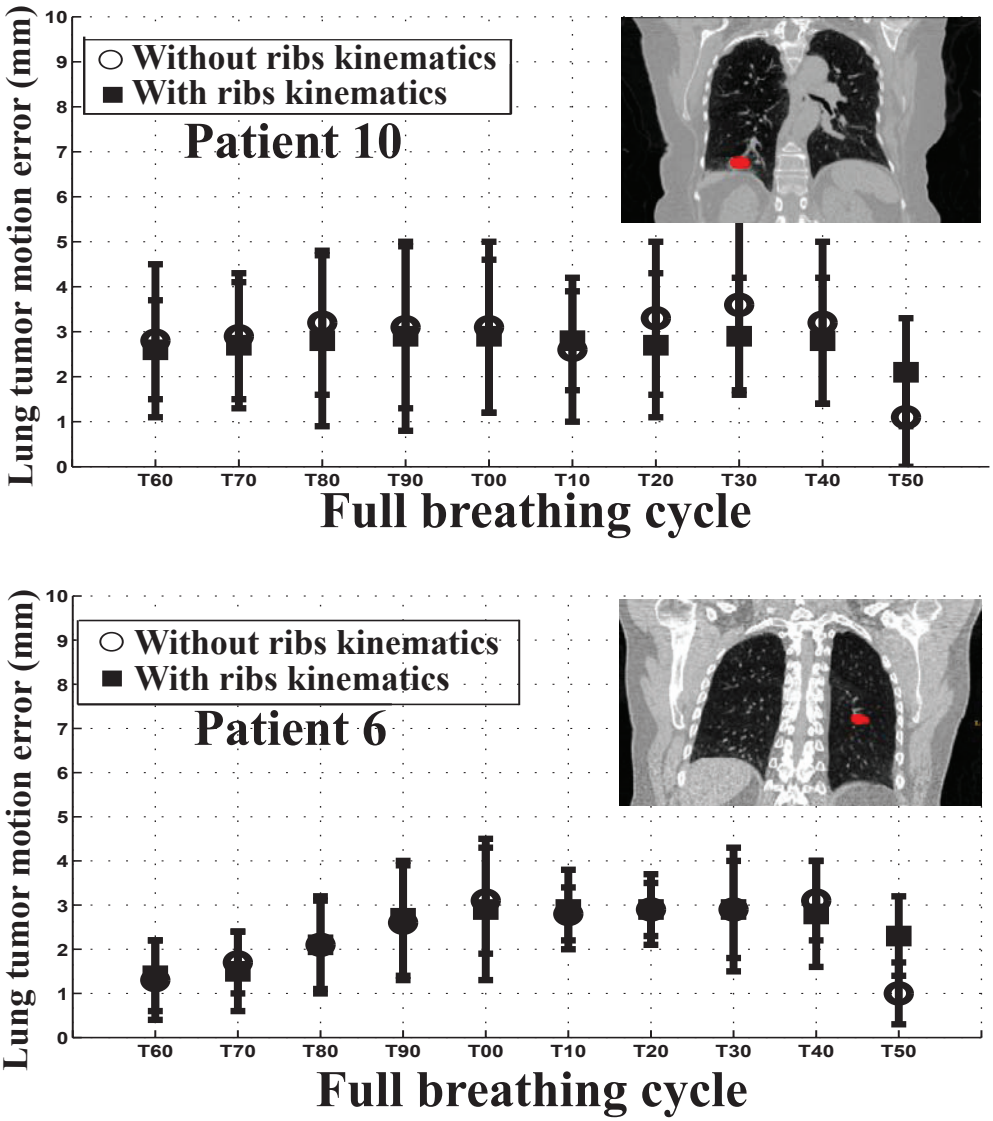

Figure 4.12 – Mean errors ± standard deviation of lung tumor position during the whole cycle of breathing (10 phases between the EI and EE) between the trajectory issued from 4D CT images compared to the trajectory calculated by biomechanical finite element simulation coupled with the lung-pressure/diaphragm-force optimization for two patients P6 and P10.

Another investigation conducted to study the impact of rib kinematics on the lung tumor motion prediction. This investigation was conducted by varying the ribs displacement by 10%, 25% and 50% during the whole breathing cycle. The Fig.4.15 illustrates that our patient specific biomechanical model for lung tumor position estimation is in a good agreement with the experimental data. These analysis confirmed the robustness of the proposed technique for lung tumor motion tracking. It is important to note that the results

References	Cycle	Organs Modeled	Boundary conditions	P6 (mm)	P9 (mm)	P10 (mm)
[Fuerst 2015]	half	All organs No ribs	4 pressure zones (sub diaphragm) 16 pressure zones (thoracic)	3.27 ±1	2.97 ±1	2.83 ±1
[Li 2015]	half	Only lungs	One CT Uniform pressure	- -	3.2±1.4	4.4±2.9
		All organs	Personalized P-V			
Our model [Giroux 2017a]	Full	Thorax	Rib Kinematics	2.0±1.3	1.9± 1.2	1.8±1.3
		Diaphragm	Tangential force			

Table 4.5 – Comparison between our biomechanical patient specific model results and the results from Fuerst et al. [Fuerst 2015] and Li et al. [Li 2015], on patient 6, patient 9 and patient 10 issued from DIR-Lab Dataset [Castillo 2009].

for the patient 6 and patient 10, are slightly better with the rib kinematics but the difference is not significant during the whole cycle for patient 6 and 10. This is because the respiration for these patients is mainly diaphragmatic.

4.3.6 Mechanical parameters uncertainty assessment

Mechanical properties of the lung cancer tissue are specific and differs from one patient to another and depends on geometrical, pathological and physiological characteristics of the patient. To investigate the impact of mechanical properties uncertainties on the lung tumor motion prediction, we have compared and evaluate the most values the lung tissue Young's modulus and Poisson's ratio used in the literature. Hence, it is very important to take these variations in our model and simulations to assess the method's robustness and accuracy. In this part, all simulations applied the St. Venant-Kirchoff material model.

4.3.6.1 Young's modulus

A variety values of the Young's modulus can be found in the literature. The lung tissue Young's modulus is reported at 0.1kPa to 10kPa in different studies [Al-Mayah 2011, Werner 2009, Nakao 2007, Villard 2005]. In our study, we have evaluated and compared the Young's modulus values often used in the literature and applied to simulate lung deformation. We choose four values: $E = 3.74kPa$ from [Al-Mayah 2011], $E = 0.1kPa$ from [Werner 2009], $E = 0.823kPa$ from [Villard 2005] and $E = 10kPa$ from [Nakao 2007], for fixed value of Poisson's ratio ($\nu = 0.33$). Furthermore, we have evaluated the sensitivity of lung motion estimation to variations of the lung tissue mechanical properties, using 75 anatomical landmarks from EI to EE at intermediate states (5 states). For each Young modulus value, we recalculate the personalized physiological compliance (pressure-volume curve).

Fig.4.16 shows the average landmark lung error during respiration at different respiratory

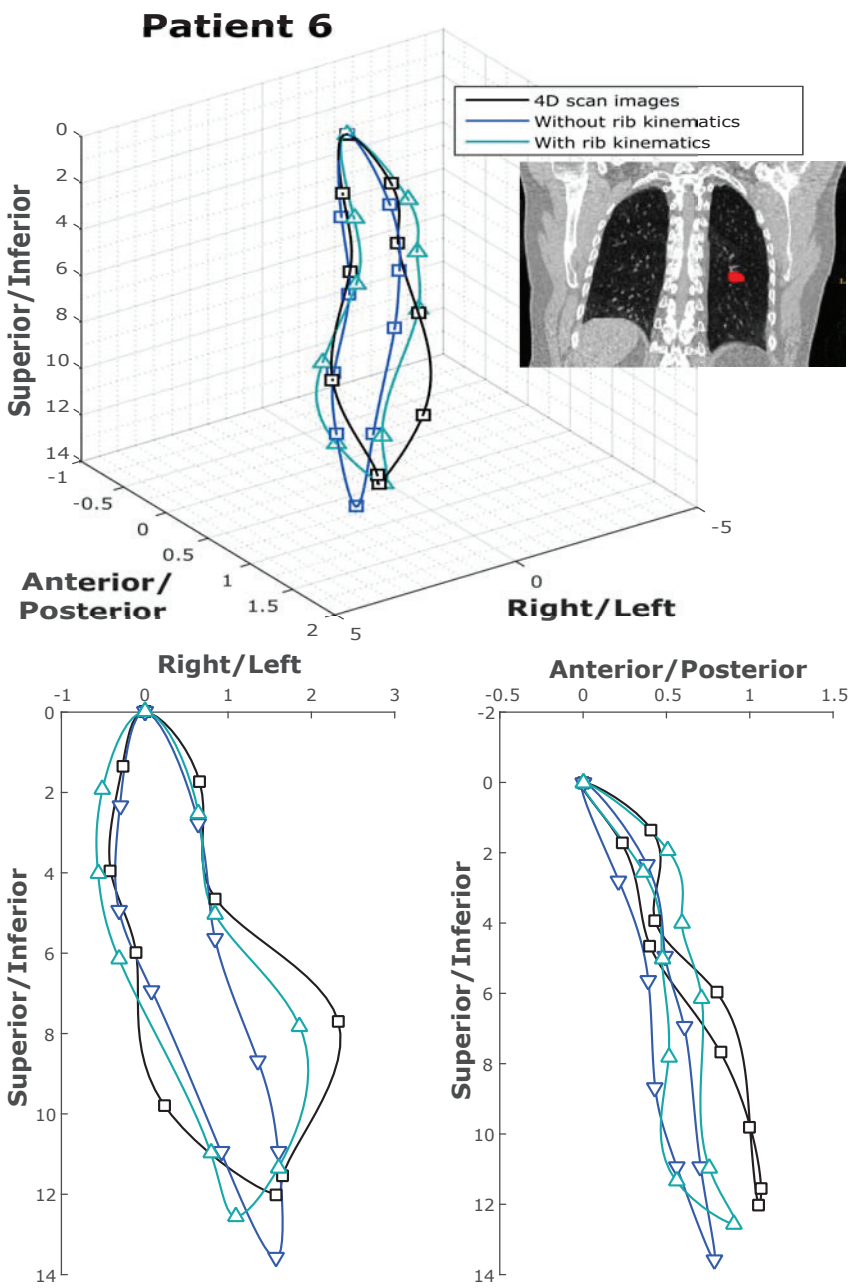

Figure 4.13 – 3D lung tumor trajectory (in mm) issued from 4D CT images compared to the trajectory calculated by biomechanical finite element model including or not the rib kinematics for patients P6 for DirLab data set [Castillo 2009].

states for different value of Young's modulus. This comparison demonstrated a good agreement between the experimental and simulation results for the different value of Young's modulus and the variation is small and negligible.

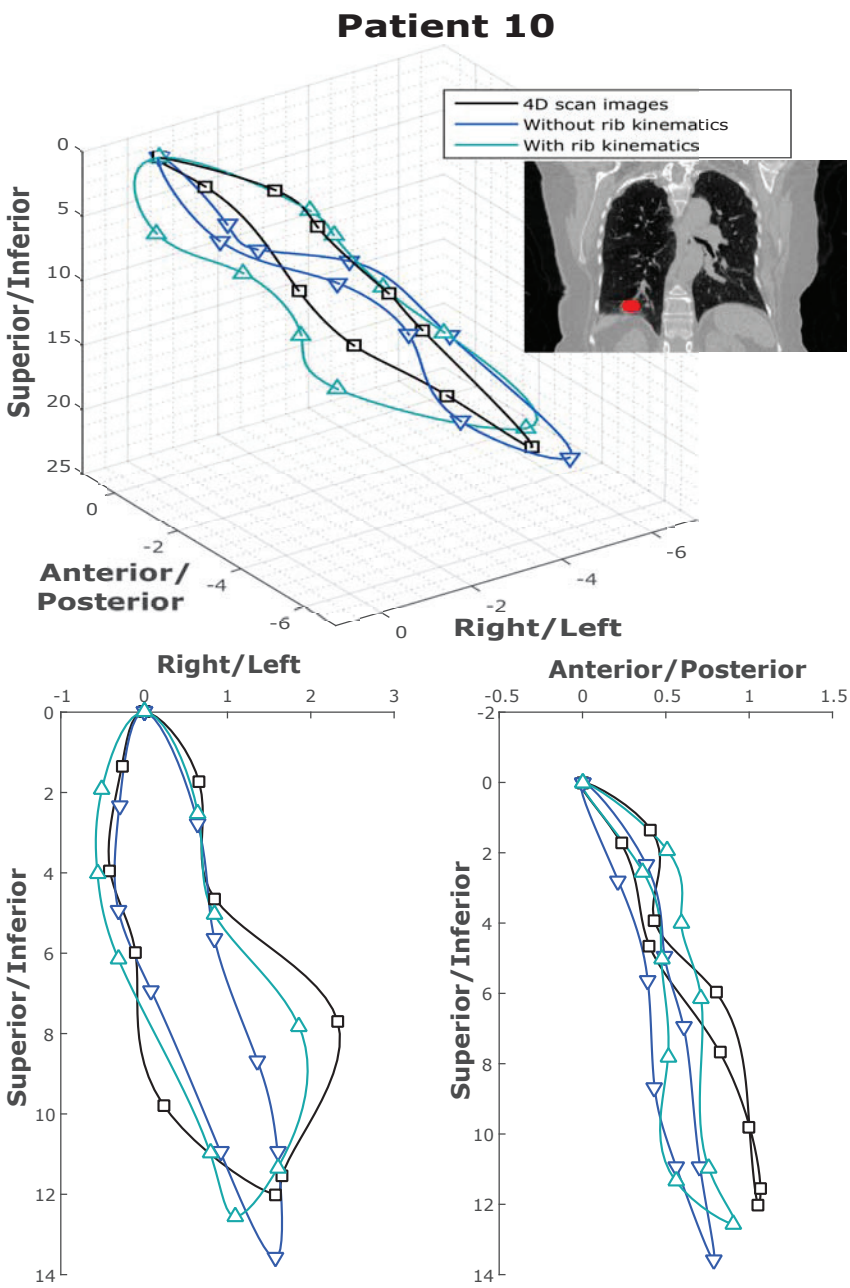

Figure 4.14 – 3D lung tumor trajectory (in mm) issued from 4D CT images compared to the trajectory calculated by biomechanical finite element model including or not the rib kinematics for patients P10 for DirLab data set [Castillo 2009].

4.3.6.2 Poisson's ratio

Therefore a range of values from $\nu = 0.2$ to $\nu = 0.5$ was used in our simulations to investigate the influence and impact of PoissonŠs ratio on landmark lung error during respiration at different respiratory states. For fixed value of Young modulus $E = 3.74kPa$,

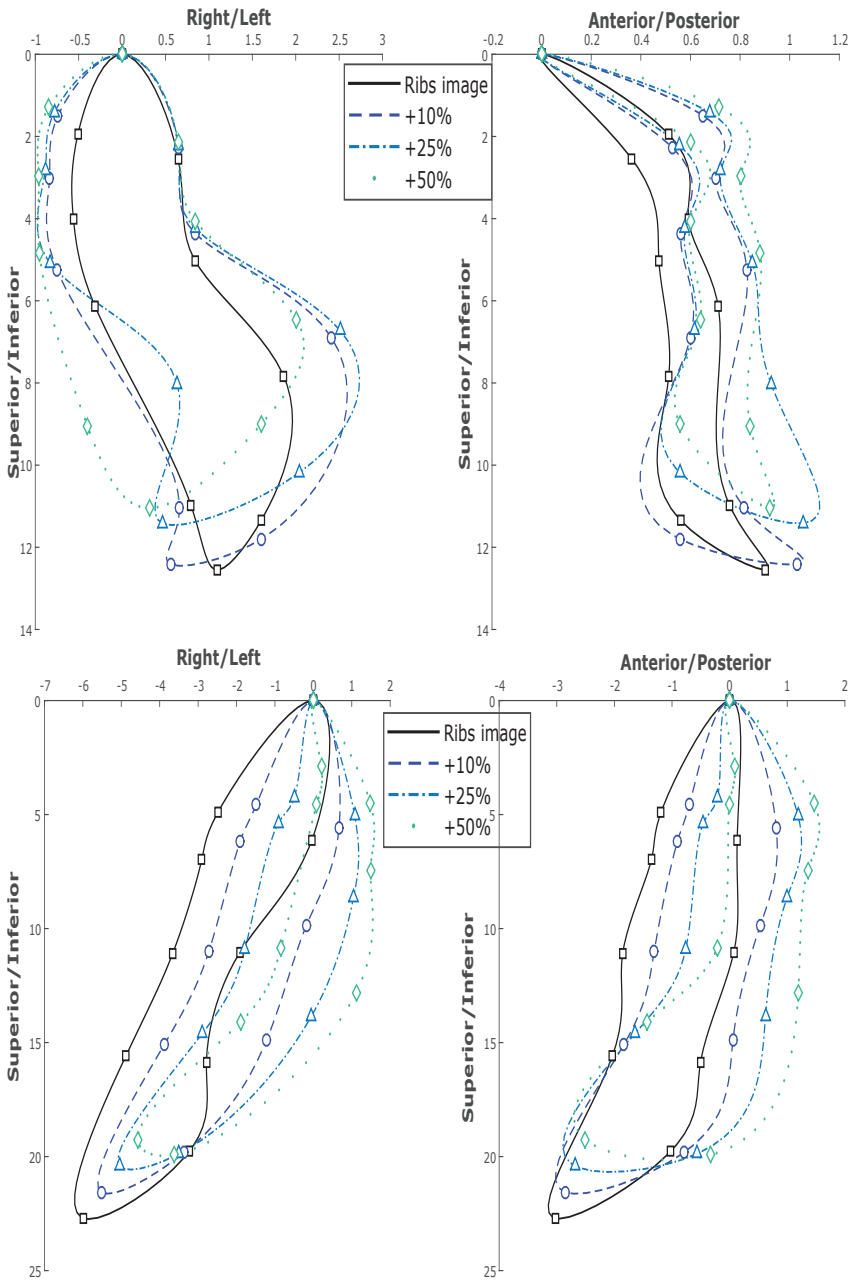

Figure 4.15 – 3D lung tumor trajectory (in mm) issued from 4D CT images compared to the trajectory calculated by biomechanical finite element model including rib kinematics displacement changed by 10%, 25% and 50% of the rib displacement calculated from CT scan images.

a series of simulations with different different values of Poisson ratio were generated. The values chosen were $\nu = 0.33$, $\nu = 0.2$, $\nu = 0.4$ and $\nu = 0.49$. Fig.4.17 shows he average landmark lung error during respiration at different respiratory states for different value of

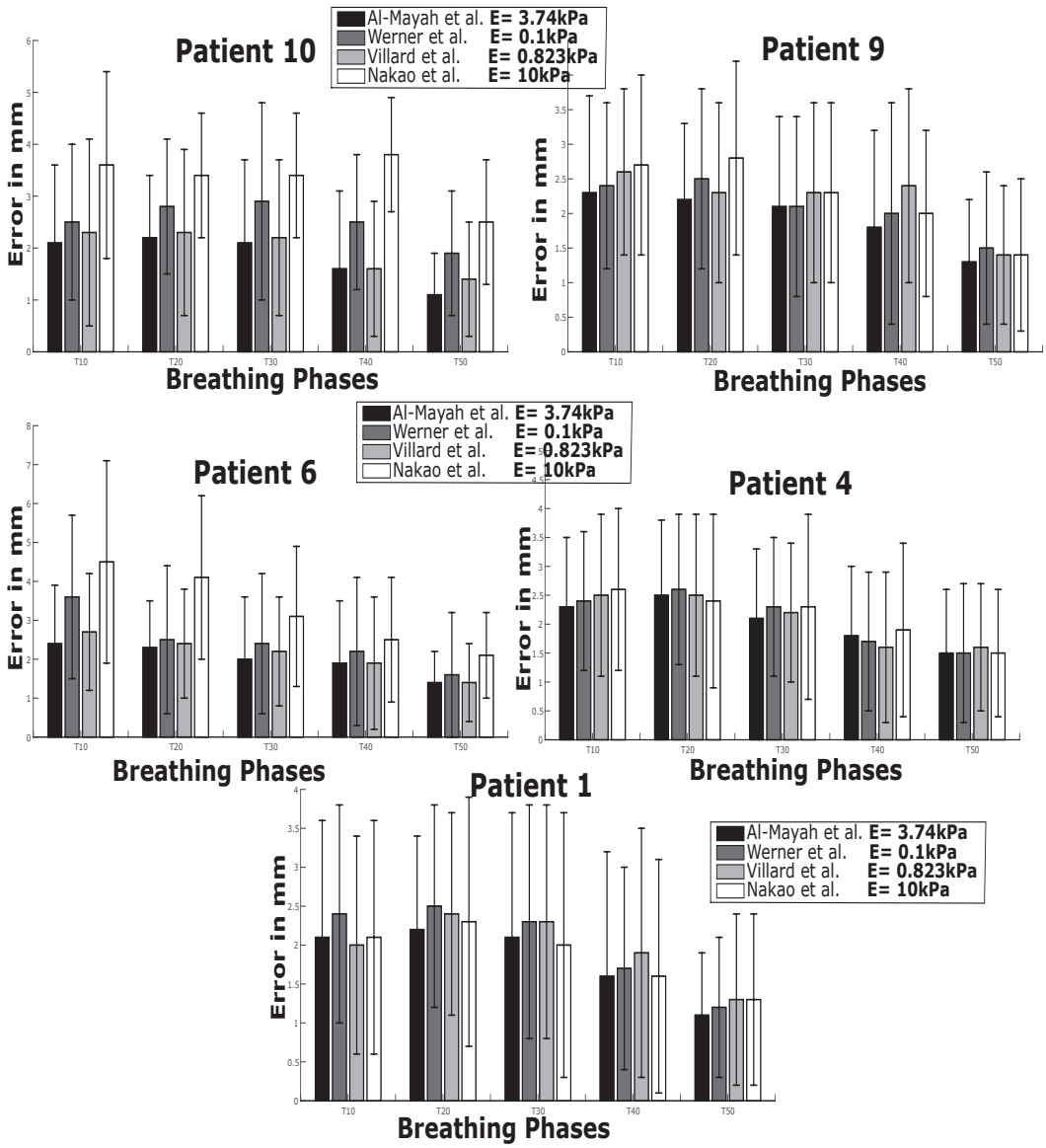

Figure 4.16 – Young's modulus sensibility: Average landmark lung error (mm) during respiration at different respiratory states for different value of Young's modulus

Poisson ratio.

Contrary to Young's modulus variation, the poisson ratio variation has an impact on the simulation result. In these comparisons, the results indicates that the landmark lung error(obtained by $\nu = 0.49$; quasi-incompressible) is three times larger than the landmark lung error obtained from Poisson ratio $\nu = 0.33$.

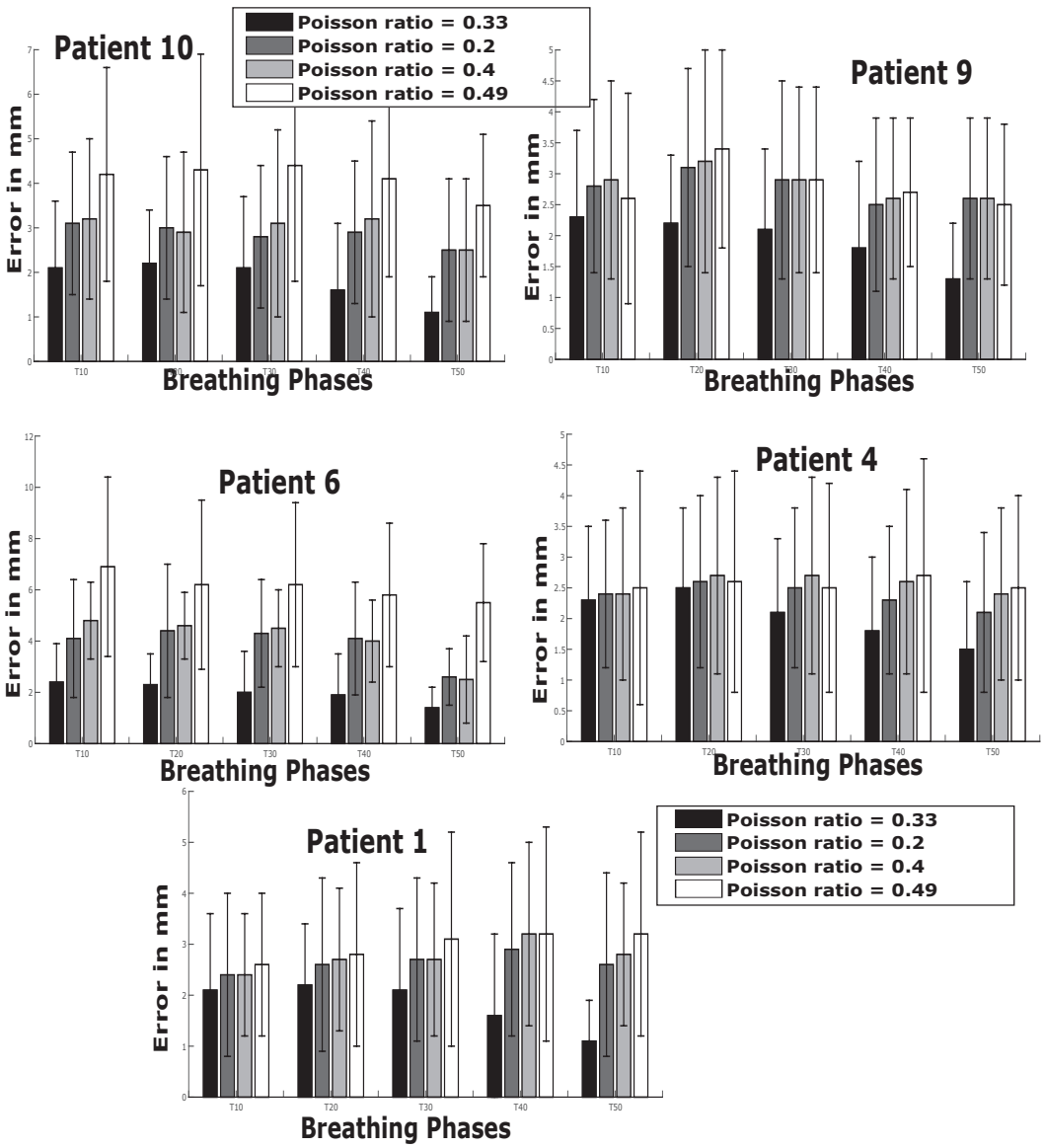

Figure 4.17 – Poisson's ratio sensibility: Average landmark lung error (mm) during respiration at different respiratory states for different value of Poisson's ratio

4.3.7 Behavior uncertainty

Another important effect In the chapter 3, we have illustrated the impact of the nonlinearity type (geometrical or material) to find globally the appropriate mechanical behavior of the organs (diaphragm and lungs), calculated directly from 4D CT images. Until now, the different simulations in this thesis applied the St. Venant-Kirchoff material model for the lung and diaphragm tissues.

The main objective in this section is to simulate the mechanical behavior of the lung tissue. To perform this, a study of four widely referenced hyperelastic models in the literature is

Table 4.6 – Material parameters value for four hyperelastic models for respiratory motion

Models	parameters
Saint-Venant Kirchoff model	$E = 3.74kPa$ and $\nu = 0.33$
Mooney Rivlin model	$C_{10} = 0.703kPa$, $C_{01} = 0.703kPa$ and $D = 3.74\,kPa$
Neo Hooke model	$C_{10} = 0.703kPa$ and $D = 3.74kPa$
Yeoh model	$C_1 = 0.703kPa$, $C_2 = -7.03kPa$ and $C_3 = 703kPa$

performed. Numerical simulations are carried out for Neo-Hookean model, Yeoh model, Mooney-Rivlin model, and St. Venant-Kirchoff model. For all simulations, the personalized physiological compliance (pressure-volume curve) is calculated using $E = 3.74kPa$ and $\nu = 0.33$ for each patient. The mechanical properties (different parameters) of the different models used in our simulations are settled in the Table. 4.6. For more details concerning how to calculate the different parameters of each model can be found in Appendix 1.

Fig.4.18 illustrates the comparison study between the different hyperelastic models on the lung motion estimation. The performance of the proposed biomechanical model has been evaluated by comparing the FE simulation results with ground truth (4D CT images) on 75 anatomical landmarks, at end inspiration (EI) and end expiration (EE) states, and at each respiratory state. From a biomechanical point of view, Saint-Venant Kirchhoff model (linear elastic behavior with large displacement) give as good results as Mooney-Rivlin model (full nonlinear hyperelastic behavior) compared to the Neo Hooke model and Yeoh model. In view of the obtained results, it can be concluded that the Saint-Venant Kirchhoff and Mooney-Rivlin models are the most accurate behavior models for simulate the lung tissues.

4.3.8 Discussion and conclusion

In this chapter, we have evaluated the accuracy of our developed patient specific biomechanical model of the respiratory system for a whole respiratory cycle, based on specific pressure-volume curves, chest movement, as well as an automatic tuning algorithm to determine specific lung pressure and diaphragm force parameters. A quantitative and qualitative analysis of simulations were conducted on five selected patients from DIR-Lab dataset with small and large breathing amplitudes (P1=10.9 mm, P4=18.1 mm, P6=27.2 mm, P9=15.5 mm and P10=26.06mm). The performance of the proposed biomechanical model has been evaluated by comparing the simulation results with ground truth (CT images) on 75 anatomical landmarks available between end inspiration (EI) and end expiration (EE) and intermediate states, also on 300 anatomical landmarks available at end inspiration (EI) and end expiration (EE). However, the tumor trajectory has been evaluated on a full breathing cycle (10 states).
Another investigation conducted in this thesis, the impact of rib kinematics on the lung tumor motion prediction by varying the ribs displacement. Also, we have examined the different elasticity parameters (Young's modulus and Poisson's ratio) on the lung tumor motion. In this order, we have compared and evaluate the most values the lung tissue

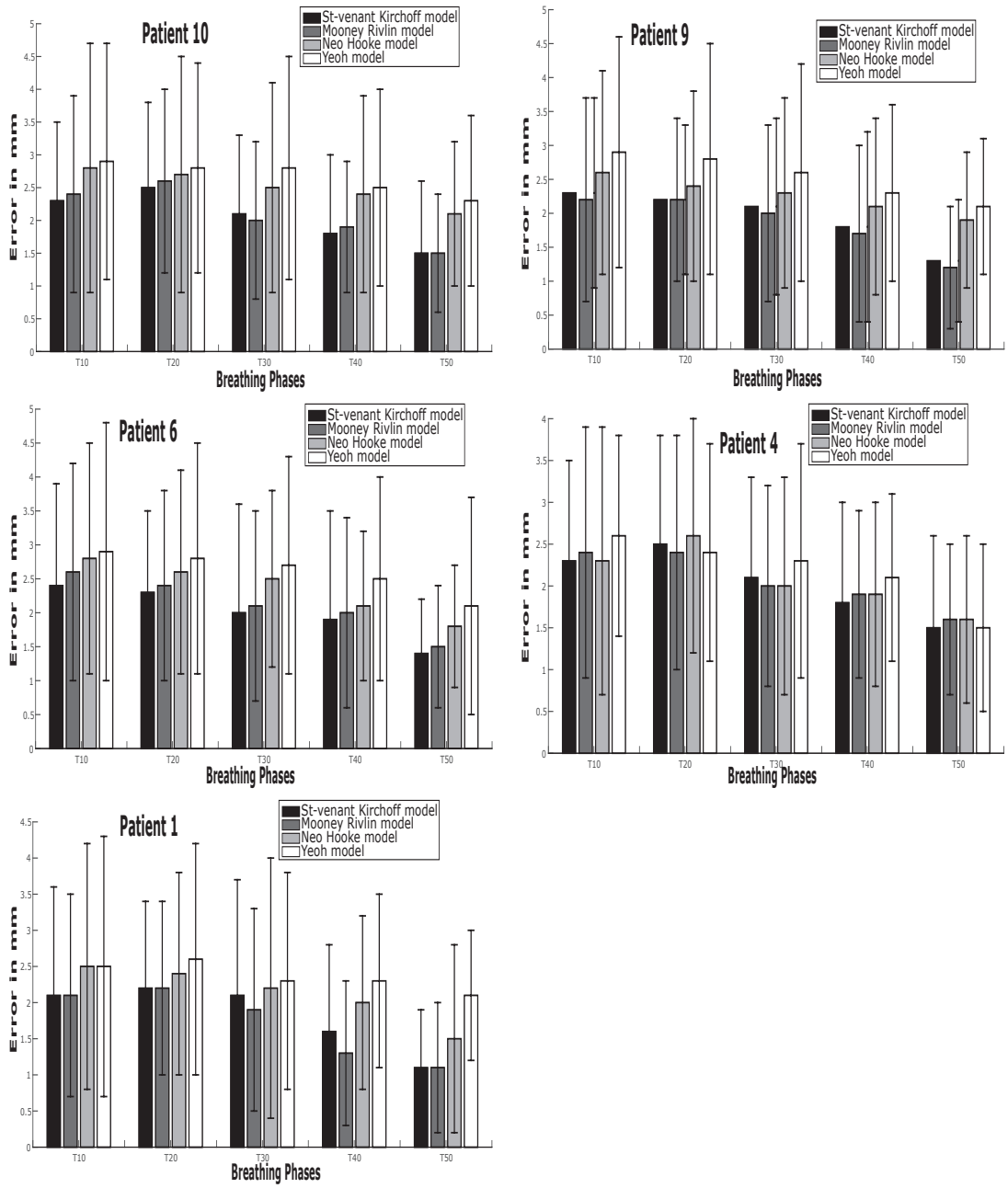

Figure 4.18 – Mean errors ± SD between FE simulation results with ground truth (4D CT images) on 75 anatomical landmarks, at end inspiration (EI) and end expiration (EE) states based on four hyperelastic models: Neo-Hookean model, Yeoh model, Mooney-Rivlin model and St. Venant-Kirchoff model.

Young's modulus and Poisson's ratio used in the literature. The impact of different values for Young's modulus was found to be small. In contrast, Poisson's ratio was observed to be little important. This is probably due to the our adaptive and automatic tuning algorithm

to determine patient specific compliance (pressure-volume curve).
Additionally, we have investigated the impact of the nonlinearity type mechanical behavior of the lung tissue. In this order, four widely referenced hyperelastic models in the literature is performed(Neo-Hookean model, Yeoh model, Mooney-Rivlin model, and St. Venant-Kirchoff model).
In our study, the Saint-Venant Kirchhoff model gives a performance very similar to the full non linear Mooney-Rivlin model. Our results are quite realistic compared to the 4DCT scan images. We can observe that the proposed physically-based FE model is able to predict correctly the respiratory motion.

Chapter 5

General conclusions and future perspectives

The 4D computational patient specific of the respiratory system could be potentially used in various medical contexts; for diagnosis, treatment planning, laparoscopic, dose computation or the registration between online imaging systems such as positron emission tomography (PET), computed-tomography (CT) as well as high fidelity and precise computer-based training simulators.
In this PhD project we have investigated the challenging issues in patient-specific biomechanical model of the respiratory system enabling the correlation of the internal organs motion with respiratory surrogate signal(s) during the treatment. This permits to take into account the respiratory motion variabilities. The deformation of the different structures is controlled and driven by simulated rib cage (mimic the external intercostal muscles) and diaphragm actions. For the diaphragm, we have applied the radial direction of muscle forces, and simple homogeneous dirichlet boundary condition is applied to the lower part of the diaphragm, which is attached to the rib cage. For each rib a rigid transformation is calculated automatically by finite helical axis method (rigid translation and rotation) and used to define displacement boundary conditions. The resulting widening of the thoracic cavity forces the lungs to expand due to an applied negative pressure in the pleural cavity. Other novelty of this thesis, that the amplitude of the lung pressure and diaphragm force are patient-specific, and determined at different respiratory states by an optimization framework based on inverse FE analysis methodology, by minimizing the volume lungs errors, between the respiratory volume (calculated from CT scan images at each state) and the simulated volume (calculated by biomechanical simulation). All other structures are linked to each other, but feature different deformation behavior due to the assigned material properties. Five selected patients from DIR-Lab dataset with small and large breathing amplitudes, and two with visible lung tumor, from DIR-Lab Dataset [Castillo 2009] have been considered. We have compared the FE simulation results on 75 and 300 anatomical landmarks, at end inspiration (EI), end expiration (EE) states, and at each intermediate respiratory state. We have also evaluated the tumor motion identified in 4D CT scan images and compared it with the trajectory obtained by FE simulation, during one complete

breathing cycle. The results demonstrate the good quantitative results of our physic-based model.

Another investigation conducted in this thesis, we have study the impact of rib kinematics on the lung tumor motion prediction by varying the ribs displacement. Also, we have examined the different elasticity parameters (Young's modulus and Poisson's ratio) on the lung tumor motion. In this order, we have compared and evaluate the most values the lung tissue Young's modulus and Poisson's ratio used in the literature. The impact of different values for Young's modulus was found to be small. In contrast, Poisson's ratio was observed to be little important. This is probably due to the our adaptive and automatic tuning algorithm to determine patient specific compliance (pressure-volume curve).

Also, we have investigated the impact of the nonlinearity type mechanical behavior of the lung tissue. Four widely referenced hyperelastic models in the literature is performed(Neo-Hookean model, Yeoh model, Mooney-Rivlin model, and St. Venant-Kirchoff model). In our study, the Saint-Venant Kirchhoff model gives a performance very similar to the full non linear Mooney-Rivlin model. Our results are quite realistic compared to the 4DCT scan images. We can observe that the proposed physically-based FE model is able to predict correctly the respiratory motion. The general conclusions of the dissertation and future work are provided in the next chapter.

Our current Biomechanical model provides a powerful tool to simulate respiratory mechanics, however, the generation of these models is very time-consuming, requiring laborious steps for diaphragm segmentation, surface modeling and treatment of the multiple-organ meshing. Therefore, this requires a large amount of manual operation time for one patient. To avoid these limitations and reduce the manual operation time without lowering the quality, a realistic atlas based 3D shape reconstruction based on statistical training might be used to get fast and automatic 3D shape registration patient-specific model. These methods establish correspondences across different subjects and generate high-quality surface meshes without removing shape details, taking into account complexities such as geometrical irregularity and organ contacts within patient-specific anatomical boundary conditions. Our current model, although accurate, cannot be directly used in clinical situations. It is therefore important to optimize the algorithms for real time clinical validation. In this order, a large part of this project is to develop and evaluate new improved real time 4D personalized dynamic patient-specific of the respiratory system monitored by the external modalities. This model will be validated pre-clinically based on dynamic anthropomorphic breathing phantom, LuCa (Lung Cancer) developed by the Center for Proton Therapy at the Paul Scherrer Institute (PSI) Fig.5.1. The different experimentation will be done at center of Protontherapy "Antoine Lacassagne" (CAL) in Nice and hospital George Pompidou .

To conclude, the approaches presented in this manuscript (patient-specific biomechanical model of the respiratory system) can be used to improve the 4D treatment planning in the

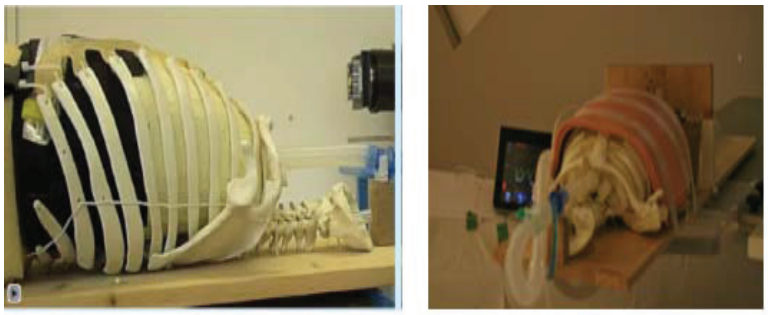

Figure 5.1 – Dynamic anthropomorphic breathing phantom, LuCa (Lung Cancer) developed by the Center for Proton Therapy at the Paul Scherrer Institute (PSI)

context of beam tracking as it could take into account all the possible variations of the breathing pattern before treatment. Moreover, this model could be investigate the effects of different breathing patterns on PET-based treatment verification. In the same context of treatment verification, together with a biomechanical model based on tetrahedral mesh, can be used in order to simulate Prompt Gamma events and to estimate the effects of motion-induced breathing on Prompt Gamma imaging. In the same manner, the same approach can be extended in the future to other types of imaging such as proton radiography or vertex imaging.

Chapitre 6

Résumé en français

6.1 Introduction

La Radio/Hadron-thérapie consiste à déposer une dose létale de rayonnement dans la tumeur tout en réduisant l'impact de cette dose sur les tissus sains. Les mouvements internes, en particulier ceux engendrés par la respiration modifient la forme, la position et la densité des organes, source d'erreur et d'incertitude sur la position du dépôt de dose. Lorsque la tumeur se trouve sur un organe en mouvement, la difficulté majeure est de cibler la tumeur pendant le traitement. Cette incertitude sur la position rend indispensable la mise en place d'une stratégie permettant la prédiction du mouvement tumoral. Ceci permet en effet de guider le faisceau de rayons ionisants de sorte qu'il suive les mouvements tumoraux. De plus, le traitement par hadronthérapie nécessite également l'accès à une description précise de la densité de l'ensemble des organes traversés par le faisceau, car la position du dépôt maximal de l'énergie véhiculée par les ions (le pic de Bragg) en dépend. Malheureusement, le mouvement respiratoire est complexe et sa prédiction n'est pas une tâche simple Ű en particulier, la respiration est commandée par l'action indépendante des muscles de la cage thoracique et du diaphragme.
Les techniques actuelles basées sur l'imagerie, telles que le Cone-Beam ou le recalage déformable d'images, tentent de prédire la position des tumeurs pulmonaires. Ces méthodes font l'hypothèse d'un mouvement reproductible de l'appareil respiratoire dans le temps. D'autres techniques basées sur l'emploi de deux caméras à rayons X (cyberknife, tracking mis au point par l'équipe du Centre carbone d'Heildelberg [HIT]) peuvent permettre la prédiction de la position des tumeurs, quand leur segmentation et leur contourage automatique en temps réel est possible. Cependant, ces méthodes sont, si ce n'est risquées, invasives, et elles ne permettent pas de calculer l'évolution des organes environnants, une information indispensable pour déterminer la position du pic de Bragg. Ainsi déduire le mouvement de la tumeur à partir de seules séries d'images médicales apparaît comme insuffisant. Une solution peut alors résider dans le développement d'un modèle biomécanique patient-spécifique du système respiratoire intégrant la variabilité du mouvement respiratoire. Pour que ce modèle soit précis, il doit comprendre la modélisation de la cage thoracique, du diaphragme et des poumons. Il est tout aussi important que ce modèle puisse être piloté par des pa-

ramètres mesurés en externe (capteurs 3D, spiromètre, etc.) afin de préserver un caractère non-invasif et de corréler le mouvement externe du thorax et de l'abdomen, ainsi que le flux d'air échangé avec les mouvements internes. Les changements de propriétés mécaniques des milieux traversés par le faisceau doivent également être modélisés afin de satisfaire les besoins de l'hadronthérapie.

6.2 Contributions

L'objectif global de mon projet de thèse est d'améliorer le traitement par thérapie ionisante du cancer pulmonaire. Le principe de cette thérapie consiste à déposer une dose létale de rayonnement dans la tumeur tout en réduisant l'impact de cette dose sur les tissus sains. Lorsque la tumeur se trouve sur un organe en mouvement, la difficulté majeure est de cibler la tumeur pendant le traitement. Ce facteur limitant est particulièrement marqué dans le cas des tumeurs pulmonaires pour lesquelles les résultats cliniques sont encore insatisfaisants.
Mon projet de thèse consiste à l'amélioration et la personnalisation d'un modèle biomécanique 4D (3D+t) de l'appareil respiratoire développé au sein de l'équipe, et de prendre en compte la variabilité morphologique dans la modélisation géométrique, ce qui nécessite la personnalisation géométrique et mécanique des modèles pour chaque patient, et la prise prendre en compte la variabilité intra individus. Il est tout aussi important que ce modèle puisse être piloté et contrôlé par des différentes modalités de capture externe (capteurs 3D, spiromètre, etcĚ) et préserver un caractère non-invasif.
Durant ma thèse, nous avons développé une nouvelle approche basée sur un modèle biomécanique patient spécifique du système respiratoire. L'approche proposée est originale, car contrairement aux modèles classiques qui ne prennent pas en compte les paramètres physiologiques et la variabilité respiratoire, l'approche développée permet de calculer des paramètres patient-spécifique à partir des images scanner 4D du même patient. Le modèle biomécanique est contrôlé par une compliance physiologique personnalisée (courbes pression-volume pulmonaire). Pour déterminer ces paramètres patient-spécifique à chaque état respiratoire, nous avons développé une approche automatique basée sur une analyse par éléments finis inverse en minimisant les variations des volumes pulmonaires entre les données expérimentales issues directement des images scanner CT 4D et les résultats de simulation.
Nous avons évalué la précision de notre approche sur cinq (5) patients sélectionnés à partir de données disponibles dans la littérature DIR-Lab [Castillo 2009], avec des amplitudes respiratoires petites et grandes, en comparant les résultats de simulation éléments finis sur 300 et 75 points ou repères anatomiques, à la fin de l'inspiration, fin de l'expiration, et à chaque état respiratoire intermédiaire. Les mouvements et les trajectoires en 3D de la tumeur ont été évalués en comparant les trajectoires calculées à partir des images scanner 4D et les trajectoires prédites et celles issues de la simulation biomécanique.

6.3 Conclusion

Dans cette thèse, Nous avons présenté une approche basée sur une modélisation biomécanique patient-spécifique du systéme respiratoire en incluant le comportement mécaniques approprié à chaque organe. Les résultats du modèle simulé sur 5 patients (5 scanners CTscan 4D) montrent une bonne adéquation avec les données expérimentales. Ces études nous permettent par la suite de développer un prototype pré-thérapeutique de planification et de validation de dosimétrie basé sur une modélisation biophysique personnalisée du système respiratoire. C'est-à-dire un outil de planification et de validation de dose, avant, intra et inter séances de traitement.

Appendix A

Hyperelastic models

Models of hyperelastic materials are regularly used to represent a large deformation behavior of materials. They are commonly used to model the mechanical behavior of elastomers. In addition to elastomers, models of hyperelastic materials are also used to reproduce the mechanical behavior of biological tissues that undergo large deformations. Linear elastic materials are described through two material constants (such as Young's modulus and Poisson ratio). In contrast, hyperelastic materials are described, in most cases, in a deformation energy density function. The stress energy density can be used to derive a nonlinear constitutive model (i.e., stresses as a function of large deformation deformation measures, such as a deformation gradient or Cauchy-Green tensors). , etc.). There are several models proposed in the literature such as Neo-Hookean, Mooney-Rivlin, Ogden, Yeoh models.

Hyperelastic materials can be defined by a stress-strain relationship that is determined by a function of the deformation energy density$W$ such as $\Sigma(E) = \frac{\partial W}{\partial E}$ where$W$ which is in function at the three main deformation ratios (according to the direction) λ_1,λ_2 and λ_3. These three ratios form the invariants (independent of the directions), according to the tensor of the stress of which the characteristic equations are the following ones:

$$I_1 = \sigma_{ii} = \sigma_{xx} + \sigma_{yy} + \sigma_{zz}$$

$$I_2 = \frac{1}{2}(\sigma_{ii}\sigma_{jj} - \sigma_{ij}\sigma_{ij})$$

$$I_3 = J = det(\sigma_{ij})$$

For models of hyperelastic materials are expressed in the form:

$$W = \sum_{i+j=1}^{N} C_{ij}(I_1 - 3)^i (I_2 - 3)^j + \sum_{k=1}^{N} \frac{1}{D_k}(J-1)^{2k}$$

The Saint-Venant-Kirchhoff model is probably the most common hyperelastic model. It holds isotropic materials and has a linear stress-strain relationship:

$$W(E) = \frac{\lambda}{2} tr(E)^2 + \mu tr(E^2) \tag{A.1}$$

$\lambda > 0$ and $\mu > 0$ are called Lamé constants. Other elastic constants could be used instead, for example, Young's modulus$E > 0$ and Poisson's ratio$0 < \nu < 0.5$.Constants can be converted by:

$$E = \frac{\mu(3\lambda + 2\mu)}{\lambda + \mu} \; and \; \nu = \frac{\lambda}{2(\lambda + \mu)} \tag{A.2}$$

The applied values of the elastic constants differ, most values were chosen heuristically due to the lack of experimental data.

with C_{ij} andD_k, constants specific to the materials.

Mooney Rivlin model Here : N=1 with i=[0,1] et j =[0;1]

We obtain

$$W = C_{10}(I_1 - 3) + C_{01}(I_2 - 3) + \frac{1}{D_1}(J - 1)^2$$

Now the constants C_{10}, C_{01} and $D_1$are expressed as a function of the modulus of shear G and the bulk modulus$K$

$$G = C_{10} + C_{01} \; and \; K = \frac{E}{3(1 - 2\nu)}$$

In the literature, for simplicity we find $C_{10} = C_{01}$ in the case of the lungs ([Tehrani 2015]).

Neo-Hooke model Here : N=1 with i=1

We obtain

$$W = C_{10}(I_1 - 3) + \frac{1}{D_1}(J - 1)^2$$

Now the constantsC_{10}, andD_1 are expressed as a function of the modulus of shear$G = 2(C_{10})$ and the bulk modulus $K = D_1$

Yeoh model For the Yeoh model, the strain energy is dependent only on the first invariant I_1.

$$W = \sum_{i=1}^{3} C_i (I_1 - 3)^i$$

Becomes

$$W = C_1(I_1 - 3) + C_2(I_1 - 3)^2 + C_3(I_1 - 3)^3$$

The constants $G = 2C_1$, $G = -20C_2$, $G = 200C_3$ in the case of incompressible materials

Model based on experimental data [Zeng 1987] The experimental study, by [Zeng 1987] of lung tissue properties based on ex vivo samples (tested within 48 hours after death). The measurements give a nonlinear stress-strain relationship, which could be approximated by deformation per unit volume:

$$\begin{aligned} W = \tfrac{1}{2}c(&exp(a_1E_{11}^2 + a_2E_{22}^2 + 2a_4E_{11}E_{22}) \\ &+exp(a_1E_{11}^2 + a_2E_{33}^2 + 2a_4E_{11}E_{33}) \\ &+exp(a_1E_{33}^2 + a_2E_{22}^2 + 2a_4E_{33}E_{22})) \end{aligned} \tag{A.3}$$

The average values of c, a_1, a_2, et a_3 are 11.8 g/cm, 0.43, 0.56, and 0.32. E_{ij} denote the components of the Green-St deformation tensor. From. These data were used in the studies of Eom et al., In which the constraint of Equation (1) was applied[Eom 2009, Eom 2010], and the team of Al-Mayah , who approached the data using the deformation energy function of Marlow [Al-Mayah 2008, Al-Mayah 2011].

Even though these models are based on an experimental study these are based on averages and are therefore not specific to each patient. In addition, the reduction of the average errors remains in the same order as the models using St Venant-Kirchoff.

Concerning the boundary conditions, there are two possibilities: the surface displacement and the slip without friction. Even if the surface displacement gives correct results, the frictionless sliding allows to model the behavior of the sliding of the pleura and is thus closer to the physiology.

Appendix B

Principle of Mechanical Resolution by the Finite Element Method

B.1 Variational approach

The principle of the variational approach for the resolution of partial differential equations is to replace the equation by an equivalent formulation, called variational, obtained by integrating the equation multiplied by a test function. In our case, virtual displacements $\delta\overrightarrow{u}$ will be integrated in parts. In solids mechanics, the variational formulation obtained is identical to that given by the Principle of Virtual Works or in some cases the minimization of the total potential energy of the structure. The goal is therefore to minimize the energy given by the work applied to the structure for a displacement $\delta\overrightarrow{u}$.

The method for obtaining a variational formulation is as follows: the partial differential equations of the departure are transformed into an integral formulation of the form $\int_\Omega ...d\overrightarrow{u}$, then, an integration by parts makes it possible to get terms that only affect part of the domain boundary. Virtual displacements will weight the global integral.

This formulation leads to a system of algebraic equations that provides an approximate solution of the problem ($\int_\Omega ...\delta\overrightarrow{u}d\overrightarrow{u}$). There are several methods for constructing a variational formulation of a problem.

In our case, we have:

$$\rho\frac{\partial^2\vec{u}}{\partial^2 t} = \vec{div}\vec{\sigma} + \overrightarrow{f} \tag{B.1}$$

which is equivalent to, in Ωwhatever the vector \ overrightarrow $\overrightarrow{P}$:

$$\int_\Omega \overrightarrow{P}.(\rho\frac{\partial^2\vec{u}}{\partial^2 t} - \vec{div}\vec{\sigma} - \overrightarrow{f}).dV = 0 \tag{B.2}$$

In our case, our goal is to find the virtual work principle, so we pose $\overrightarrow{P} = \delta\vec{u}$:

$$\int_{\Omega} \delta\vec{u}.(\rho\frac{\partial^2\vec{u}}{\partial^2 t} - \vec{div}\vec{\sigma} - \overrightarrow{f}).dV = 0 \tag{B.3}$$

In addition we use the symmetry of the stress tensor and the following relations:

$$\sigma : grad\vec{u} = \overrightarrow{div}\sigma.\vec{u} - \vec{u}\cdot div\sigma T \qquad \sigma : grad^T\vec{u} = \overrightarrow{div}(\sigma\vec{u})\vec{u}\mathring{u}\overrightarrow{div}\sigma \tag{B.4}$$

The equation becomes:

$$\int_{\Omega} (\delta\vec{u}.\rho\frac{\partial^2\vec{u}}{\partial^2 t} + \sigma : grad\delta\overrightarrow{u} - \overrightarrow{div}(\sigma\ \vec{\delta u}) - \delta\vec{u}.\overrightarrow{f}).dV = 0 \tag{B.5}$$

Let's apply Ostrogradsky's theorem:

$$\int_{\Omega} (\delta\vec{u}.\rho\frac{\partial^2\vec{u}}{\partial^2 t} + \sigma : grad\delta\vec{\overrightarrow{u}} - -\delta\vec{u}.\overrightarrow{f}).dV - \int_{\partial\Omega} \delta\vec{u}.\sigma.\overrightarrow{n}.dS = 0 \tag{B.6}$$

$$A(\overrightarrow{u},\delta\overrightarrow{u}) = \int_{\Omega} (\delta\vec{u}.\rho\frac{\partial^2\vec{u}}{\partial^2 t} + \sigma : grad\delta\vec{\overrightarrow{u}} - -\delta\vec{u}.\overrightarrow{f}).dV \quad and \quad B(\delta\overrightarrow{u}) = \int_{\partial\Omega} \delta\vec{u}.\sigma.\overrightarrow{n}.dS$$

Subsequently we will note Y the variational formulation of a problem. Finally, the variational formulation of a problem with partial derivatives will lead to an equation of the type:

$$\Psi = A(\overrightarrow{u},\delta\overrightarrow{u}) - B(\delta\overrightarrow{u}) = 0\forall\delta U\in V \tag{B.7}$$

The terms $A(\overrightarrow{u},\delta\overrightarrow{u})$ and $B(\delta\overrightarrow{u})$ are composed of integrals. The interest of this formulation is to transform the integrals on the whole volume in sum of integrals on elements thanks to the additivity property of the integral. The problem will therefore be solved in the finite element Ω space.

B.2 Discretization in elements.

To find an approximate solution, we discretize the field of displacement. The structure is then cut into M "pieces" called elements defined by their geometries (hexahedron, tetrahedron ...). We will calculate the displacement field on a set of N discrete points in the solid (called "nodes" in finite element terminology) that constitute a mesh.

Subsequently the notation of the nodes is indicated by exponent while that of the elements in subscript.

We will note X^j the coordinates of the nodes where the exponent j goes from 1 to N. The unknown displacement vector with each node will be noted (U_x^j , U_y^j ,U_z^j).. The$\overrightarrow{u}(X)$ displacement field at a point belonging to the elementE_i will be specified by the approximation $\tilde{U}(X)$ resulting from the interpolation between the nodal valuesU^j thanks to the interpolation functions $w^j(X)$:

$$X \in \Omega_i, \tilde{U}(X) = \overset{[}{j} = 1]N^i\sum w^j(X)U^j.$$

with j the number of the vertex among the N^i vertices of the elementE_i. In this equation, the functions $w_j(X)$ satisfy $\overset{[}{j} = 1]N^i\sum w^j(X) = 1$ and coincide with the barycentric

coordinates of the point X. The functions of form $w^j(X)$ depend only on the position, and must have the following properties:

$$w^j(X^\beta) = \begin{cases} 1 \; si \; j = \beta \\ 0 \; si \; j \neq \beta \end{cases}$$

and :

$$w^j(X) = \begin{cases} 1 \; si \; X \in \beta \\ 0 \; si \; X \notin \beta \end{cases}$$

We can obviously interpolate virtual displacement fields in exactly the same way :

$$\delta\tilde{U}(X) = \overset{[}{j} = 1]N^i \sum w^j(X)\delta U^j.$$

and write the variational formulation again, substituting the interpolated fields in equation (7). For this, we express the functions $A(\overrightarrow{u}, \delta\overrightarrow{u})$ and$B(\delta\overrightarrow{u})$ as sums on elements.

In order to be able to correspond to each element i, the different nodes (among all the nodes N of the solid) which form part of this element, one must deny a matrix of localization named G_i. The matrixG_i makes it possible to obtain the displacementsU_i to the nodes of the elementE_i thanks to the nodes of the solid whole {U}:

$$U_i = G_i \overrightarrow{u}$$

The terms $G_{i_{kl}}$ are such that they are equal to 1 if the node numbered k on the complete solid coincides with the$l^{ème}$ node of the element E_i The dimension of the matrix G_i is thus $N_i \times N$.

B.3 Numerical integration and Matrix system

Let $\tilde{U}_i(X)$ be the displacement vector sought at a point of the element E_i and U_i the vector representing the displacement vectors of the N_i nodes of this element mesh. We have seen the passage of $\tilde{U}_i(X)$ toU_i this one can also be represented in the following matrix form:

$$\tilde{U}_i(X) = [W_i(X)]U_i$$

$[W_i(X)]$ is the interpolation matrix of the element E_i : $[W_i(X)] = [W_i^0(X), ..., W_i^{N_i}(X)]$. In the general anisotropic case, the elasticity matrix is written:

$$[D] = \begin{pmatrix} D_{xxxx} & D_{xxyy} & D_{xxzz} & D_{xxxy} & D_{xxxz} & D_{xxyz} \\ & D_{yyyy} & D_{yyzz} & D_{yyxy} & D_{yyxz} & D_{yyyz} \\ & & D_{zzzz} & D_{zzxy} & D_{zzxz} & D_{zzyz} \\ & & & D_{xyxy} & D_{xyxz} & D_{xyyz} \\ & Sym & & & D_{xzxz} & D_{xzxz} \\ & & & & & D_{yzyz} \end{pmatrix}$$

We then have the following relationship:

$$\sigma = [D]\varepsilon$$

On the other hand, in the case of small deformations, displacements and deformations are connected by the matrix [L] such that :

$$\varepsilon = [L]U$$

and in matrix expression :

$$\varepsilon = \begin{Bmatrix} \varepsilon_{xx} \\ \varepsilon_{yy} \\ \varepsilon_{zz} \\ 2\varepsilon_{xy} \\ 2\varepsilon_{xz} \\ 2\varepsilon_{yz} \end{Bmatrix} = [L]U(X) = \begin{vmatrix} \frac{\partial}{\partial x} & 0 & 0 \\ 0 & \frac{\partial}{\partial y} & 0 \\ 0 & 0 & \frac{\partial}{\partial z} \\ \frac{\partial}{\partial y} & \frac{\partial}{\partial x} & 0 \\ \frac{\partial}{\partial z} & 0 & \frac{\partial}{\partial x} \\ 0 & \frac{\partial}{\partial z} & \frac{\partial}{\partial y} \end{vmatrix} U(X)$$

And :

$$\varepsilon = [L][W_i]U_i = [C_i]U_i \; where \; [C_i] = [L][W_i]$$

The goal now is to group the terms of the variational formulation Ψ_i of an element as a matrix expression until an expression of the type :

$$\Psi_i = \delta U_i([K_i]U_i - F_i)$$

Where$[K_i]$ is the elementary stiffness matrix of the element andF_i is the second elementary element vector.

Still in the linear case, $A(U, \delta U)$can be written :

$$A(U, \delta U) = \overset{[}{i}]M \sum \int_{\Omega_i} \sigma(U)\varepsilon(\delta U)dv$$

By convention, <> represents the vectors in line and the vectors in column.

So $\sigma = \varepsilon^\top \sigma =< \varepsilon > \sigma$ } and :

$$A(U, \delta U) = \overset{[}{i}]M \sum \int_{\Omega_i} \varepsilon(\delta U)^\top \sigma(U)dv$$

Then if we use the matrix D, the expression becomes :

$$A(U, \delta U) = \overset{[}{i}]M \sum \int_{\Omega_i} \varepsilon(\delta U)^\top [D] \, \varepsilon(U)dv$$

v

$$A(U, \delta U) = \overset{[}{i}]M \sum \int_{\Omega_i} \delta U_i{}^\top [C_i]^\top [D] \, [C_i] \, U_i dv$$

$\delta U_i{}^\top$andU_i being nodal values, they can be output from the integral :

$$A(U, \delta U) = \overset{[}{i}]M \sum \delta U_i{}^\top \int_{\Omega_i} [C_i]^\top [D] \, [C_i] \, dv.U_i$$

Finally being nodal values, they can be output from the integral :

$$A(U, \delta U) = \overset{[}{i}]M \sum \delta U_i{}^{\top} \left[K_i\right]^{\top} \left[C_i\right] U_i$$

With $\left[K_i\right]^{\top} = \int_{\Omega_i} \left[C_i\right]^{\top} \left[D\right] \left[C_i\right] dv$
On the other hand, the member $B(\delta \overrightarrow{u})$ is written :

$$B(\delta U) = \overset{[}{i}]M \sum \left(\int_{\Omega_i} f_i \delta U_i dv + \int_{T^N} t_i \delta U_i ds \right)$$

with :

$$f_i = G_i f$$
$$t_i = G_i t$$

According to the displacements and the interpolation matrix and by leaving the nodal values of the integral :

$$B(\delta U) = \overset{[}{i}]M \sum \left(\delta U_i{}^{\top} \int_{\Omega_i} \left[W_i\right] f_i dv + \delta U_i{}^{\top} \int_{T^N} \left[W_i\right] t_i ds \right)$$

So, finally :

$$B(\delta U) = \overset{[}{i}]M \sum \delta U_i{}^{\top} \left[F_i\right]$$

With $\left[F_i\right] = \int_{\Omega_i} \left[W_i\right] f_i dv + \int_{T^N} \left[W_i\right] t_i ds$
Fundamentals of Continuum Mechanics and Finite Element Principles The global variational form Ψ is constructed by the addition of elementary forms :

$$\Psi = \overset{[}{i}]M \sum \Psi_i = MXi\delta Ui([Ki]Ui - Fi)$$

This sum is also organized in matrix form :

$$\Psi = ([K]U - F)\delta U$$

Where [K] is the global stiffness matrix and {F} is the second global member vector.

Appendix C

Geometrical tools for breathing modelisation

C.1 Principle of Non-Uniformal Rational B-Splines

The NURBS (Non-Uniformal Rational B-Splines) are mathematical representations of 3D geometry that can accurately describe any shape, from a simple 2D line, a circle, an arc, or a curve to a 3D organic surface or solid very complex free form. Thanks to their flexibility and precision, NURBS models can be used in any process, such as illustration, animation or manufacturing. The main interest of these NURBS is that they even manage to fit curves and surfaces that can not be represented by uniform B-splines. The latter can only represent exactly segments of the line and certain curves and surfaces.

Nurbs curves and surfaces act in a similar way and much of their terminology is the same. Since the curves are easier to describe, we will treat them first.

A NURBS curve of k degree is defined by :

— Control points $P_i$are a list of at least $n+1$ points.

— A knots vector $T = (t_0, t_1, ...)$,is a parameter value sequence that determines where and how control points will affect the shape. The number of nodes is always equal to $m+1$

— A normalized B-spline basis functions of degree k ,$N_{i,k}$,by means of n weight w_i (generally selected strict positives)

— The relation between the number of knots $(m+1)$, the degree (k) of $N_{i,k}$ and the number of control points $(n+1)$ is given by $m = n+k+1$

So a NURBS curve $C(t)$, which is a vector-valued piecewise rational polynomial function, is defined as [Piegl et al,91]:

$$C(t) = \frac{\sum_{i=0}^{m} w_i P_i N_{i,k}(t)}{\sum_{i=0}^{m} w_i N_{i,k}(t)}$$

These B-splines are defined recursively as:

$$\begin{cases} N_{i,1}(t) = \begin{cases} 1 & if\ t_i \leq t \leq t_{i+1} \\ 0 & else \end{cases} \\ N_{i,k}(t) = \frac{t-t_i}{t_{i+k}-t_i} N_{i,k-1}(t) + \frac{t_{i+k+1}-t}{t_{i+k+1}-t_{i+1}} N_{i+1,k-1}(t) \end{cases}$$

Nurbs Surfaces are obtained by extension of the definition of the NURBS curves with two knots vectors T and S, each having the variables$t$ and s. This variables have respectivly $m_t + 1$ and $m_s + 1$ nodes.

— Control points $P_{i,j}$are a list of at least $(m_t + 1) \times (m_s + 1)$ points.

— normalized B-spline basis functions of degree k ,$N_{i,k}$ and$N_{j,k}$,by means of $(m_t + 1) \times (m_s + 1)$ weight w_i (generally selected strict positives)

A NURBS-surface S is define in a similar way:

$$S(t) = \frac{\sum_{i=0}^{m_t} \sum_{j=0}^{m_s} w_{i,j} P_{i,j} N_{i,k}(t) N_{j,k}(t)}{\sum_{i=0}^{m_t} \sum_{j=0}^{m_s} w_{i,j} N_{i,k}(t) N_{j,k}(t)}$$

C.2 Principle of a-shape

The formal definition of a-shape was presented by H. Edelsbrunner and E. P. Mürke in their article [Edelsbrunner et al. 94]. The a-shape of a set of points is a generalization of the convex hull and a subgraph of the Delaunay triangulation.

The convex hull of a set P of points is the enclosing convex polygon contains P with smallest area [O'Rourke 98, DeBer et al. 00]. Equivalently, the convex hull of P is the intersection of all convex polygons that contain P. The intuitive idea of a-shape algorithm is digging the convex hull of a sample of points using a ball involves the Delaunay triangulation of these points.

For a real number a such that $0 \leq \alpha \leq +\infty$, the a-shape of a set point S is a polytope which is neither necessarily convex nor necessarily connected, defined as a subgraph of the Delaunay triangulation of S.

For$\alpha = +\infty$, the a-shape is identical to the convex envelope. However, as decreases from $+\infty$, the a-shape gradually contracts by developing cavities.

Formally, for *simplex*, an a-ball of radius a (a 0-ball is a point and a ∞-ball is an open half-space). An a-ball b is empty if :

$$b \cap S = \emptyset.$$

Any subset $T \subseteq S$ of size $|T| = k + 1$, with$0 \leq k \leq 3$, defines a k-simplex σ_t, convex envelope of T, denoted $conv(T)$.

For $0 \leq k \leq 2$, a k-simplex σ_t,is called a-exposed if there exists an empty a-ball b with $T = \partial b \cap S$, where ∂b is the bounding sphere or plane b.

Thus, a fixed defines a set $F_{k,\alpha}$ of k-simplexes a-exposed for $0 \leq k \leq 2$. The a-shape of S denoted S_α is the polytope whose limits are the triangles of $F_{2,\alpha}$, the edges of $F_{1,\alpha}$ and the vertices of $F_{0,\alpha}$.

In practice, if D is the Delaunay triangulation of the set of points S. For each k-simplex $\sigma_t \in D$, there exists a unique interval such that σ_t is a face of the form S_α if and only if a belongs to this interval. The calculation of the bounds of this interval according to the nature ofσ_t and $|T|$ is described in [Edelsbrunner et al. 94].

Moreover, the a-shape of a finite set of points S constitute a discrete family. Indeed, $S_{\alpha_1} \neq S_{\alpha_2}$ if and only if there exists an empty open ball bounded by the smallest sphere circumscribed on one side, a triangle, or a tetrahedron of D and whose radius is in the interval α_1 and α_2. As a result, the total number of a-shape of S is bounded by the total number N of k-simplexes of D (for $0 \leq k \leq 3$) plus one. So, S has at most $N = 2n^2 - 5n$ a-shapes where $n = card(S)$

List of Figures

1.1 Comparison of dose distribution in the case of a large tumour located in the base of the skull.(Left) HT using Carbon ions (two fields). (Right) IMRT (nine fields). In the case of HT it can be noticed a substantial reduction in the deposited dose in the normal tissue as compared to IMRT. Taken from [Durante 2010]. 6

1.2 Right : the schematic comparison between the dose profiles of photons and of charged particles used in HT. Left: a high dose of radiation is distributed to the tumour volume while not exceeding the tolerable dose of nearby critical healthy tissues. In contrast, with photons a lower dose is delivered to the tumour and a significant dose to the normal tissues distal from the tumour (figure taken from [Smith 2009]). 7

1.3 Lung deformations during the full breathing cycle and intermediate states (10 states). Image slices of a patient case are taken from the DIR-lab data base [Castillo 2009]. The curve is only for illustration purposes 8

1.4 Schematic representation of the volumes of interest defined by the ICRU [Jones 1994]. An example of the different treatment margins on lung cancer. 9

1.5 An example of the respiratory gating radiation therapy during the specific period of respiration. Taken from [Jung Ae Lee 2014] 9

1.6 An example of the robotic Cyberknife Synchrony system (Accuray Inc., Sunnyvale, Ca., USA) applied to x-ray radiosurgery. 10

1.7 Description of the different steps and workflow of radiation therapy with summary of each phases. 11

1.8 Global methodology to monitor the lung motion by the diaphragm muscles and rib kinematics, correlated to external sensors during treatment: between the spirometer and/or the capture of thoracic motion 13

2.1 Respiratory mechanics: the role of the diaphragm and thorax in breathing. 16

2.2 Anatomy of the Lungs divided into two halves, the right and left lungs. Each half of the lung is composed of lobes. Surrounding the lung is an airtight membrane called the pleural cavity. The pleural cavity is surrounded by the the chest wall on the sides, and the diaphragm on the bottom. 17

2.3 Anatomy of human diaphragm. It is composed of a peripheral part (muscular fibre) and a central part (tendon). 17

2.4 Anterior view of the thoracic cage and intercostal muscles (figure taken from http://anatomysciences.com). 18
2.5 Anatomy the mediastinum area found in the midline of the thorax that is surrounded by the left and right pleural sacs. It is divided into two parts: the superior and inferior mediastinum. 19
2.6 Inhalation and Exhalation: During the process of inhalation, the lung volume expands as a result of the contraction of the diaphragm and intercostal muscles. The exhalation the diaphragm and the intercostal muscles relax and involve a smaller thoracic volume and a positive pressure relative to the atmospheric pressure inside the thorax. 20
2.7 Pulmonary pressure volume curves obtained during inflation and deflation with air: Theoretical curve representing the pressure volume during the full cycle breathing. 21
2.8 Theoretical curve representing a dynamic compliance calculated by $C_{dyn} = \frac{Vt}{P_{peek}-PEEP}$ where Vt is the inspired or expired volume, P_{peek} the maximum pressure during the cycle and $PEEP$ residual pressure maintained in the airway during exhalation 21
2.9 Model components including body, lungs, and tumor. In the model without the contact surface; these displacements are applied to the lung's nodes directly since they are attached to those of the chest cavities. However, in the contact model; the boundary conditions are applied to the chest cavity nodes, not to the lungs, allowing sliding of lungs inside chest cavities. (figure taken from [Al-Mayah 2009]). 24
2.10 Illustration of two boundary condition (BC) concepts commonly applied for biomechanical modeling of lung ventilation. The first approach is to precompute lung surface displacements prior to the actual biomechanical modeling process. In the second approach, the forces are applied to the lung boundary are along the surface normal and also the motion of the lung surface points are allowed to slide along a limiting geometry (final breathing phase). (figure taken from [Ehrhardt 2013]). 25
2.11 Illustration of the anatomical boundary conditions (figure taken from [Werner 2009]). 25
2.12 Finite element model including a thoracic cavity, lung tumor and lungs (figure taken from [Eom 2010]). 26
2.13 Rib kinematics based on the Finite Helical Axis Method (FHAM). Left figure: two thorax sagittal views grey mesh: thorax segmented on the CT scans at an intermediate state of breathing black dots: computed rib cage position by inverse kinematics. Right figure: Finite helical axis method principle (figure taken from [Ladjal 2015]). 26
2.14 Right: Different parts of the human diaphragm and thorax including: tendon and muscles tissues, ribs, Thoracic vertebra, costal cartilage margin, body of sternum. Left: Finite element simulation of the human respiratory system: stress distribution and the total deformation of the diaphragm including the thorax behavior (figure taken from [Ladjal 2015]). 27

2.15 Finite element model of the thorax: Respiratory muscles, rib cage and vertebrae and diaphragm (figure taken from [Zhang 2016]). 28
2.16 Left: CT image showing the respiratory system of a patient. Right: patient specific biomechanical model of the lung motion used 4 and 16 pressure zones on the sub-diaphragm and thoracic cavity (figure taken from [Fuerst 2015]). 29

3.1 Schematic of a global pipeline to generate patient-specific anatomical 3D models of the respiratory system from medical images (CT scan data) to finite element simulation including: the organs segmentation, 3D CAD reconstruction and 3D mesh generation, boundary conditions and appropriate behavior for different parts of the respiratory system. 35
3.2 3D segmentation of the internal organs of the respiratory system: all ribs and diaphragm and 3D geometrical models issued directly from segmentation: human Ribcage and diaphragm. 36
3.3 Type of surface combinations for the marching cube algorithm. 38
3.4 Respiratory solid model superimposed onto CT scan volume images. 38
3.5 An example for 2D triangle meshes intersection and approximated by NURBS curves. 39
3.6 Geometrical patient specific of the respiratory system with NURBS (Non-Uniform Rational Basis Splines) including: diaphragm, thorax, mediastinum and lungs 40
3.7 Different parts and 3D tetrahedral meshes of the human respiratory system using two types of tetrahedral elements: The first-order tetrahedra (C3D4) and the modified 10 node elements (C3D10). 41
3.8 Contour diaphragm. 43
3.9 Strain estimation: the uniaxial strain deformation ε_1, the logarithmic strain ε_2 and the Green-Lagrange strain ε_3 43
3.10 Contour lungs. 44
3.11 Contour lungs. 45
3.12 Different parts and 3D tetrahedral meshes of the thorax including:ribs, thoracic vertebra, costal cartilage margin, body of sternum. 47
3.13 Finite Helical Axis Method (FHAM) represent 3D motion of the ribs described by a rotation (θ) about an axis and a translation (T) along an axis : (Left) shows the principle of the Finite Helical Axis Method (FHAM) and (Right) shows the automatic rib positions computed by interpolation at any intermediate state (figure taken from [Ladjal 2015]). 48
3.14 The boundary conditions (BC) of our patient specific biomechanical model including rib kinematics (a), and the personalized Compliance (b). 48
3.15 Global computational framework patient-specific model of the respiratory system. The personalized diaphragm forces and the lungs pressure during the whole respiratory cycle and for each intermediate respiratory state are calculated automatically based on inverse finite element optimization. . . . 49

3.16 Tetrahedral density map generation.The mass of a tetrahedral element equals the sum of the masses of volumes of intersection between the tetrahedron and the grid of voxels. 52

4.1 Two selected patients (6 and 10) from DIR-Lab Dataset [Castillo 2009], where the tumor location is visible 54
4.2 Euclidean distance between the landmark's simulated position (FEM) and the position at the target phase (medical images) 55
4.3 Evaluate lung tumor motion: affine registration applied to the segmented lung tumor volume at different respiratory states 55
4.4 Stabilization and internal energies: comparison between the energy dissipation due to stabilization (ALLSD) against the internal energy of the structure (ALLIE) 56
4.5 Mesh convergence study: Stress Von Mises computed for different resolution of meshing. 56
4.6 Some criteria of mesh quality of tetrahedral elements of the human diaphragm without thorax. The triangular mesh element showing the longest side, shortest side, maximum interior angle and the minimum interior angle. 57
4.7 Different specific compliances for each patient, calculated and identified at each state directly from 4D CT scan images 58
4.8 Qualitative analysis of finite element simulation for respiratory system . . . 58
4.9 Distance error measurement on the diaphragm and lungs between FEM simulated end inspiration EI and segmented EI extracted from CT images. . . 59
4.10 The percentile errors distribution for patient from DIRlab dataset in the AP, RL, and SI directions at EE and EI phases. 61
4.11 The percentile errors distribution for patient from DIRlab dataset in the AP, RL, and SI directions at EE and EI phases. 62
4.12 Mean errors ± standard deviation of lung tumor position during the whole cycle of breathing (10 phases between the EI and EE) between the trajectory issued from 4D CT images compared to the trajectory calculated by biomechanical finite element simulation coupled with the lung-pressure/diaphragm-force optimization for two patients P6 and P10. 64
4.13 3D lung tumor trajectory (in mm) issued from 4D CT images compared to the trajectory calculated by biomechanical finite element model including or not the rib kinematics for patients P6 for DirLab data set [Castillo 2009]. . 66
4.14 3D lung tumor trajectory (in mm) issued from 4D CT images compared to the trajectory calculated by biomechanical finite element model including or not the rib kinematics for patients P10 for DirLab data set [Castillo 2009]. . 67
4.15 3D lung tumor trajectory (in mm) issued from 4D CT images compared to the trajectory calculated by biomechanical finite element model including rib kinematics displacement changed by 10%, 25% and 50% of the rib displacement calculated from CT scan images. 68
4.16 Young's modulus sensibility: Average landmark lung error (mm) during respiration at different respiratory states for different value of Young's modulus 69

4.17 Poisson's ratio sensibility: Average landmark lung error (mm) during respiration at different respiratory states for different value of Poisson's ratio . . 70
4.18 Mean errors ± SD between FE simulation results with ground truth (4D CT images) on 75 anatomical landmarks, at end inspiration (EI) and end expiration (EE) states based on four hyperelastic models: Neo-Hookean model, Yeoh model, Mooney-Rivlin model and St. Venant-Kirchoff model. 72

5.1 Dynamic anthropomorphic breathing phantom, LuCa (Lung Cancer) developed by the Center for Proton Therapy at the Paul Scherrer Institute (PSI) 77

List of Tables

2.1 List of most studies of biomechanical models for respiratory system that have been used in the literature. 30

3.1 Five selected patients from DIR-Lab Dataset [Castillo 2009], with small and large breathing amplitudes. 37

3.2 Experimental data analysis: Quantification of the deformation of the human diaphragm based on 4CT scan data for twelve patients, $\varepsilon_1 = \frac{l-l_0}{l_0}$, $\varepsilon_2 = ln\left(\frac{l}{l_0}\right)$, $\varepsilon_3 = \frac{1}{2}\left(\frac{l^2-l_0^2}{l_0^2}\right)$ 42

4.1 Mechanical properties of breathing system: LE Linear Elastic, HVSK Hyperelastic Saint Venant Kirchhoff, E Youngs modulus andν Poisson coefficient (from [Al-Mayah 2011, Villard 2005], ρ volumetric density (calculated from CT images) 59

4.2 Average surface errors (mm) for the diaphragm and lungs surfaces at end inspiration EI between FEM simulation surface and segmented surfaces extracted from CT images for four patients from DirLab database [Castillo 2009] 60

4.3 Average anatomical landmark lung error(mm) at end inspiration (EI) and end expiration (EE) states for four patients from DirLab database [Castillo 2009] 63

4.4 Average landmark lung error (mm) during respiration at different respiratory states: the first state T00, the end inspiration (T50), the end expiration (T10) 63

4.5 Comparison between our biomechanical patient specific model results and the results from Fuerst et al. [Fuerst 2015] and Li et al. [Li 2015], on patient 6, patient 9 and patient 10 issued from DIR-Lab Dataset [Castillo 2009]. . . 65

4.6 Material parameters value for four hyperelastic models for respiratory motion 71

Bibliography

[Al-Mayah] Adil Al-Mayah, Joanne Moseley, Mike Velec et Kristy Brock. Effect of heterogeneous material of the lung on deformable image registration. page 72610V. (Cité en page 43.)

[Al-Mayah 2008] A Al-Mayah, J Moseley et KK Brock. Contact surface and material nonlinearity modeling of human lungs. Physics in medicine and biology, vol. 53, no. 1, page 305, 2008. (Cité en pages 43, 50 et 85.)

[Al-Mayah 2009] A. Al-Mayah, J. Moseley, M. Velec et K. K. Brock. Sliding characteristic and material compressibility of human lung: Parametric study and verification. Medical Physics, vol. 36, no. 10, pages 4625–4633, 2009. (Cité en pages 23, 24 et 98.)

[Al-Mayah 2011] Adil Al-Mayah, Joanne Moseley, Mike Velec et Kristy Brock. Toward efficient biomechanical-based deformable image registration of lungs for image-guided radiotherapy. Physics in medicine and biology, vol. 56, no. 15, page 4701, 2011. (Cité en pages 28, 59, 65, 85 et 103.)

[Baudet 2003] V. Baudet, P.-. Villard, F. Jaillet, M. Beuve et B. Shariat. Towards accurate tumour tracking in lungs. In Proc. Seventh Int. Conf. Information Visualization IV 2003, pages 338–343, Juillet 2003. (Cité en page 23.)

[Bert 2010] Christoph Bert, Alexander Gemmel, Nami Saito, Naved Chaudhri, Dieter Schardt, Marco Durante, Gerhard Kraft et Eike Rietzel. Research Dosimetric precision of an ion beam tracking system. 2010. (Cité en page 10.)

[Bert 2011] Christoph Bert et Marco Durante. Motion in radiotherapy: particle therapy. Physics in medicine and biology, vol. 56, no. 16, page R113, 2011. (Cité en page 10.)

[Castillo 2009] Richard Castillo, Edward Castillo, Rudy Guerra, Valen E Johnson, Travis McPhail, Amit K Garg et Thomas Guerrero. A framework for evaluation of deformable image registration spatial accuracy using large landmark point sets. Physics in Medicine and Biology, vol. 54, no. 7, page 1849, 2009. (Cité en pages 8, 35, 37, 54, 60, 63, 65, 66, 67, 75, 80, 97, 100 et 103.)

[Cluzel 2000] P Cluzel, T Similowski, C Chartrand-Lefebvre, M Zelter, J P Derenne et P A Grenier. Diaphragm and chest wall: assessment of the inspiratory pump with MR imaging-preliminary observations. Radiology, vol. 215, pages 574–583, Mai 2000. (Cité en page 36.)

[Didier 2007] A-L Didier, P-F Villard, J-Y Bayle, Michael Beuve et Behzad Shariat. Breathing thorax simulation based on pleura physiology and rib kinematics. In

Medical Information Visualisation-BioMedical Visualisation, 2007. MediVis 2007. International Conference on, pages 35–42. IEEE, 2007. (Cité en pages 23, 26 et 47.)

[Durante 2010] Marco Durante et Jay S Loeffler. Charged particles in radiation oncology. Nature reviews Clinical oncology, vol. 7, no. 1, pages 37–43, 2010. (Cité en pages 6 et 97.)

[Ehrhardt 2013] Jan Ehrhardt, Cristian Lorenzet al. 4d modeling and estimation of respiratory motion for radiation therapy. Springer, 2013. (Cité en pages 12, 22, 24, 25 et 98.)

[Eom 2009] Jaesung Eom, Chengyu Shi, Xie George Xu et Suvranu De. Modeling respiratory motion for cancer radiation therapy based on patient-specific 4DCT data. vol. 12, pages 348–355, 2009. (Cité en pages 23, 24 et 85.)

[Eom 2010] Jaesung Eom, Xie George Xu, Suvranu De et Chengyu Shi. Predictive modeling of lung motion over the entire respiratory cycle using measured pressure-volume data, 4DCT images, and finite-element analysis. Medical physics, vol. 37, no. 8, pages 4389–4400, 2010. (Cité en pages 24, 26, 85 et 98.)

[Fokdal 2004] Lars Fokdal, Henriette Honoré, Morten Høyer, Peter Meldgaard, Kirsten Fode et Hans von der Maase. Impact of changes in bladder and rectal filling volume on organ motion and dose distribution of the bladder in radiotherapy for urinary bladder cancer. International Journal of Radiation Oncology* Biology* Physics, vol. 59, no. 2, pages 436–444, 2004. (Cité en page 7.)

[Fuerst 2015] B. Fuerst, T. Mansi, F. Carnis, M. SÃďlzle, J. Zhang, J. Declerck, T. Boettger, J. Bayouth, N. Navab et A. Kamen. Patient-Specific Biomechanical Model for the Prediction of Lung Motion From 4-D CT Images. IEEE Transactions on Medical Imaging, vol. 34, no. 2, pages 599–607, Février 2015. (Cité en pages 27, 29, 43, 63, 65, 99 et 103.)

[Giroux 2017a] Matthieu Giroux, Hamid Ladjal, M Beuve, P Giraud et B Shariat. Patient-Specific Biomechanical Modeling of the Lung Tumor for Radiation Therapy. Computer methods in biomechanics and biomedical engineering, vol. 20, no. sup1, pages 95–96, 2017. (Cité en pages 29, 43, 50, 54 et 65.)

[Giroux 2017b] Matthieu Giroux, Hamid Ladjal, Michael Beuve et Behzad Shariat. Biomechanical Patient-Specific Model of the Respiratory System Based on 4D CT Scans and Controlled by Personalized Physiological Compliance. In Maxime Descoteaux, Lena Maier-Hein, Alfred Franz, Pierre Jannin, D. Louis Collins et Simon Duchesne, editeurs, Medical Image Computing and Computer-Assisted Intervention âĹŠ MICCAI 2017, volume 10434, pages 216–223. Springer International Publishing, 2017. DOI: 10.1007/978-3-319-66185-8_25. (Cité en pages 29 et 43.)

[Hof 2003] Holger Hof, Klaus K Herfarth, Marc Münter, Angelika Hoess, Johann Motsch, Michael Wannenmacheret al. Stereotactic single-dose radiotherapy of stage I non–small-cell lung cancer (NSCLC). International Journal of Radiation Oncology* Biology* Physics, vol. 56, no. 2, pages 335–341, 2003. (Cité en page 7.)

[Ilegbusi 2014] Olusegun J. Ilegbusi, Behnaz Seyfi et Rafael Salvin. Patient-specific model of lung deformation using spatially dependent constitutive parameters. Mathematical

and Computer Modelling of Dynamical Systems, vol. 20, no. 6, pages 546–556, 2014. (Cité en page 23.)

[Jones 1994] Douglas Jones. ICRU report 50âĂŤprescribing, recording and reporting photon beam therapy. Medical Physics, vol. 21, no. 6, pages 833–834, 1994. (Cité en pages 8, 9 et 97.)

[Jung Ae Lee 2014] Dae Sik Yang Won Sup Yoon Young Je Park Suk Lee Jung Ae Lee Chul Yong Kim et Young Bum Kim. Four-dimensional computed tomography based respiratory-gated radiotherapy with respiratory guidance system: analysis of respiratory signals and dosimetric comparison. BioMed research international, vol. 2014, 2014. (Cité en pages 9 et 97.)

[Kilby 2010] W Kilby, JR Dooley, G Kuduvalli, S Sayeh, CR Maurer Jret al. The CyberKnife Robotic Radiosurgery System in 2010. Technology in cancer research & treatment, vol. 9, no. 5, pages 433–452, 2010. (Cité en page 10.)

[Ladjal 2013a] H. Ladjal, J. L. Hanus et A. Ferreira. Micro-to-Nano Biomechanical Modeling for Assisted Biological Cell Injection. IEEE Transactions on Biomedical Engineering, vol. 60, no. 9, pages 2461–2471, Septembre 2013. (Cité en page 40.)

[Ladjal 2013b] Hamid Ladjal, Behzad Shariat, Joseph Azencot et Michael Beuve. Appropriate Biomechanics and kinematics Modeling of the respiratory System: Human Diaphragm and Thorax. In Intelligent Robots and Systems (IROS), 2013 IEEE/RSJ International Conference on, pages 2004–2009. IEEE, 2013. (Cité en pages 26, 37, 40 et 47.)

[Ladjal 2015] Hamid Ladjal, Joseph Azencot, Michael Beuve, Philippe Giraud, Jean Michel Moreau et Behzad Shariat. Biomechanical Modeling of the Respiratory System: Human Diaphragm and Thorax. Computational Biomechanics for Medicine, Janvier 2015. (Cité en pages 26, 27, 37, 40, 47, 48, 98 et 99.)

[Langen 2001] KM Langen et DTL Jones. Organ motion and its management. International Journal of Radiation Oncology* Biology* Physics, vol. 50, no. 1, pages 265–278, 2001. (Cité en page 7.)

[Li 2006] Kang Li, Xiaodong Wu, D. Z. Chen et M. Sonka. Optimal Surface Segmentation in Volumetric Images-A Graph-Theoretic Approach. IEEE Transactions on Pattern Analysis and Machine Intelligence, vol. 28, no. 1, pages 119–134, Janvier 2006. (Cité en page 36.)

[Li 2015] Feng Li et Fatih Porikli. Biomechanical model-based 4DCT simulation. Computer Methods in Biomechanics and Biomedical Engineering: Imaging & Visualization, vol. 3, no. 4, pages 222–233, 2015. (Cité en pages 63, 65 et 103.)

[Lu 2007] Hsiao-Ming Lu, Robert Brett, Gregory Sharp, Soiros Safai, Steve Jiang, Jay Flanz et Hanne Kooy. A respiratory-gated treatment system for proton therapy. Medical physics, vol. 34, no. 8, pages 3273–3278, 2007. (Cité en page 9.)

[Manescu 2013] Petru Manescu, Hamid Ladjal, Joseph Azencot, Michael Beuve, Etienne Testa et Behzad Shariat. Four-dimensional radiotherapeutic dose calculation using biomechanical respiratory motion description. International Journal of Computer Assisted Radiology and Surgery, pages 1–9, 2013. (Cité en pages 50, 51 et 52.)

[Minohara 2000] Shinichi Minohara, Tatsuaki Kanai, Masahiro Endo, Kouji Noda et Mitsutaka Kanazawa. Respiratory gated irradiation system for heavy-ion radiotherapy. International Journal of Radiation Oncology* Biology* Physics, vol. 47, no. 4, pages 1097–1103, 2000. (Cité en page 9.)

[Mori 2009] Shinichiro Mori, Hsiao-Ming Lu, John A Wolfgang, Noah C Choi et George TY Chen. Effects of interfractional anatomical changes on water-equivalent pathlength in charged-particle radiotherapy of lung cancer. Journal of radiation research, vol. 50, no. 6, pages 513–519, 2009. (Cité en page 7.)

[Nakao 2007] Megumi Nakao, Ayako, M. Kokubo et Kotaro. Simulating lung tumor motion for dynamic tumor-tracking irradiation. In Proc. IEEE Nuclear Science Symp. Conf. Record, volume 6, pages 4549–4551, Octobre 2007. (Cité en pages 23, 28 et 65.)

[Negoro 2001] Yoshiharu Negoro, Yasushi Nagata, Tetsuya Aoki, Takashi Mizowaki, Norio Araki, Kenji Takayama, Masaki Kokubo, Shinsuke Yano, Sachiko Koga, Keisuke Sasaiet al. The effectiveness of an immobilization device in conformal radiotherapy for lung tumor: reduction of respiratory tumor movement and evaluation of the daily setup accuracy. International Journal of Radiation Oncology* Biology* Physics, vol. 50, no. 4, pages 889–898, 2001. (Cité en page 7.)

[Nihei 2006] Keiji Nihei, Takashi Ogino, Satoshi Ishikura et Hideki Nishimura. High-dose proton beam therapy for Stage I non–small-cell lung cancer. International Journal of Radiation Oncology* Biology* Physics, vol. 65, no. 1, pages 107–111, 2006. (Cité en page 8.)

[Ota S 2015] Sumida I Yoshioka Y Kado R et al Ota S Monzen H. Quality Improvement in External Radiation Therapy Using a Departmental Incident-Reporting System and Multidisciplinary Team Efforts. J Nucl Med Radiat Ther., vol. 6, pages doi: 10.4172/2155–9619.1000243, 2015. (Cité en page 11.)

[Promayon 2008] E. Promayon et P. Baconnier. A 3D Discrete Model of the Diaphragm and Human Trunk. In L. Boudin, C. Grandmont, Y. Maday, B. Maury et J. F. Gerbeau, editeurs, Lung Modelling, volume 23, pages 66–77, July 2008. (Cité en page 23.)

[Seppenwoolde 2002] Yvette Seppenwoolde, Hiroki Shirato, Kei Kitamura, Shinichi Shimizu, Marcel van Herk, Joos V Lebesque et Kazuo Miyasaka. Precise and real-time measurement of 3D tumor motion in lung due to breathing and heartbeat, measured during radiotherapy. International Journal of Radiation Oncology* Biology* Physics, vol. 53, no. 4, pages 822–834, 2002. (Cité en page 7.)

[Shirato 2004] Hiroki Shirato, Masataka Oita, Katsuhisa Fujita, Yoshiharu Watanabe et Kazuo Miyasaka. Feasibility of synchronization of real-time tumor-tracking radiotherapy and intensity-modulated radiotherapy from viewpoint of excessive dose from fluoroscopy. International Journal of Radiation Oncology* Biology* Physics, vol. 60, no. 1, pages 335–341, 2004. (Cité en page 7.)

[Shirato 2006] Hiroki Shirato, Keishiro Suzuki, Gregory C Sharp, Katsuhisa Fujita, Rikiya Onimaru, Masaharu Fujino, Norio Kato, Yasuhiro Osaka, Rumiko Kinoshita, Hiroshi Taguchiet al. Speed and amplitude of lung tumor motion precisely detected in four-dimensional setup and in real-time tumor-tracking radiotherapy. International

Journal of Radiation Oncology* Biology* Physics, vol. 64, no. 4, pages 1229–1236, 2006. (Cité en pages 12 et 23.)

[Smith 2009] Alfred R Smith. Present Status and Future Developments in Proton Therapy. In Laser-driven relativistic plasmas applied to science, industry and medicine: the 2nd international symposium, Kyoto, Japan, 19-23 January 2009, numéro 1153, page 426. Amer Inst of Physics, 2009. (Cité en pages 7 et 97.)

[Tehrani 2015] Joubin Nasehi Tehrani, Yin Yang, Rene Werner, Wei Lu, Daniel Low, Xiaohu Guo et Jing Wang. Sensitivity of tumor motion simulation accuracy to lung biomechanical modeling approaches and parameters. vol. 60, no. 22, pages 8833–8849, 2015. (Cité en pages 24 et 84.)

[Vidal 2012] F. P. Vidal, P. Villard et ÃĽ. Lutton. Tuning of Patient-Specific Deformable Models Using an Adaptive Evolutionary Optimization Strategy. IEEE Transactions on Biomedical Engineering, vol. 59, no. 10, pages 2942–2949, Octobre 2012. (Cité en page 23.)

[Villard 2004] P.-F. Villard, M. Beuve, B. Shariat, V. Baudet et F. Jaillet. Lung mesh generation to stimulate breathing motion with a finite element method. pages 194–199. IEEE, 2004. (Cité en page 24.)

[Villard 2005] P-F Villard, Michaël Beuve, Behzad Shariat, Vincent Baudet et Fabrice Jaillet. Simulation of lung behaviour with finite elements: Influence of bio-mechanical parameters. In Medical Information Visualisation-Biomedical Visualisation, 2005.(MediVis 2005). Proceedings. Third International COnference on, pages 9–14. IEEE, 2005. (Cité en pages 23, 24, 26, 28, 43, 50, 59, 65 et 103.)

[Villard 2009] Pierre-FrÃĺdÃĺric Villard, Franck P. Vidal, Carrie Hunt, Fernando Bello, Nigel W. John, Sheena Johnson et Derek A. Gould. A prototype percutaneous transhepatic cholangiography training simulator with real-time breathing motion. International Journal of Computer Assisted Radiology and Surgery, vol. 4, no. 6, page 571, Novembre 2009. (Cité en page 23.)

[Werner 2008] Rene Werner, Jan Ehrhardt, Rainer Schmidt et Heinz Handels. Modeling respiratory lung motion: a biophysical approach using finite element methods. page 69160N, 2008. (Cité en pages 23 et 24.)

[Werner 2009] René Werner, Jan Ehrhardt, Rainer Schmidt et Heinz Handels. Patient-specific finite element modeling of respiratory lung motion using 4D CT image data. Medical physics, vol. 36, no. 5, pages 1500–1511, 2009. (Cité en pages 23, 24, 25, 28, 65 et 98.)

[Wilson 2001] T A Wilson, A Legrand, P A Gevenois et A De Troyer. Respiratory effects of the external and internal intercostal muscles in humans. The Journal of physiology, vol. 530, pages 319–330, Janvier 2001. (Cité en page 47.)

[Yalamanchili 2010] R. Yalamanchili, D. Chittajallu, P. Balanca, B. Tamarappoo, D. Berman, D. Dey et I. Kakadiaris. Automatic segmentation of the diaphragm in non-contrast CT images. In Proc. IEEE Int. Symp. Biomedical Imaging: From Nano to Macro, pages 900–903, Avril 2010. (Cité en page 36.)

[Zeng 1987] YJ Zeng, D Yager et YC Fung. Measurement of the mechanical properties of the human lung tissue. Journal of biomechanical engineering, vol. 109, no. 2, pages 169–174, 1987. (Cité en pages 23, 24 et 85.)

[Zhang 2016] Guangzhi Zhang, Xian Chen, Junji Ohgi, Toshiro Miura, Akira Nakamoto, Chikanori Matsumura, Seiryo Sugiura et Toshiaki Hisada. Biomechanical simulation of thorax deformation using finite element approach. Biomedical engineering online, vol. 15, no. 1, page 18, 2016. (Cité en pages 27, 28 et 99.)